8-11-2020

Phase Clusters and Chimeras in Networks of Kuramoto Oscillators with Inertia

Barrett N. Brister
Georgia State University

PHASE CLUSTERS AND CHIMERAS IN NETWORKS OF KURAMOTO OSCILLATORS WITH INERTIA

by

BARRETT NUGENT BRISTER

Under the Direction of Dr. Igor Belykh

ABSTRACT

Modeling cooperative dynamics using networks of phase oscillators is a common practice for a wide spectrum of biological networks. Patterns of synchronized clusters are some of the most prevalent instances of such cooperative behavior, manifesting themselves in ways similar to groups of neurons firing together during epileptic seizures or Parkinson's tremors. Despite significant interest, the emergence and hysteretic transitions between stable clusters in oscillator networks have still not been fully understood. In particular, the celebrated

Kuramoto model of phase oscillators is known to exhibit multiple spatio-temporal patterns, including co-existing clusters of synchrony and chimera states in which some oscillators form a synchronous cluster, while the others oscillate asynchronously. Rigorous analysis of the stability of clusters and chimeras in the finite-size Kuramoto model has proven to be challenging, and most existing results are numerical. In this thesis, we contribute toward the rigorous understanding of the emergence of stable clusters in networks of identical Kuramoto oscillators with inertia. We first study the co-existence of stable patterns of synchrony in two coupled populations of identical Kuramoto oscillators with inertia. The two populations have different sizes and can split into two clusters where the oscillators synchronize within a cluster while there is a phase shift between the dynamics of the two clusters. Due to the presence of inertia, which increases the dimensionality of the oscillator dynamics, this phase shift can oscillate, inducing a breathing cluster pattern. We derive analytical conditions for the co-existence of stable two-cluster patterns with constant and oscillating phase shifts. We then study the emergence of stable clusters of synchrony with complex inter-cluster dynamics in a three-population network of identical Kuramoto oscillators with inertia. We extend the results of the bistability of synchronized clusters in the two-population network and demonstrate that the addition of a third population can induce chaotic inter-cluster dynamics. This effect can be captured by the old adage "two is company, three is a crowd" which suggests that the delicate dynamics of a romantic relationship may be destabilized by the addition of a third party, leading to chaos. Through rigorous analysis and numerics, we demonstrate that the inter-cluster phase shifts can stably co-exist and exhibit different forms of chaotic behavior, including oscillatory, rotatory, and mixed-mode oscillations. We also discuss the implications of our results for predicting the emergence of chimeras and

solitary states in real-world biological networks.

INDEX WORDS: Networks, Coupled oscillators, Kuramoto model, Inertia, Clusters, Chimeras, Multistability

PHASE CLUSTERS AND CHIMERAS IN NETWORKS OF KURAMOTO OSCILLATORS WITH INERTIA

by

BARRETT NUGENT BRISTER

A Dissertation Submitted in Partial Fulfillment of the Requirements for the Degree of

Doctor of Philosophy

in the College of Arts and Sciences

Georgia State University

2020

PHASE CLUSTERS AND CHIMERAS IN NETWORKS OF KURAMOTO OSCILLATORS WITH INERTIA

by

BARRETT BRISTER

Committee Chair: Igor Belykh

Committee: Vladimir Bondarenko

Yaroslav Molkov

Michael Stewart

Electronic Version Approved:

Office of Graduate Studies

College of Arts and Sciences

Georgia State University

August 2020

DEDICATION

This dissertation is dedicated to my parents, Mark and Rhonda Brister, who have always been there for me no matter what.

ACKNOWLEDGEMENTS

I would be remiss if I did not take the opportunity to thank the many, many people who helped me along this wonderful journey. Though I understand that a number people helped me in ways that I will never know, I can at least acknowledge as many of you as I can.

Dr. Igor Belykh, thank you for guiding me through the many twists and turns of my work. No matter how stuck I seemed at times, you always gave me the push I needed to get going again. You remained consistent and persistent even during the moments when I was not.

To the rest of my dissertation committee – Drs. Vladimir Bondarenko, Michael Stewart, and Yaroslav Molkov – I greatly appreciate the time and effort you put into advising this dissertation. I also appreciate the instruction from you and the many other professors and instructors at Georgia State University. In particular, Dr. Valerie Miller, your wit, wisdom, teaching experience, and honest advice was more valuable than I can put into words.

Sandra Ahuama-Jonas, Beth Conner, and Earnestine Collier-Jones, thank you for guiding me through the complex maze of bureaucracy and showing me the right step to take every time.

Sutandra Sarkar, Dr. Mikhail Stroev, and Martin Crowe, thank you for all the help with the MILE and teaching MATH 1113.

Thank you to my colleagues in the Belykh Lab: Kevin Daley, Kelley Smith, Reimbay Reimbayev, Ratislav Krylov, and Russell Jeter. In particular, thank you to Kevin for your camaraderie and your assistance with Python and complex dynamical systems. Several components of this work were made easier because of your help.

To my other graduate school colleagues – Elizaveta Latash, William Barnett, Rodrigo Castro, Akossi Aurelie, Xiuxiu He, Aubrey Kemp, Deniz Alaçam, Howard Smith, Sara Motlaghian, Jie Nissel, Alex Carstairs, Siang Ng, Kevin James, and the many others whose names elude me – thank you for your inspiration and in many cases, friendship. Thank you to Sergey Klimov and Regina Chang for staying the course to the end on one of the most

stressful yet ultimately satisfying school projects I have ever worked on.

Thank you to all the students I had over the years. Just as I taught you how to do math even better, you taught me how to teach even better.

My family members and friends, you gave me love and support at just the right times. Some of you helped me keep going in those critical moments when I didn't know if I could continue with this daunting task. You know who you are!

Finally, I want to thank Georgia State University as a whole, which made this whole opportunity possible. You have given me a new direction in my life and career, for which I will always be grateful.

I am thankful for the SIAM Student Travel Award which allowed me to present the work related to this thesis at the 2019 SIAM Conference on Applications of Dynamical Systems at Snowbird, Utah. I gratefully acknowledge support from the Georgia State University Brains and Behavior Program as a Student Fellow and from the National Science Foundation under Grant No. DMS-1909924.

IMPACT

The results of this thesis were published in two journal papers and one refereed conference proceedings:

1. B. Brister, V. Belykh, and I. Belykh, "When three is a crowd: chaos from clusters of Kuramoto oscillators with inertia," *Physical Review E,* 101, 062206 (2020).

2. B. Brister, V. Belykh, and I. Belykh, "Multistable cluster rhythms in networks of coupled rotators," *Proceedings of the 9th International Conference "Physics and Control" (PhysCon-2019),* Innopolis, Russia, September 8-11, IPACS Press, pp. 1-6 (2019).

3. I. Belykh, B. Brister, and V. Belykh, "Bistability of patterns of synchrony in Kuramoto oscillators with inertia," *Chaos,* 26, 094822 (2016).

This work was presented at the following national and international meetings:

- B. Brister and I. Belykh, "Kuramoto oscillator models as a paradigm for neuronal synchronization," 2019 Brains & Behavior Retreat, Georgia State University, May 24, 2019.

- R. Krylov, K. Daley, B. Brister, C. Epstein, M. Dhamala, and I. Belykh, "Functional network reconstruction and analysis of epileptic seizures," 2019 Brains & Behavior Summer Research Symposium, Georgia State University, August 7, 2019.

- B. Brister, V. Belykh, and I. Belykh, "When three is a crowd: chaos from clusters in networks of phase oscillators with inertia," SIAM Conference on Applications of Dynamical Systems, Snowbird, Utah, May 21, 2019.

- B. Brister, V. Belykh, and I. Belykh, "When three is a crowd: chaos from clusters in networks of Kuramoto oscillators with inertia," International Workshop "Dynamics of Coupled Oscillator Systems," The Weierstrass Institute, Berlin, Germany, November 19, 2018.

- B. Brister, V. Belykh, and I. Belykh, "Multistability of synchronized clusters in networks of phase oscillators," International Conference "Frontiers of Mathematical Biology: Modeling, Computation, and Analysis," Orlando, May 2, 2018.

- B. Brister, V. Belykh, and I. Belykh, "Multistability of synchronized clusters in networks of phase oscillators," Department Retreat, GSU Department of Mathematics, April 5, 2018.

- B. Brister, V. Belykh, and I. Belykh, "Multistable clusters and chimeras in networks of phase oscillators," Georgia Scientific Computing Symposium, Georgia State University, February 24, 2018.

- B. Brister, V. Belykh, and I. Belykh, "Bistability of patterns of synchrony in Kuramoto oscillators with inertia," IEEE International Workshop on Complex Systems and Networks, Georgia State University, November 13, 2016.

TABLE OF CONTENTS

LIST OF FIGURES

CHAPTER 1

INTRODUCTION

Patterns of synchronized activities are observed in many natural and technological networks [98, 82, 29]. In biological systems, examples include synchronized cortical rhythms in the central systems of mammals which are crucial for sensory perception, memory, and locomotion [35, 67, 107], pathological neuronal synchronization which causes epileptic seizures and Parkinson's tremors [89, 50], birds flying in formation and maneuvering as one cohesive unit [33], and synchronized gaits of walkers on a wobbly footbridge [99, 41, 15, 13]. In technological systems, synchronization is required for an array of lasers to reach high power levels [87, 86, 39] and for power generators for the operation of electrical power grids [68].

The strongest form of synchronized activities is complete synchronization of identical or nearly identical oscillators whose emergence and stability are controlled by the underlying network structure [79, 28, 17, 10]. Cluster synchronization emerges when the network splits into clusters of coherent oscillators but the dynamics between the clusters remains asynchronous [16, 18, 83, 84, 8, 46, 45, 106, 80, 12, 57, 95]. The existence of clusters in networks of identical oscillators are governed by network symmetries, and possible cluster partitions can be identified by combinatorial methods [12, 57, 95]. The stability of cluster synchronization [16, 83, 84, 80, 95] and its persistence against individual oscillators' parameter mismatch [8] have been studied for several general classes of oscillator networks. However, the emergence and hysteretic transitions between clusters in multistable oscillator networks have yet to be fully understood.

The classical Kuramoto model of first-order phase oscillators with mean-field coupling [59, 97, 82] is such an example of a network capable of exhibiting various synchronization patterns [3, 7, 76, 65, 53, 81, 63, 85]. The oscillators are assumed to be non-identical with different natural frequencies, whose distribution is defined by a given probability density

function. The model has a coupling threshold such that the oscillators, evolving incoherently for a weak coupling, synchronize when the coupling exceeds the threshold. Transitions from the incoherent state to various forms of partial frequency synchronization, measured by an order parameter, have been studied in the Kuramoto model with different regular and random coupling configurations (see a review paper [4] for more details). Historically, the emergence of patterns of synchrony was studied in the Kuramoto model, under the assumption of an infinitely large network size, allowing for the mean field approximation. A breakthrough in the rigorous study of the infinite-dimensional Kuramoto model was made with the discovery of the Ott-Antonsen ansatz [76] which reduces the analysis of a restricted class of phase states to low dimensional dynamics [7, 76, 65]. Motivated by real-world finite-size networks, the interest has now shifted towards the analysis of finite-dimensional Kuramoto models [53, 81, 63, 85, 20].

When oscillators in the classical Kuramoto model have identical frequencies, the network has no coupling threshold and complete synchronization is locally stable for any, arbitrarily weak coupling strength [4]. This had been the main obstacle in realizing that the identical oscillators can also exhibit complex patterns of synchrony whose emergence may be hidden by the stable synchronous state. This general perception of somewhat uninspiring dynamics of identical Kuramoto models has changed with the discovery of chimera states [77, 2, 1, 77] in which structurally and dynamically identical oscillators spontaneously break into groups where some oscillators synchronize whereas the others remain incoherent. There is now a vast literature on the study of chimera states in the Kuramoto model as well as in other models of biological and mechanical systems (see an extensive review [77] for more details and references). Most studies of the stability of chimera states are numerical, with the exception of a few theoretical investigations, including the ones performed for large[75, 109] and small networks [6, 78] of 1-D phase oscillators.

The original Kuramoto model of one-dimensional (1D) oscillators was extended to a model of two-dimensional (2D) phase oscillators with inertia [42]. This modification made the 2D oscillators capable of adjusting their natural frequencies and allowed the Kuramoto

second-order oscillator network to become a more adequate model of real-world networks, including neural, mechanical and power grid systems [105]. As a result, networks of Kuramoto oscillators with inertia can exhibit a rich array of dynamics including complex synchronization transitions [100, 101, 56, 69], hysteresis [74] and bistability of synchronous clusters [14], intermittent chaotic chimeras [73], reentrant synchronous regimes [58], and solitary states [54, 64]. In particular, it was numerically demonstrated that weak chimera states can appear in small networks composed of only three Kuramoto oscillators with inertia [64]. These so-called weak chimera states are characterized by the formation of a synchronized two-oscillator cluster and one incoherent oscillator which rotates at a different frequency and can exhibit periodic or chaotic dynamics [64]. Such smallest chimera states in the three-node network can also be viewed as a proxy of a two-cluster pattern in a three-group network of identical Kuramoto oscillators with inertia. In this setting, the oscillators can synchronize within each group and two groups in turn can synchronize between each other, while leaving the dynamics of the third group incoherent. The emergence of these and more complex clusters of synchrony in multi-population Kuramoto networks with inertia calls for an analytical study to isolate the principal bifurcations and stability mechanisms underpinning the co-existence of stable clusters with complex, possibly, chaotic dynamics. This thesis seeks to establish such an analytical insight.

The layout of this thesis is as follows. In Chapter 2, we study the co-existence of stable patterns of synchrony in two coupled populations of identical Kuramoto oscillators with inertia. The two populations have different sizes and can split into two clusters where the oscillators synchronize within a cluster while there is a phase shift between the dynamics of the two clusters. Due to the presence of inertia, which increases the dimensionality of the oscillator dynamics, this phase shift can oscillate, inducing a breathing cluster pattern. We derive analytical conditions for the co-existence of stable two-cluster patterns with constant and oscillating phase shifts. We demonstrate that the dynamics, that governs the bistability of the phase shifts, is described by a driven pendulum equation. We also demonstrate how inertia affects the hysteretic transitions between the patterns. Our stability results also shed

light on the emergence of transient and stable chimeras.

In Chapter 3, we study the emergence of stable clusters of synchrony with complex intercluster dynamics in a three-population network of identical Kuramoto oscillators with inertia. We extend our results on the bistability of synchronized clusters in the two-population network and demonstrate that the addition of a third population can induce chaotic intercluster dynamics. This effect can be captured by the old adage "two is company, three is a crowd," which suggests that the delicate dynamics of a romantic relationship may be destabilized by the addition of a third party, leading to chaos. Through rigorous analysis and numerics, we demonstrate that the intercluster phase shifts can stably coexist and exhibit different forms of chaotic behavior, including oscillatory, rotatory, and mixed-mode oscillations. We also discuss the implications of our stability results for predicting the emergence of chimeras and solitary states. Finally, the Appendix contains two of the Python scripts used to analyze and simulate the three-population network of 2D oscillators. In particular, it contains a Python code for calculating winding numbers associated with a phase shift cluster solution in the three-population network. These numbers characterize regular and chaotic phase shift dynamics in the three-population Kuramoto model, so that the interested reader might find this Python code useful for further exploring new types of dynamical effects and cooperative structures in multipopulation networks of phase oscillators.

CHAPTER 2

BISTABILITY OF PATTERNS OF SYNCHRONY IN TWO-POPULATION NETWORKS OF KURAMOTO OSCILLATORS WITH INERTIA

2.1 Introduction

Pattern synchronization has been shown to be central for the functioning of a wide spectrum of biological and technological networks [32, 36, 48, 102, 70, 43, 68]. Two important cooperative rhythms of pattern dynamics are complete and cluster synchronization. Complete synchronization, in which all oscillators evolve in unison, and its dependence on network structure have received a great deal of attention in the literature [79, 28, 17, 10, 72]. Cluster synchronization is observed when the network splits into groups of coherent oscillators but the dynamics between the groups is asynchronous [16, 18, 83, 84, 8, 46, 45, 106, 80, 12, 57]. The existence of clusters of perfect synchrony in networks of identical oscillators is strictly defined by intrinsic symmetries of the network [46, 45]. These symmetries are defined as permutations of the nodes that preserve all internal dynamics and all couplings [106]. Permissible cluster partitions in a given complex network can be found via available combinatorial algorithms [12, 57].

Central questions in the study of cluster synchronization are (i) under what conditions are the clusters stable? and (ii) do the clusters defined by perfect symmetries persist under parameter mismatch? These stability [16, 83, 84, 80] and persistence [8] questions have been addressed for different classes of dynamical networks; yet, the full picture is far from being complete.

Inspired by the adaptive frequency model of firefly synchronization [42] where the oscillators are capable of adjusting their natural frequencies, the classical Kuramoto model of 1-D phase oscillators was extended to a model of 2-D oscillators with inertia [100, 101]. This Kuramoto model with inertia was shown to exhibit various synchronization transitions

[100, 101, 56] and hysteristic phenomena [74], including intermittent chaotic chimeras [73] and reentrant synchronous regimes [58]. Existing analytical studies of the collective dynamics of the Kuramoto model with inertia mainly aim at (i) the stability of complete synchronization [40, 34, 49], (ii) bifurcations leading to its loss[21], and (iii) non-trivial phase transitions to synchrony in the presence of noise [58].

Despite significant interest among physicists and applied mathematicians, the emergence and hysteretic transitions between stable clusters in Kuramoto networks of identical oscillators have still not been fully understood. Rigorous analysis of the stability of clusters and chimeras in the finite-size Kuramoto model has proved to be challenging, and most existing results are numerical.

In this chapter, we contribute toward the rigorous understanding of the co-existence of stable patterns of synchrony in two symmetrically coupled populations of identical Kuramoto oscillators with inertia. We derive exact results on the stability of a two-cluster synchronous state in which the population splits into two clusters of synchronized oscillators, but there is no synchrony between the clusters. We reduce the system, governing the dynamics of the phase shift between the clusters, to the pendulum equation [5]. As a result, the phase shift between the clusters can remain constant or can periodically rotate its phase, depending on the choice of initial conditions. This yields the bistability of patterns of synchrony where a pattern with a constant inter-cluster phase shift stably co-exists with a breathing pattern when the inter-cluster phase shift evolves in time. Our stability analysis also addresses the emergence of transient and stable chimeras. The results presented in this chapter were published in [14].

The layout of this Chapter is as follows. First, in Sec. 2.2, we present and discuss the network model. In Sec. 2.3, we study the existence of synchronous clusters and perform the analysis that allows for describing the dynamics of the synchronous clusters in terms of the limit sets of the pendulum equation. We derive the conditions on the bistability of synchronous dynamics which are explicit in parameters of the network model. In Sec. 2.4, we analyze the variational equations for the stability of the synchronous cluster and obtain

the main stability results of this paper. In Sec. 2.5, we present a numerical example which supports our analytical results. Finally, Section 2.6 contains concluding remarks.

2.2 Two-group network: identical rotators, different group sizes

Following previous studies in networks of Kuramoto models without [1, 78] and with inertia [73], we consider a two-group network of 2-D rotators

$$\begin{aligned} m\ddot{\theta}_i + \dot{\theta}_i &= \omega + \tfrac{\mu}{N+M}\sum_{j=1}^{N}\sin(\theta_j - \theta_i - \alpha) \\ &+ \tfrac{\nu}{N+M}\sum_{j=1}^{M}\sin(\varphi_j - \theta_i - \alpha),\ i = 1, ..., N \\ m\ddot{\varphi}_k + \dot{\varphi}_k &= \omega + \tfrac{\mu}{N+M}\sum_{j=1}^{M}\sin(\varphi_j - \varphi_k - \alpha) \\ &+ \tfrac{\nu}{N+M}\sum_{j=1}^{N}\sin(\theta_j - \varphi_k - \alpha),\ k = 1, ..., M. \end{aligned} \tag{2.1}$$

Here, the network is divided into two groups of oscillators of sizes N and M, with all-to-all symmetrical coupling within and between the two groups, such that the intragroup coupling strength, μ, is stronger than the intergroup coupling strength, ν. Variables θ_i and φ_k represent the phases of oscillators in the first and second groups, respectively. The oscillators are assumed to be identical, with identical frequency ω, phase lag $\alpha \in [0, \pi/2)$ and inertia m. The model (2.1) is an extension of the Abrams *et al.* chimera model[1, 78], consisting of two groups of 1-D phase oscillators with Kuramoto-Sakaguchi coupling [59, 88]. In the model (2.1), we use the 2-D Kuramoto oscillator with inertia as the individual cell model and consider non-equal group sizes. These two properties will allow for deriving analytical conditions on the stability of clusters of synchrony, exhibiting two types of co-existing behavior where (i) the phase between the synchronized clusters remains fixed and (ii) the phase between the clusters oscillates.

By rescaling time $\tau = \mu t/(N+M)$ and parameter $\beta = \mu m/(N+M)$, and using a rotating frame of reference $\Theta_i = \theta_i - \omega t + c$, $\Phi_k = \varphi_k - \omega t + c$, where c is a constant, we can

cast the model (2.1) into a more compact form

$$\begin{aligned}
\beta\ddot{\Theta}_i + \dot{\Theta}_i &= \sum_{j=1}^{N} \sin(\Theta_j - \Theta_i - \alpha) \\
&+ \gamma \sum_{j=1}^{M} \sin(\Phi_j - \Theta_i - \alpha),\ i = 1, ..., N \\
\beta\ddot{\Phi}_k + \dot{\Phi}_k &= \sum_{j=1}^{M} \sin(\Phi_j - \Phi_k - \alpha) \\
&+ \gamma \sum_{j=1}^{N} \sin(\Theta_j - \Phi_k - \alpha),\ k = 1, ..., M,
\end{aligned} \tag{2.2}$$

where $\gamma = \nu/\mu$ represents the ratio between the intra- and intergroup couplings such that $\gamma \in (0, 1)$.

2.3 Existence of synchronous clusters

2.3.1 Cluster partition

The connectivity matrix G of network (2.2) has a block structure

$$G = \begin{pmatrix} J_{N,N} & \gamma J_{N,M} \\ \gamma J_{M,N} & J_{M,M} \end{pmatrix} \tag{2.3}$$

where $J_{N,N}$, $J_{M,M}$, $J_{N,M}$, and $J_{M,N}$ are $N \times N$, $M \times M$, $N \times M$, and $M \times N$ all-ones matrices, respectively.

In general, clusters of perfect synchrony are determined by a network decomposition into the disjoint subsets of oscillators $V = V_1 \cup ... \cup V_d$, $V_p \cap V_q = \emptyset$ defined by the equalities of the oscillator states. If this cluster decomposition is flow-invariant with respect to the vector field of the network system, then the corresponding manifold $D(d)$ is invariant and defines d synchronous clusters. Synchronous clusters exist if the graph vertices have a corresponding balanced coloring [46, 45, 106]. Every cluster corresponds to a coloring in which two oscillators have the same color if and only if their states are completely synchronized. Oscillators colored in this way create a coloring map. A coloring of the vertices is balanced, if each oscillator of color i has the same number of inputs from the oscillators of color j, for

all i and j. A minimal balanced coloring is a balanced coloring with the minimal number of colors.

In the context of the network (2.2), a necessary condition for oscillators to form a cluster is the equal row sum constraint. In fact, the first N rows of matrix G, corresponding to the first group of oscillators, have row sums equal to $N+\gamma M$. The remaining M rows are defined by the connectivity of the second group and equal to $M+\gamma N$. As a result, the minimal cluster partition has two colors. The corresponding cluster synchronization manifold

$$D(2) = \{\Theta_1 = ... = \Theta_N = \Theta, \dot{\Theta}_1 = ...\dot{\Theta}_N = \dot{\Theta},\ \Phi_1 = ... = \Phi_M = \Phi, \dot{\Phi}_1 = ...\dot{\Phi}_M = \dot{\Phi}\} \quad (2.4)$$

defines two clusters of synchrony. As the two groups of oscillators are formed by all symmetrical all-to-all networks, all other combinations of cluster partitions within the two clusters are also possible. This includes so-called chimeras [78], where the first group of N oscillators is completely synchronized, and all M oscillators from the second group are desynchronized; this state is defined by the cluster synchronization manifold $D(M+1) = \{\Theta_1 = ... = \Theta_N, \dot{\Theta}_1 = ...\dot{\Theta}_N,\ \Phi_1, ..., \Phi_M, \dot{\Phi}_1, ..., \dot{\Phi}_M\}$. Note that complete synchronization is impossible in the network (2.2) as $N \neq M$ and the equal row sum constraint is not respected.

In the following, we will focus on the dynamics on the two-cluster synchronization manifold $D(2)$ and the conditions of its transversal stability.

2.3.2 Dynamics on the cluster manifold

2.3.2.1 Transformation to the pendulum equation The dynamics on the manifold $D(2)$ is defined by the following system

$$\begin{aligned} \beta\ddot{\Theta} + \dot{\Theta} &= -N\sin\alpha + \gamma M \sin(\Phi - \Theta - \alpha) \\ \beta\ddot{\Phi} + \dot{\Phi} &= -M\sin\alpha + \gamma N \sin(\Theta - \Phi - \alpha) \end{aligned} \quad (2.5)$$

obtained from the system (2.2) by omitting the subscripts i, j and k.

For convenience, we rotate the coordinate frame and introduce new variables

$$\begin{aligned} x &= \Phi - \Theta \\ y &= \Theta + \kappa\Phi, \quad \text{where } \kappa = M/N < 1. \end{aligned} \tag{2.6}$$

The addition of the factor κ to the standard change of basis for the difference and sum variables is not necessary; however, it will make the sum variable y strictly decreasing, therefore making the analysis simpler.

In terms of x and y, the system (2.5) can be rewritten as follows:

$$\beta\ddot{x} + \dot{x} = (N - M)\sin\alpha - \gamma(N\sin(x + \alpha) + M\sin(x - \alpha)) \tag{2.7a}$$

$$\beta\ddot{y} + \dot{y} = -(N + \kappa M)\sin\alpha + \gamma M(\sin(x - \alpha) - \sin(x + \alpha)). \tag{2.7b}$$

We use the following trigonometric formula to simplify the equation (2.7a):

$$N\sin(x + \alpha) + M\sin(x - \alpha) = ((M + N)\cos\alpha)\sin x + ((N - M)\sin\alpha)\cos x = R\sin(x + \delta),$$

where $R = \gamma\sqrt{N^2 + M^2 + 2MN\cos 2\alpha}$ and the angle δ is introduced to make the expression more manageable, with $\cos\delta = \frac{N+M}{R}\cos\alpha$ and $\sin\delta = \frac{N-M}{R}\sin\alpha$, yielding $\tan\delta = \frac{N-M}{N+M}\tan\alpha = \frac{1-\kappa}{1+\kappa}\tan\alpha$. Similarly simplifying the right-hand side of (2.7b), we turn the system (2.7a)-(2.7b) into the following form:

$$\beta\ddot{x} + \dot{x} = \Omega - R\sin(x + \delta) \tag{2.8a}$$

$$\beta\ddot{y} + \dot{y} = -(\tilde{\Omega} + 2\gamma M\cos x)\sin\alpha, \tag{2.8b}$$

where $\Omega = (N - M)\sin\alpha$, $\tilde{\Omega} = \frac{N^2+M^2}{N}$, and $\delta = \arctan\left(\frac{1-\kappa}{1+\kappa}\tan\alpha\right)$, with $\kappa = M/N$.

The shift $x + \delta \to x$ transforms the system (2.8a)-(2.8b) into the form:

$$\beta\ddot{x} + \dot{x} + R\sin(x) = \Omega \tag{2.9a}$$

$$\beta\ddot{y} + \dot{y} = -(\tilde{\Omega} + 2\gamma M\cos(x-\delta))\sin\alpha. \tag{2.9b}$$

Note that equation (2.9a), governing the difference dynamics between the clusters, does not depend of the sum variable y, such that equation (2.9a) drives equation (2.9b). Remarkably, equation (2.9a) is the equation of a pendulum, with a constant torque Ω, [5] as well as the model of a shunted Josephson junction [22]. Its dynamics on the cylinder ($x \bmod 2\pi$, $\dot{x} = v$) are known to exhibit various interesting dynamical regimes, including bistability where a stable equilibrium co-exists with a stable limit cycle. Figure 2.1 illustrates the well-known stability diagram [96, 22] that indicates possible dynamics as a function of bifurcation parameters Ω, R, and β. Two bifurcation curves separate the stability diagram into three regions of parameters. The curve $\Omega/R = 1$ corresponds to a saddle-node bifurcation of equilibria. The curve $\Omega/R = T(h)$ with $h = 1/\sqrt{\beta R}$ is the Tricomi curve [103] that indicates a homoclinic bifurcation of the saddle where the homoclinic orbit encircles the cylinder and forms a saddle connection. The two curves meet at $h^* \approx 1.22$ [5, 47]. While the closed-form derivation of the Tricomi curve is not available, we suggest the following nonlinear function $T(h)$ as an approximation of the Tricomi curve:

$$T(h) = \frac{4}{\pi}h - 0.305h^3 = \frac{4}{\pi\sqrt{\beta R}} - 0.305(\beta R)^{-3/2}. \tag{2.10}$$

This approximation matches the numerically calculated Tricomi curve remarkably well (see Fig. 2.1) and will be used for the derivation of the bistability conditions of cluster synchrony in Statement 1.

The three stability regions of parameters in the pendulum equation (2.8a) are as follows.

Region I: A stable equilibrium.

$$\frac{\Omega}{R} < \begin{cases} T(h), & 0 < h < h^* \\ 1, & h > h^*. \end{cases} \tag{2.11}$$

In this region, system (2.8a) has two fixed points on the cylinder: a saddle at $x = \pi - \arcsin\frac{\Omega}{R} + \delta$ and a stable equilibrium (node or focus) at

$$x_e = \arcsin\frac{\Omega}{R} - \delta. \tag{2.12}$$

Region II: Co-existence.

$$T(h) < \frac{\Omega}{R} < 1, \quad 0 < h < h^*. \tag{2.13}$$

Here, the stable equilibrium at x_e co-exists with a stable limit cycle which emerged from the homoclinic orbit of the saddle at $\Omega/R = T(h)$. $x_c(t)$ denotes the x-coordinate of the stable limit cycle. The attraction basins of the stable equilibrium and the limit are separated by a stable manifold of the saddle (Fig. 2.1).

Region III: A globally stable limit cycle. For $\frac{\Omega}{R} > 1$, system (2.8a) only has a globally stable limit cycle as the saddle and the stable node had disappeared via the saddle-node bifurcation at $\Omega/R = 1$. The stable limit cycle corresponds to rotation around the cylinder.

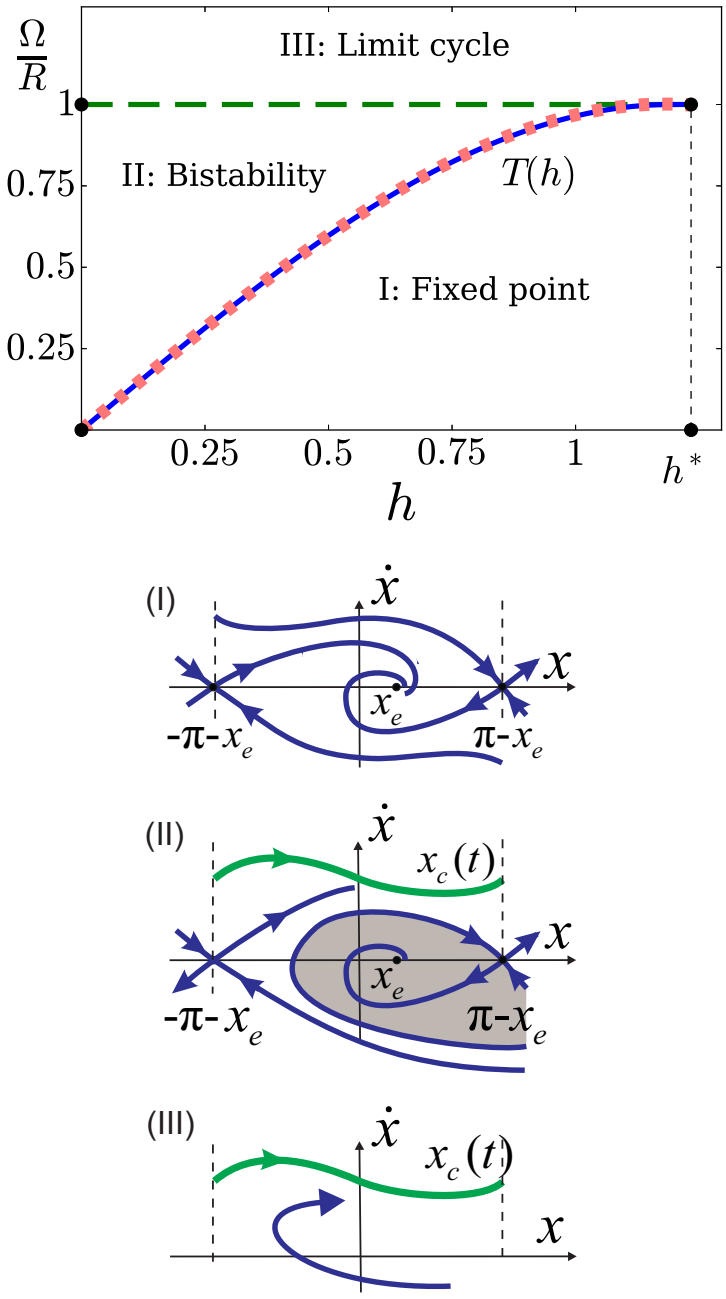

Figure 2.1: Bifurcation diagram $(h, \frac{\Omega}{R})$. The saddle-node (green dashed) horizontal line and the Tricomi (blue solid) curve $T(h)$ divide the diagram into regions I, II, and III. The Tricomi curve, corresponding to a homoclinic bifurcation of the saddle, is calculated numerically. Its nearly perfect analytical approximation $\frac{\Omega}{R} = T(h) = \frac{4}{\pi}h - 0.305h^3$, used in the bistability condition (2.18), is depicted by the red dashed line. (I-III). Schematic phase portraits. In (II), the stable limit cycle $x_c(t)$ co-exists with the stable fixed point x_e. The shaded area is the basin of attraction of the fixed point x_e.

Equation (2.8b) for the sums of the cluster coordinates is driven by (2.8b) via $x(t)$. Therefore, as long as $\tilde{\Omega}+2\gamma M\cos x>0$, any solution of (2.8b) eventually satisfies $\dot{y}<0$ and $y(t)$ monotonically decreases in time. In particular, the time-dependent solution $(y_e,\dot{y_e})$ of (2.8b), corresponding to the stable fixed point x_e in (2.8a), is obtained by integrating (2.8b) such that

$$y_e=-([(\tilde{\Omega}+2M\gamma\cos x_e)\sin\alpha]t+y_0), \tag{2.14}$$

where y_0 is a constant of integration. The solution $(y_c,\dot{y_c})$, corresponding to the limit cycle x_c in (2.8b), is not given explicitly.

Thus, we can conclude that three distinct dynamics of system (2.8a) in regions I, II, and III yield three dynamical regimes on the cluster manifold $D(2)$ in the network system (2.2).

2.3.2.2 Cluster phase shifts **I. Constant phase shift (region I).** Governed by the phases Φ and Θ, two clusters of synchrony have a constant phase shift $\Phi_e-\Theta_e=x_e$, where x_e is the coordinate of the stable equilibrium of the pendulum system (2.8a) and defined in (2.12). It follows from (2.5) and (2.6) that the cluster phases at x_e are defined by

$$\Theta_e=\tfrac{y_e-\kappa x_e}{1+\kappa},\quad \Phi_e=\tfrac{y_e+x_e}{1+\kappa}=\Theta_e+x_e, \tag{2.15}$$

where y_e is defined in (2.14).

As the phase shift is constant, the rotation frequencies of the two clusters become equal and are defined, according to the system (2.5), by

$$\dot{\Theta}=-N\sin\alpha+\gamma M\sin(x_e-\alpha)=\dot{\Phi}=-M\sin\alpha-\gamma N\sin(x_e+\alpha). \tag{2.16}$$

II. Co-existence of constant and oscillating phase shifts (region II). The co-existence of the stable equilibrium and the limit cycle in system (2.8a) yields the bistability of the cluster regimes. Here, the phase shift can remain constant at x_e or periodically oscillate such that $\Phi-\Theta=x_c(t)$, which is governed by the stable limit cycle. The realization of one of

the cluster regimes depends on initial conditions.

III. Oscillating phase shift (region III). Defined by the globally stable limit cycle in (2.8a), the phase difference between the clusters, establishing from any conditions on the cluster manifold M, periodically oscillates such that

$$\Theta_c = \tfrac{y_c-\kappa x_c}{1+\kappa}, \quad \Phi_c = \tfrac{y_c+x_c}{1+\kappa} = \Theta_c + x_c(t) \ . \tag{2.17}$$

The bistability condition (2.13) can be expressed in terms of the original parameters of the network system (2.2). This leads to the following assertion.

Statement 1. *The constant and oscillating phase shifts $x = \Phi - \Theta$ between two clusters on the cluster manifold $D(N)$ in the network system (2.2) co-exist if*

$$\alpha_{\rm TR} = \arctan \frac{1+\kappa}{1-\kappa} \frac{\gamma T(h)}{\sqrt{1-(\gamma T(h))^2}} < \alpha < \arctan \frac{1+\kappa}{1-\kappa} \frac{\gamma}{\sqrt{1-\gamma^2}} = \alpha^*, \tag{2.18}$$

where $\kappa = M/N$, $T(h) = \frac{4}{\pi\sqrt{\beta R}} - 0.305(\beta R)^{-3/2}$, and $R = \gamma\sqrt{N^2+M^2+2MN\cos 2\alpha}$. The left hand side of the inequality (2.18) is defined by $\alpha_{\rm TR}$ which corresponds to the Tricomi curve (2.11). The right hand side is determined by the critical value α^*, for which system (2.8a) undergoes the saddle-node bifurcation at $\frac{\Omega}{R} = 1$, where $\Omega = (N-M)\sin\alpha$. Condition (2.18) can also be cast in the alternative, more compact form

$$\frac{4}{\pi\sqrt{\beta R}} - 0.305(\beta R)^{-3/2} < \frac{\Omega}{R} < 1. \tag{2.19}$$

In the following section, we will derive conditions on the stability of the clusters. In particular, we will combine the stability conditions with the co-existence condition of Statement 1 to determine the parameter regions of two co-existing stable cluster regimes with constant and oscillating shifts. We will also discuss conditions for the emergence of chimeras when one cluster of oscillators remains stable while the other cluster disintegrates.

2.4 Stability of clusters

Linearizing the network system (2.2) about the synchronous cluster solution (2.4) $(\Theta, \dot{\Theta}, \Phi, \dot{\Phi})$, we obtain the variational equations for the local stability of the cluster manifold $D(2)$

$$\begin{aligned}
\beta\ddot{\xi}_i + \dot{\xi}_i &= -\left(N\cos\alpha + \gamma M\cos(x_s-\alpha)\right)\xi_i + \cos\alpha\sum_{j=1}^{N}\xi_j + \gamma\cos(x_s-\alpha)\sum_{j=1}^{M}\eta_j,\ i=1,...,N \\
\beta\ddot{\eta}_k + \dot{\eta}_k &= -\left(M\cos\alpha + \gamma N\cos(x_s+\alpha)\right)\eta_k + \cos\alpha\sum_{j=1}^{M}\eta_j + \gamma\cos(x_s+\alpha)\sum_{j=1}^{N}\xi_j,\ k=1,...,M.
\end{aligned} \tag{2.20}$$

Here, ξ_i is an infinitesimal perturbation of the i-th oscillator's synchronous solution in the larger N-cluster, and η_k corresponds to the smaller M-cluster. x is the cluster phase shift as defined above. System (2.20) can be rewritten in the matrix form

$$\beta\ddot{V} + \dot{V} = AV, \tag{2.21}$$

where vector $V = \text{column}(\xi_1, ..., \xi_N, \eta_1, ..., \eta_M)$. Matrix A is the Jacobian

$$A = \begin{pmatrix} cJ_{N,N} - (Nc + Mc^-)I_N & c^-J_{N,M} \\ c^+J_{M,N} & cJ_{M,M} - (Mc + Nc^+)I_M \end{pmatrix}, \tag{2.22}$$

where $c = \cos\alpha$, $c^- = \gamma\cos(x_s-\alpha)$, $c^+ = \gamma\cos(x_s+\alpha)$, I_N and I_M are identity matrices, and $J_{N,N}$, $J_{N,M}$, and $J_{M,N}$ are all-ones matrices.

2.4.1 Stability along the cluster manifold

The $(N+M)\times(N+M)$ Jacobian A has equal zero-row sums. Therefore, it contains one zero eigenvalue that corresponds to equation (2.8b), which governs the rotating frame coordinate y on the cluster manifold $D(2)$. An eigenvector $V_{\text{syn}} = \text{column}(\underbrace{\xi, ..., \xi}_{N}, \underbrace{\eta, ..., \eta}_{M})$

determines the direction along the cluster manifold $D(2)$. The corresponding eigenvalue

$$\lambda_s = -Nc^+ - Mc^- = -\gamma(N\cos(x_s+\alpha) + M\cos(x_s-\alpha)), \quad s = e, c \tag{2.23}$$

defines the stability of the fixed point $x = x_e$ or the limit cycle $x = x_c(t)$ in the pendulum equation (2.8a) which governs the dynamics of the cluster shift on the cluster manifold $D(2)$.

Case I: Fixed point x_e.

If the dynamics on the cluster manifold is governed by the fixed point $x_e = \arcsin\frac{\Omega}{R} - \delta$ (cf. (2.12)), the stability of the constant phase shift between the two clusters is defined via the eigenvalue (2.23) such that

$$-\lambda_e = \gamma(N\cos(x_e+\alpha) + M\cos(x_e-\alpha)) > 0. \tag{2.24}$$

This condition holds true as long as $\frac{\Omega}{R} < 1$ and the stable fixed point exists in region I (cf. Fig. 2.1).

Case II: Limit cycle $x_c(t)$.

In this case, the eigenvalue λ_c is defined by the time-varying phase shift $x_c(t)$. The stability of the limit cycle is defined by the variational equation

$$\beta\ddot{\zeta} + \dot{\zeta} - \lambda_c(t)\zeta = 0, \tag{2.25}$$

written for the perturbations ζ to the limit cycle of system (2.7a). The stability of the cycle in equation (2.25) is defined by the Lyapunov characteristic exponents. One of the exponents is zero and corresponds to the direction along the limit cycle, whereas the other is negative as the divergence of the vector field of (2.7a) is negative, $\mathrm{div}F(x = v, \dot{v}) = -1/\beta < 0$. Therefore, the limit cycle x_c is stable and determines the stability of the synchronous solution on the cluster manifold $D(2)$.

2.4.2 Transversal stability

To demonstrate that the synchronous clusters can stably appear in the network (2.2), we shall prove the transversal stability of the cluster manifold $D(2)$. We introduce the difference variables

$$\begin{aligned} u_i &= \xi_i - \xi_{i+1}, \quad i = 1, ..., N-1 \\ w_k &= \eta_k - \eta_{k+1}, \quad k = 1, .., M-1 \end{aligned} \tag{2.26}$$

whose convergence to zero will imply the transversal stability of $D(2)$. Subtracting the $(i+1)$-th $[(k+1)$-th] equation from the i-th $[k$-th] equation in system (2.21)-(2.22), we obtain the variational equations for the transversal stability:

$$\beta \ddot{u}_i + \dot{u}_i + q_1 u_i = 0, \quad i = 1, ..., N-1 \tag{2.27a}$$

$$\beta \ddot{w}_i + \dot{w}_i + q_2 w_i = 0, \quad i = 1, ..., M-1, \tag{2.27b}$$

where

$$q_1 = Nc + Mc^- = N\cos\alpha + \gamma M \cos(x_s - \alpha) \tag{2.28a}$$

$$q_2 = Nc^+ + Mc = N\gamma \cos(x_s + \alpha) + M\cos\alpha. \tag{2.28b}$$

Here, q_1 and q_2 are eigenvalues of the Jacobian A in (2.22) which have multiplicities $N-1$ and $M-1$, respectively. Note that the equations (2.28a) and (2.28b) are uncoupled. The analysis of the stability equations (2.28a)-(2.28b) leads to the following assertions.

Theorem 1. [Stability of the cluster solution with a constant phase shift].
Let the parameters satisfy the condition $\Omega/R < 1$, *then the cluster solution (2.4)* $(\Theta, \dot{\Theta}, \Phi, \dot{\Phi})$ *with the constant phase shift* x_e *is locally stable to transversal perturbations iff*

$$\alpha < \alpha^{\rm cr}, \tag{2.29}$$

where the critical value $\alpha^{\rm cr}$ *is the solution of the equation*

$$q_2 = \gamma\cos(x_e+\alpha) + \kappa\cos\alpha = 0. \tag{2.30}$$

Here, $\gamma \in (0,1)$ *is the coupling ratio,* x_e *is defined via (2.12),* $\kappa = M/N$*, and* $\alpha \in [0,\alpha^*)$*, where* $\alpha^* = \arctan\frac{1+\kappa}{1-\kappa}\frac{\gamma}{\sqrt{1-\gamma^2}}$ *(see (2.18)). Positive values of* q_2 *correspond to* $\alpha < \alpha^{\rm cr}$ *and define the stability of the cluster solution.*

Proof. The condition $\Omega/R < 1$ implies that the pendulum equation (2.8a), governing the dynamics of the phase shift x on the cluster manifold $D(2)$, has a stable equilibrium point $x_e = \arcsin\frac{\Omega}{R} - \delta$ (see Fig. 1). Therefore, functions (2.28a)-(2.28b), q_1 and q_2, must be evaluated at x_e. The stability of the variational system (2.27a)-(2.27b) is guaranteed iff

$$q_1 = \cos\alpha + \gamma\kappa\cos(x_e-\alpha) > 0 \tag{2.31a}$$

$$q_2 = \gamma\cos(x_e+\alpha) + \kappa\cos\alpha > 0. \tag{2.31b}$$

This is due to the fact that $q_{1,2} > 0$ is required for the real parts of the roots of the characteristic equations $\beta s^2 + s + q_{1,2} = 0$ for (2.27a)-(2.27b) to be negative. Note that $\cos\alpha > 0$ and $\cos(x_e-\alpha) > 0$ for $\alpha \in [0,\pi/2)$ in (2.31a), and therefore $q_1 > 0$.

The phase shift x_e is a monotonically increasing function of α. Therefore, the function q_2 monotonically decreases and can become negative when increasing α. As a result, there is a critical value $\alpha^{\rm cr}$ for which q_2 becomes 0. Finding $\alpha^{\rm cr}$ amounts to solving $q_2 = \gamma\cos(x_e+\alpha) + \kappa\cos\alpha = 0$. While this equation cannot be solved for α in closed form, $\alpha^{\rm cr}$ can be directly calculated for given values of N, M, and γ. This concludes the proof. □

Corollary 1. [Sufficient condition]. *If the relative size of the two clusters* $\kappa = M/N$ *satisfies the following sufficient condition*

$$\kappa < 1 - 2\gamma^2, \tag{2.32}$$

then the cluster solution $(\Theta, \dot\Theta, \Phi, \dot\Phi)$ *is locally stable to transversal perturbations for any*

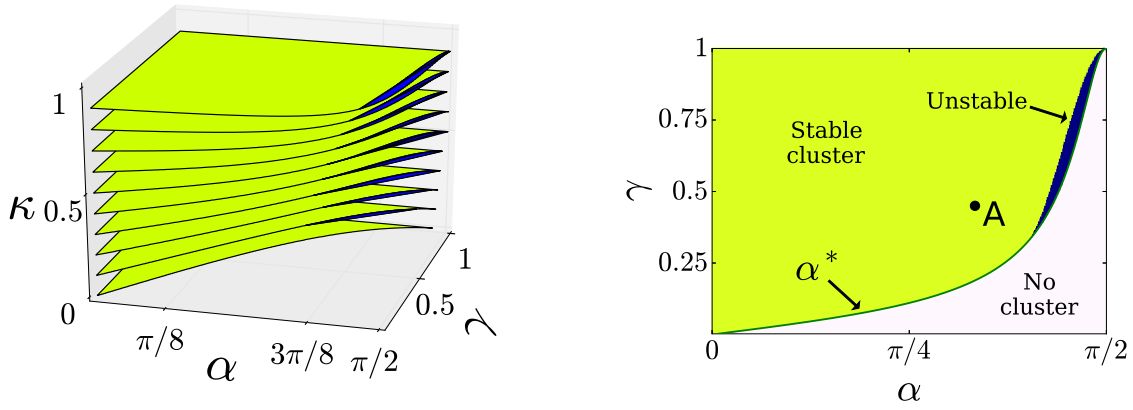

(a) (b)

Figure 2.2: Illustration of the stability condition $q_2 = \gamma\cos(x_e+\alpha)+\kappa\cos\alpha > 0$ in Theorem 1. Yellow (light) regions are defined by $q_2 > 0$ and correspond to the stable cluster with a constant shift. Instability regions with $q_2 < 0$ are depicted in dark blue. The cluster with a constant shift does not exist in white regions. (a). 3-D diagram with 2-D cuts at various discrete $\kappa = M/N$. (b). 2-D cut at $\kappa = 0.8$. The curve α^* separates the regions of existence (yellow/blue) and non-existence (white). Point A corresponds to the parameters used in Fig. 2.4.

$\alpha \in [0, \alpha^*)$.

Proof. The maximum value of $\alpha^{\rm cr}$ is bounded by α^* that corresponds to the saddle-node bifurcation of the fixed point x_e at $\Omega/R = 1$. Therefore, this bound gives the constraints on γ and κ that can be calculated from

$$q_2 = \gamma\cos(x_e+\alpha^*)+\kappa\cos\alpha^* > 0. \tag{2.33}$$

As $x_e(\alpha^*) = \pi/2 - \arcsin\gamma = \pi/2 - \arctan\frac{\gamma}{\sqrt{1-\gamma^2}}$, we get $\cos(x_e+\alpha^*) = \sin(\arcsin\gamma - \alpha^*) = \gamma\cos\alpha^* - \sqrt{1-\gamma^2}\sin\alpha^*$. Therefore, the condition (2.33) can be rewritten as follows

$$q_2 = (\gamma^2+\kappa)\cos\alpha^* - \gamma\sqrt{1-\gamma^2}\sin\alpha^* > 0. \tag{2.34}$$

It further transforms into

$$\tan\alpha^* < \frac{\gamma^2+\kappa}{\gamma\sqrt{1-\gamma^2}}. \tag{2.35}$$

At the same time $\tan\alpha^* = \frac{1+\kappa}{1-\kappa}\frac{\gamma}{\sqrt{1-\gamma^2}}$ (see Statement 1), therefore condition (2.35) becomes

$$\frac{1+\kappa}{1-\kappa}\frac{\gamma}{\sqrt{1-\gamma^2}} < \frac{\gamma^2+\kappa}{\gamma\sqrt{1-\gamma^2}} \tag{2.36}$$

and yields the sufficient condition $\kappa < 1 - 2\gamma^2$. This concludes the proof of Corollary 1. □

Figure 2.2 illustrates the conditions of Theorem 1 for $q_2 > 0$ and demonstrates that the stable cluster with a constant shift exists in a wide region of parameters α, γ, κ. Notice that $\alpha^{\rm cr}$, which separates the stability and instability regions, coincides with α^* for a significant (lower) part of the curve α^* (see Fig. 2.2b). Hence, in this region of $\alpha \in [0, 1.26056)$ and $\gamma \in [0, 0.3275)$, the cluster with a constant shift, defined by the stable fixed point x_e of equation (2.7a), remains stable as long as it exists. For values $\gamma \geq 0.3275$, the cluster becomes unstable at $\alpha^{\rm cr} < \alpha^*$ and remains unstable until it ceases to exist at α^* (see the dark blue instability region in Fig. 2.2b).

Remark 1. If the size of the cluster groups is equal so $N = M$, then cluster synchronization turns into complete synchronization with phase shift $x_e = 0$. As a result, the stability condition (2.29) in Theorem 1 holds true for any $\alpha \in [0, \alpha^*)$, so complete synchronization is always (locally) stable. In regard to Fig. 2.2a, the corresponding horizontal cut at $\kappa = M/N = 1$ contains no unstable region, and $q_2 > 0$ for any $\alpha \in [0, \alpha^*)$ (this top cut is not shown for a better visibility of lower cuts $\kappa \in [0.1, 0.9]$).

Remark 2. If $\gamma = \kappa$, then $\alpha^{\rm cr}$ from the stability condition (2.29) can be explicitly calculated and equals $\alpha^{\rm cr} = \pi/2 - x_e/2$. This follows from the equation (2.30) where γ can be replaced by $\kappa = \frac{M}{N}$. Therefore, equation (2.30) simplifies to $\cos(x_e + \alpha) + \cos\alpha = 2\cos\frac{x_e+\alpha}{2}\cos\frac{x_e-\alpha}{2} = 0$ which holds true if $\alpha = \alpha^{\rm cr} = \pi/2 - x_e/2$.

Remark 3. [Relation to the stability of chimeras]. When condition (2.29) is violated such that the function $q_2 < 0$, the two-cluster pattern loses its stability (see Fig. 2.2). As it follows from the variational equations (2.27a)-(2.27b), the stability of the N-cluster of

synchronous oscillators $(\Theta, \dot{\Theta})$ is determined by the condition $q_1 > 0$ which holds true for any $\alpha \in [0, \pi/2)$, independent from the sign of q_2. Therefore, when q_2 changes sign from positive to negative, the trivial fixed point of the variation equations (2.27a)-(2.27b), which corresponds to the cluster manifold, becomes a saddle. This saddle point has a stable manifold of dimension $2N + M$ and an unstable manifold of dimension M, where the $2N$ stable directions correspond to the variables of the first N oscillators and are defined by the condition $q_1 > 0$. At the same time, the M unstable directions are determined by the condition $q_2 < 0$, which implies transversal instability of the M variables of the oscillators from the second cluster. A trajectory, starting close to the stable manifold of the saddle point may remain close to it, giving rise to a transient chimera, where the first cluster persists for a some fairly long amount of time, especially in a large network. This argument comes from the rigorous conditions on the stability/instability of the cluster solution (2.4) $(\Theta, \dot{\Theta}, \Phi, \dot{\Phi})$ whose stability along the cluster manifold $D(2)$ is proven. At the same time, a rigorous proof of the stability of a non-transient chimera state $D(M+1) = \{\Theta_1 = ... = \Theta_N, \dot{\Theta}_1 = ...\dot{\Theta}_N, \Phi_1, ..., \Phi_M, \dot{\Phi}_1, ..., \dot{\Phi}_M\}$ via the stability of the first cluster oscillators' variables remains elusive. This is due to the fact that the stability of the chimera state solution along the chimera manifold $D(M+1)$ cannot be rigorously assessed via the 2-D equation for the dynamics of the phase shift (2.8a) but must be proven through the full $2 \times (M+1)$ system, similar to (2.5), where Φ is replaced with $\Phi_1, ..., \Phi_M$. Although, our numerical simulations indicate the emergence of non-transient chimeras (see Fig. 2.5), where the N-cluster never disintegrates and remains stable.

Theorem 2. [Stability of the breathing cluster solution] (sufficient conditions). *Let the parameters satisfy the condition: $\Omega/R > T(h)$ (see Fig. 1) such that the system (2.8a) has a stable limit cycle which determines the oscillating phase shift $x_c(t)$ between two clusters. Then, the cluster solution (2.4)* $(\Theta, \dot{\Theta}, \Phi, \dot{\Phi})$ *with the phase shift x_c in the network system*

(2.2) is locally stable to transversal perturbations if

$$\kappa \cos\alpha > \gamma \tag{2.37a}$$

$$1 - 4\beta N(k\cos\alpha - \gamma) > 0. \tag{2.37b}$$

Proof. As in the proof of Theorem 1, we should find parameter regions for the stability of the variational equations (2.27a)-(2.27b). In contrast to the previous case of the constant phase shift x_e, the oscillating phase shift $x_c(t)$ makes q_1 and q_2 time-varying periodic functions, and therefore the variational equations (2.27a)-(2.27b) contain time-varying coefficients. While the precise bounds on the stability of (2.27a)-(2.27b) can be numerically assessed via the calculation of the Lyapunov exponents, we derive analytical estimates as follows. As in the case of the constant phase shift x_e, the necessary condition for the stability of (2.27a)-(2.27b) is $q_1(x_c(t)) > 0$ and $q_2(x_c(t)) > 0$. In this case, these two inequalities must be fulfilled for any time instant during the period of the cycle $x_c(t)$. The condition $q_1 = N\cos\alpha + \gamma M\cos(x_c(t) - \alpha) > 0$ can be estimated via the worst-case stability scenario where $\cos(x_c(t) - \alpha) = -1$. That is, $q_1(x_c(t)) > 0\ \forall t$ if $\cos\alpha > \kappa\gamma$. Similarly, we get the bound on $q_2(x_c(t)) > 0\ \forall t$ if $\cos\alpha > \gamma/\kappa$. As $\kappa < 1$, the condition for q_2 also guarantees the condition for q_1. This gives bound (2.37a).

While bound (2.37a) alone would be sufficient if q_1 and q_2 were constant, increasing β can destabilize the variational equations (2.27a)-(2.27b) with periodically varying coefficients. The destabilizing contribution of β can be assessed via a simple criterion that the discriminants D_{q_1,q_2} of the corresponding characteristic equations $\beta s^2 + s + q_{1,2}(x_c(t)) = 0$ are positive [38]. In simple words, this sufficient condition implies that as long as the origin remains a stable node fixed point of variational equations (2.27a)-(2.27b) for any fixed time instant of time and never turns into a degenerate node or a focus, the variational equations (2.27a)-(2.27b) with time-varying parameters are stable. For the worst case of $\cos(x_c(t) + \alpha) = -1$, the condition on $D_{q_2} = 1 - 4\beta q_2 > 0$ yields bound (2.37b). This bound also includes the bound for $D_{q_1} > 0$. □

Remark 4. The use of the worst-case stability approximation $\cos(x_c(t) + \alpha) = -1$ yields a very conservative range of values κ, γ, and α. It implies that the trivial fixed point of the variational equations (2.27a)-(2.27b) with time-varying coefficients is stable for any value of $x_c(t)$. In reality, this does not have to be the case as long as its overall stability over the period of the limit cycle $x_c(t)$ is preserved such that its Lyapunov exponents remain negative. As a result, the sufficient conditions (2.37a)-(2.37b) should be considered as a proof of concept, giving an analytical proof for the stability and feasibility of a breathing cluster in the network system (2.2) (see Fig. 2.3 for the comparison with the numerically assessed region of stability).

Statement 2 [Bistability conditions]. Combining the co-existence condition (2.18) of Statement 1 with the stability criteria of Theorems 1 and 2, yields sufficient conditions on the co-existence of two stable patterns of synchrony with constant and oscillating phase shifts between two clusters.

In the following, we provide a numerical example of these bistable regimes and hysteretic transitions between them in a small network (2.2).

2.5 Numerical example

As the emergence of stable clusters and chimeras is easier to demonstrate in large Kuramoto networks without [1, 78] and with inertia [73], where the dynamics is close to its mean-field approximation, we knowingly choose the harder case of a small network (2.2) with $N = 5$ and $M = 4$ as our numerical example. Along with $\kappa = M/N = 0.8$, we fix parameter $\gamma = 0.45$ and study the dynamics of clusters as a function of α and β.

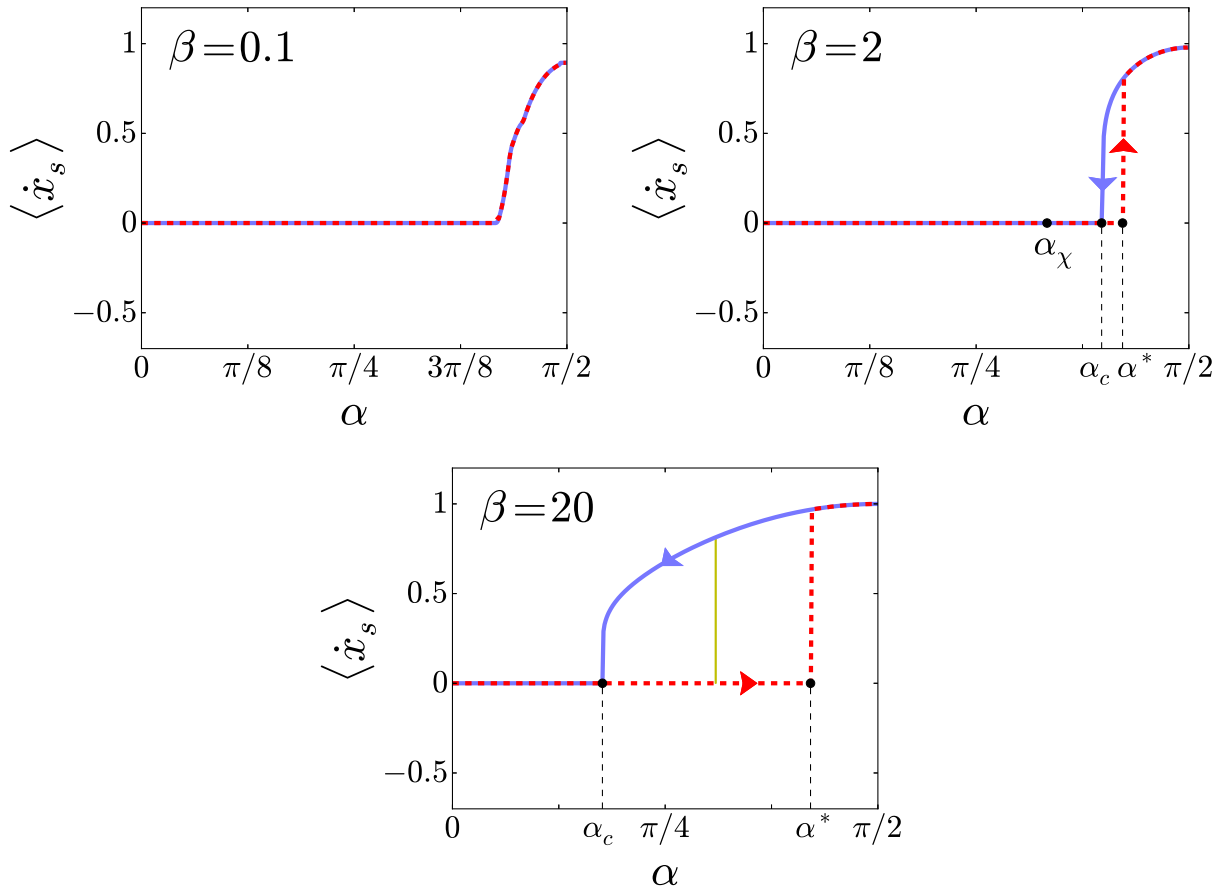

Figure 2.3: Hysteretic transitions as a function of α and β. The cluster with a constant shift is indicated by the zero derivative of phase shift $< \dot{x}_s >$. Non-zero averaged derivative $< \dot{x}_s >$ indicates the breathing cluster with an oscillating shift. The red dashed (blue solid) line corresponds to the direction of increasing (decreasing) α. $\beta = 0.1$: The clusters do not co-exist. $\beta = 2$: Clusters co-exist in the region (α_c, α^*). Point α_χ corresponds to the co-existence of the cluster with a constant shift and a stable chimera depicted in Fig. 2.5. $\beta = 20$: Increased inertia β enlarges the bistability region. The range $[\alpha_c = 0.5537, \alpha^* = 1.3273]$ matches the analytical condition of Statement 1. The thin vertical light stripe corresponds to the sufficient condition of Theorem 2.

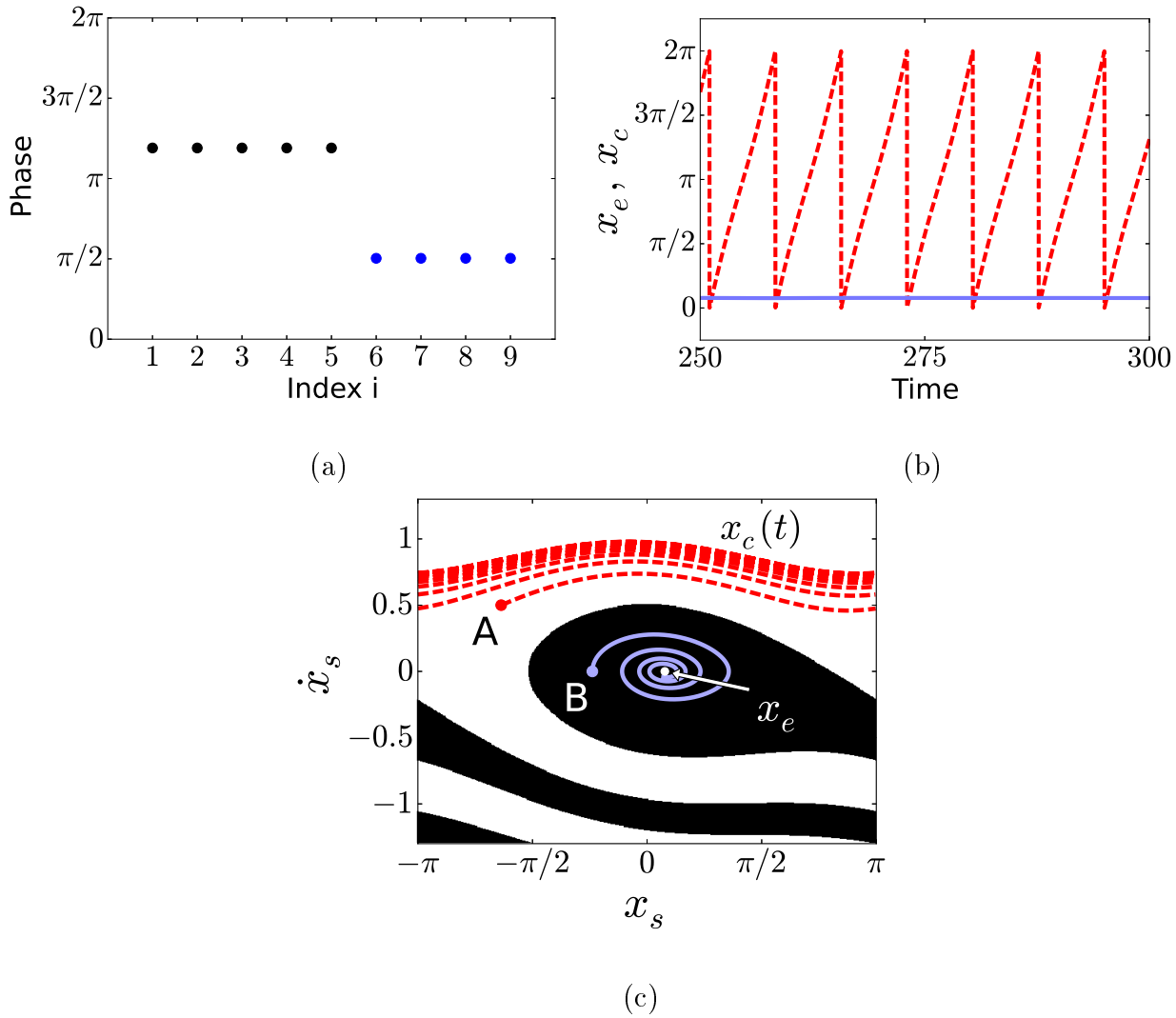

Figure 2.4: (a). Snapshot of the synchronized two-cluster pattern in the network (2.2) for $\alpha = \pi/3$ and $\beta = 20$. Initial conditions are chosen close to the cluster manifold and correspond to the breathing cluster pattern. (b). Corresponding time series of the co-existing phase shifts x_e and $x_c(t)$, robustly appearing from non-identical random initiation conditions, close to the cluster manifold. (c). Co-existence of the constant (x_e) and oscillating phase shifts ($x_c(t)$), determined by the fixed point (depicted in white) and the stable limit cycle (depicted in red), respectively. Initial conditions are chosen on the cluster manifold. Trajectories starting from initial conditions A and B converge to different attractors (the fixed point and limit cycle). Basins of attraction of the fixed point and the limit cycle are shown in black and white, respectively.

Figure 2.3 demonstrates how inertia β affects hysteretic transitions between the co-existing clusters. When inertia is small ($\beta = 0.1$), the network is mono-stable such that the breathing cluster emerges after the cluster with a constant shift disintegrates. Our simulations for $\beta = 2$ and $\beta = 20$ indicate that inertia promotes bistability and extends the range of α where the two clusters stably co-exist. Notice that the cluster with a constant shift loses its stability at α^* which corresponds to a saddle-node bifurcation of the fixed point in the pendulum equation (2.8a) (see Fig. 2.2). Therefore, this cluster is stable as long as it exists. When α decreases, the breathing cluster loses its stability at α_c which coincides with $\alpha_{\rm TR}$, where the limit cycle $x_c(t)$ merges into a homoclinic loop of the saddle and disappears with further decrease of α (cf. condition (2.18) in Statement 1). Therefore, similarly to the cluster with a constant shift, the breathing cluster remains stable as long as it is present. The values $\alpha_c = 1.3312$ for $\beta = 2$ and $\alpha_c = 0.5537$ for $\beta = 20$ match the values of the analytical bound (2.18) of Theorem 1 remarkably well. As a result, the co-existence range of α, predicted in Statement 1, coincides with the actual bistability range, observed in Fig. 2.3.

We have also verified the sufficient conditions of Theorem 2 in the worst case of large inertia ($\beta = 20$). The sufficient conditions (2.37a)-(2.37b) for the stability of the breathing cluster yield a narrow region $0.9700 < \alpha < 0.9733$ which is depicted by the light thin stripe in Fig. 2.3. While being very conservative, this region lies inside the bistability region. In accordance with (2.37b), this region becomes less conservative and enlarges when β decreases.

Figure 2.4 gives a more detailed description of the co-existing stable clusters with a constant and periodically oscillating phase shifts for $\alpha = \pi/3$ and $\beta = 20$ (cf. point A in Fig. 2.2b). In Fig. 2.4(a), we present a snapshot of the established cluster pattern. The oscillators in the first five- and second four-oscillator groups synchronize within the two clusters, and there is always a phase shift between the two synchronized groups. Depending on the initial conditions, the network exhibits either the two-cluster pattern with a constant inter-cluster phase shift or a breathing two-cluster pattern where the phase shift oscillates. While the static snapshot of Fig. 2.4(a) does not allow for identifying the dynamics of the phase shift, it actually corresponds to the breathing cluster with the oscillating phase shift

x_c, (red waveform depicted in Fig. 2.4(b)). Figure 2.4(b) indicates the bistability of the two patterns of synchrony starting from random non-equal initial conditions close to the cluster solution. Figure 2.4(c) shows the co-existence of the two dynamics for the phase shifts, similar to the qualitative phase portrait of Fig. 2.1. To explicitly define the phase shift x between the clusters, in Fig. 2.4(c), we set all initial conditions for the oscillators in the first five-oscillator cluster to zero, and for the oscillators in the second four-oscillator cluster to the same set of values $x, \dot{x}$. Thus, the initial difference between the cluster variable determines the initial phase shift x. Note that different initial conditions (points A and B) induce different phase shifts.

Figure 2.5 shows that the breathing cluster can turn into a stable breathing chimera where the first cluster of N oscillators remains locally stable, while the second cluster of M oscillators loses its stability. This stable chimera co-exists with the cluster with a constant phase shift (see the corresponding point α_χ in Fig. 2.3). While we have consistently explored the range of bistability between the two clusters of synchrony both analytically and numerically, we have not performed an exhaustive search for stable chimeras in the bistability region $[\alpha_c, \alpha^*]$ (cf. Fig. 2.3). Finding conditions on the co-existence of both stable clusters and stable chimeras is a subject of future study.

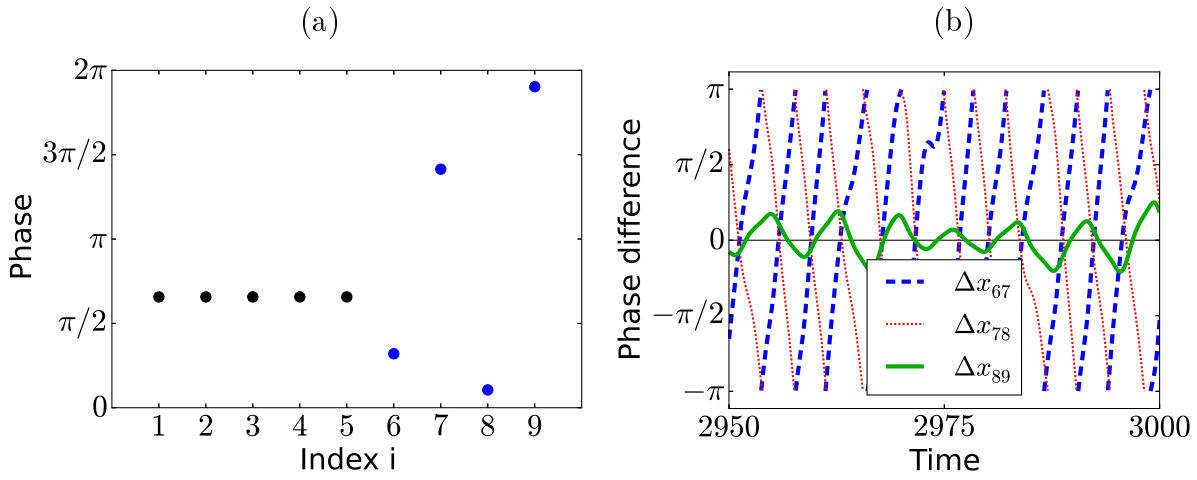

Figure 2.5: (a). Snapshot of a chimera state in the network (2.2) for $\alpha = \alpha_\chi = \pi/3$, $\beta = 2$. (b). Time-series of the phase differences between the oscillators in the second cluster. The oscillating phase differences indicate the absence of pairwise synchrony in the second cluster, therefore showing a stable chimera.

2.6 Conclusions

Rigorous analysis of the stability of cluster synchronization in complex networks of identical oscillators with symmetries has been shown to be challenging. It is typically limited to a restricted types of coupling and network topologies. This is due to the fact that the system, which determines the stability of a given multi-cluster decomposition, is high-dimensional, non-reducible, and often asymmetric. The Laplacian (diffusive) coupling with zero-row sum connectivity matrices seems to be the most difficult case for identifying cluster decompositions and proving their stability [16, 18, 83, 84, 8]. This is, in particular, due to complete synchronization, which is always present in unweighted, but possibly heterogeneous Laplacian networks, such that its stability often prevents the observation of co-existing stable clusters. In light of this, non-diffusive networks such as, for example, pulse-coupled neuronal networks[10, 12] where heterogeneous node degrees, defined by different numbers of inputs received by each cell, makes complete synchronization impossible [80]. This creates distinct groups of cells with equal node degree. The equal node degree constraint is a necessary

condition for cells to be in the same synchronous cluster. Together with the requirement of balanced coloring [46, 45, 106], this constraint determines the existence of clusters of perfect symmetry and allows for effectively identifying cluster decompositions, even in large complex networks, via the combinatorial algorithms [12, 57].

In this chapter, we have studied the stability of clusters in two coupled populations of identical Kuramoto oscillators with inertia. This network is essentially the two-population Kuramoto model[2, 1], proposed as a simple model of chimeras[2]. The new important modifications, which are vital for bistability of cluster patterns in our network, are (i) non-equal population sizes and (ii) the addition of inertia to the oscillator equation. Property (i) makes the existence of complete synchronization impossible such that a two-cluster pattern is the minimal cluster partition in this two-population network, although other multi-cluster partitions are also possible. Property (ii) increases the dimensionality of the intrinsic oscillator dynamics and creates a possibility for bistability of cluster patterns.

We have rigorously analyzed the dynamical properties and stability of the two-cluster pattern where the population splits into two synchronized groups, but there is always a phase shift between the groups. We have explicitly demonstrated that the dynamics of the phase shift can be bistable such that a constant phase shift co-exists with a time-varying shift which periodically changes from 0 to 2π. As a result, a two-cluster pattern with a constant shift co-exists with a breathing two-cluster pattern with an oscillating phase shift. We have derived the stability conditions for the stability of the cluster patterns. Due to the simple structure of the two-population network, the stability conditions for the variables, corresponding to the first and second populations, are independent. Therefore, the instability of synchrony within one group does not immediately imply the instability within the other group. In more rigorous terms, the cluster solution becomes a saddle such that stable transversal directions correspond to the first (larger) group of oscillators whereas unstable transversal directions correspond to the oscillators from the second (smaller) group. The stability result can be interpreted in terms of multidimensional clusters and chimeras. In large networks, high-dimensional stable manifolds of this saddle state may retain a close trajectory for a

considerable amount of time, giving rise to transient chimeras [77]. It can also lead to the emergence of stable multi-cluster states, where the oscillators in the smaller population split into subgroups. Our numerical simulations, not reported in this chapter, indicate these stable clusters, defined by high-dimensional cluster manifolds which are embedded into each other and contain the two-cluster manifold as a minimum cluster solution. Rigorous study of the transition from lower dimensional to high-dimensional cluster regimes, governed by the symmetry-induced embedding hierarchy [16] and accompanied by multistability of patterns of synchrony is a subject of future study.

In a more speculative way, the fulfilment of the transversal stability condition of the first cluster variables, while the transversal stability condition for the second cluster is violated, can be interpreted as a proof of a stable chimera. While the emergence of stable chimeras in the two-population network is confirmed by our numerical simulations, for this proof to be completely rigorous, one has to demonstrate the stability of the chimera solution in the longitudinal direction. This proof would require the analysis of the high-dimensional system that governs the dynamics of the chimera solution. In the case of the two-cluster solution, studied in this chapter, this system is two-dimensional and allows for a rigorous analysis of its solutions. Our results, concerning small networks of phase oscillators, also support the recent observation that a network does not have to be large to exhibit stable chimeras [78].

CHAPTER 3

WHEN THREE IS A CROWD: CHAOS FROM CLUSTERS OF KURAMOTO OSCILLATORS WITH INERTIA

3.1 Introduction

In Chapter 2, we derived analytical conditions for the emergence and co-existence of stable synchronized clusters in a two-population network of identical Kuramoto oscillators with inertia. These populations have different sizes such that complete synchronization of all oscillators is impossible. Instead, the oscillators can synchronize within each population cluster while there is a phase shift between the dynamics of the two clusters. Due to the presence of the inertia which makes the oscillator dynamics two dimensional, this phase shift can oscillate, inducing a breathing cluster pattern which can stably co-exist with a cluster pattern with a constant phase shift. In this Chapter, we aim at cluster dynamics of a three-population Kuramoto network with inertia obtained by adding a third population to the above two-population network setting from [14]. The resultant network is a three-population network of oscillators capable of synchronizing within each population, thereby potentially forming three synchronized clusters.

We primarily focus on the inter-cluster phase dynamics which can exhibit various types of complex behavior and multistability. Through rigorous analysis and numerics, we demonstrate that the addition of the third population can induce multistable chaotic dynamics, including those in which the phase shift between the first and second populations oscillates chaotically with small amplitudes whereas the phase shift between the second and third populations makes large-amplitude chaotic excursions. This effect may remind the reader of the familiar expression about romantic relationships "two is company, three is a crowd." This conventional wisdom suggests how events may unfold when such a relationship becomes destabilized by the addition of a third party. Our three-population network can be

considered a phenomenological model for describing cluster formation in real-world oscillatory networks. Suitable real-world network dynamics that can be captured by our model include (i) a multi-community neural structure of the nematode C. *elegans* worm in which neurons within each community form clusters of synchronized electrical activity that control locomotory rhythmogenesis [110, 52] and (ii) animal grouping when schooling fish align their swimming directions to split into cooperative clusters of synchronized movements to improve foraging success [37].

The layout of this Chapter is as follows. First, in Sec. 3.2, we present the oscillator network model and state the problem under consideration. In Sec. 3.3, we study limit sets and bifurcations in a four-dimensional (4D) system of two coupled pendulum equations which determines the existence of possible intercluster dynamics in the three-population network. We develop an auxiliary system method to derive bounds on partitions of parameters with permissible dynamics which include combinations of co-existing constant, periodic, and chaotically oscillating and rotating pairwise phase shifts. In particular, we prove the existence of a homoclinic orbit of a saddle-focus fixed point in the 4D system which satisfies the Shilnikov criterion [91] and yields spiral chaos. In Sec. 3.4, we analyze the variational equations for the stability of the three-cluster pattern as well as of its embedded two-cluster regime where the first and third populations become synchronized between each other, making their phase shift zero. As in the two-population case [14], we derive necessary and sufficient conditions for the constant phase shifts and give bounds on the stability of the cluster patterns with chaotically oscillating and rotating phase shifts. We also discuss the implications of our stability results to the stability of chimeras. Our analytical study is supported by numerical examples which indicate that the three-cluster pattern with chaotic phase shifts may have a fairly large attraction basin and co-exist with chimeras and hybrid solitary/chimera states. Section 3.5 contains concluding remarks and discussion.

The results presented in this Chapter were published in [30, 31].

3.2 Network model

We consider a three-population network of 2D rotators depicted in Fig. 3.1 and modeled by the following system

$$
\begin{aligned}
m\ddot{\theta}_i + \dot{\theta}_i &= \omega_0 + \tfrac{1}{M+2N}\left[\mu \sum_{j=1}^{N} \sin(\theta_j - \theta_i - \alpha) + \right. \\
&\qquad \left. + \nu \sum_{j=1}^{M} \sin(\phi_j - \theta_i - \alpha)\right], \\
m\ddot{\phi}_k + \dot{\phi}_k &= \omega_0 + \tfrac{1}{M+2N}\left[\nu \sum_{j=1}^{N} \sin(\theta_j - \phi_k - \alpha) + \right. \\
&\quad \left. + \mu \sum_{j=1}^{M} \sin(\phi_j - \phi_k - \alpha) + \nu \sum_{j=1}^{N} \sin(\psi_j - \phi_k - \alpha)\right], \\
m\ddot{\psi}_l + \dot{\psi}_l &= \omega_0 + \tfrac{1}{M+2N}\left[\nu \sum_{j=1}^{M} \sin(\phi_j - \psi_l - \alpha) + \right. \\
&\qquad \left. + \mu \sum_{j=1}^{N} \sin(\psi_j - \psi_l - \alpha)\right],
\end{aligned}
\tag{3.1}
$$

where $i = 1, \ldots, N$, $k = 1, \ldots, M$, and $l = 1, \ldots, N$. The network is composed of three oscillator populations of sizes N, M, and N. Variables θ_i, ϕ_k, and ψ_l correspond to the phases of 2D oscillators from the first, second, and third populations, respectively. The undirected connections within each population are all-to-all with a uniform intragroup coupling μ. The oscillators from the second (middle) group of size M are all-to-all connected to the oscillators from the first and third groups via a uniform intergroup coupling ν. To isolate the effect of adding an extra population to a two-population network, we do not directly couple the first and third groups thereby introducing a non-global structure to the network (3.1). The oscillators are chosen to be identical, with frequency ω_0, phase lag $\alpha \in [0, \pi/2)$ and inertia m. The model (3.1) is obtained from the Abrams *et al.* chimera model [2, 1], consisting of two groups of 1D phase oscillators with Kuramoto-Sakaguchi coupling [3], by increasing the dimension of the phase oscillators, adding the third group and making the group sizes uneven. The latter property does not allow the network to exhibit complete synchronization, which otherwise could have been the most dominant stable pattern. As a result, the uneven

group sizes can promote the emergence of stable clusters.

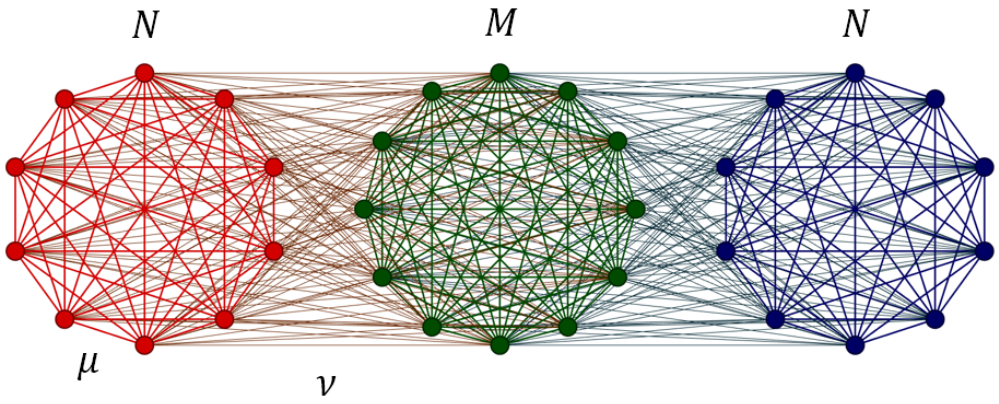

Figure 3.1: Three-population network of $M + 2N$ oscillators (3.1). Oscillators within each group are all-to-all connected to each other through uniform coupling μ. All oscillators in the second group of size M are connected to all oscillators in the first and third groups of sizes N through uniform coupling ν. There are no direct connections between the first and third groups.

Introducing new variables $\tau = \mu t/(M + 2N)$ and $\beta = \mu m/(M + 2N)$ along with a rotating frame of reference $\Theta_i = \theta_i - \omega_0 t + c$, $\Phi_k = \phi_k - \omega_0 t + c$, and $\Psi_l = \psi_l - \omega_0 t + c$, where c is a constant, we can rewrite the system (3.1) in a more convenient form

$$\begin{aligned}
\beta\ddot{\Theta}_i + \dot{\Theta}_i &= \sum_{j=1}^{N} \sin(\Theta_j - \Theta_i - \alpha) + \\
&\qquad + \gamma \sum_{j=1}^{M} \sin(\Phi_j - \Theta_i - \alpha), \\
\beta\ddot{\Phi}_k + \dot{\Phi}_k &= \gamma \sum_{j=1}^{N} \sin(\Theta_j - \Phi_k - \alpha) + \\
&\quad + \sum_{j=1}^{M} \sin(\Phi_j - \Phi_k - \alpha) + \gamma \sum_{j=1}^{N} \sin(\Psi_j - \Phi_k - \alpha), \\
\beta\ddot{\Psi}_l + \dot{\Psi}_l &= \gamma \sum_{j=1}^{M} \sin(\Phi_j - \Psi_l - \alpha) + \\
&\qquad + \sum_{j=1}^{N} \sin(\Psi_j - \Psi_l - \alpha),
\end{aligned} \tag{3.2}$$

where $\gamma = \nu/\mu$ represents the ratio between the intra- and intergroup couplings. Without loss of generality, we assume that the intragroup coupling μ is stronger than the intergroup

coupling ν so that $\gamma \in (0, 1)$.

While the network (3.2) may exhibit various clusters of perfect synchrony induced by additional symmetries of the network connectivity, we will mainly focus on the dynamics and stability of three-group cluster $C_{\Theta\Phi\Psi}$ where the oscillators are synchronized within the three groups. The existence of this cluster is defined by the invariant manifold (hyperplane)

$$\begin{aligned} C_{\Theta\Phi\Psi} = \{&\Theta_1 = \cdots = \Theta_N = \Theta, && \dot{\Theta}_1 = \cdots = \dot{\Theta}_N = \dot{\Theta}, \\ &\Phi_1 = \cdots = \Phi_M = \Phi, && \dot{\Phi}_1 = \cdots = \dot{\Phi}_M = \dot{\Phi}, \\ &\Psi_1 = \cdots = \Psi_N = \Psi, && \dot{\Psi}_1 = \cdots = \dot{\Psi}_N = \dot{\Psi}\}. \end{aligned} \tag{3.3}$$

Hereafter, we will be referring to $C_{\Theta\Phi\Psi}$ as a "manifold" or a "solution" interchangeably, depending on what term is more suitable in a particular context.

Notice that the equal node degree is a necessary condition for oscillators to form a synchronous cluster. Therefore, the oscillators from the second group of size M may not be synchronized with the oscillators from the first and third groups of size N, whereas the latter can form a cluster. As a result, the three-group cluster manifold $C_{\Theta\Phi\Psi}$ has an embedded invariant two-cluster manifold

$$\begin{aligned} C_{\Theta\Phi\Theta} = \{&\Theta_1 = \cdots = \Theta_N = \Theta, && \dot{\Theta}_1 = \cdots = \dot{\Theta}_N = \dot{\Theta}, \\ &\Phi_1 = \cdots = \Phi_M = \Phi, && \dot{\Phi}_1 = \cdots = \dot{\Phi}_M = \dot{\Phi}, \\ &\Psi_1 = \cdots = \Psi_N = \Theta, && \dot{\Psi}_1 = \cdots = \dot{\Psi}_N = \dot{\Theta}\} \end{aligned} \tag{3.4}$$

which represents the largest possible cluster partition of the network (3.2) with one synchronous cluster composed of all oscillators from the first and third groups and the other formed by all oscillators from the second group.

In the following, we will analyze the dynamics and stability of synchronous clusters $C_{\Theta\Phi\Psi}$ and $C_{\Theta\Phi\Theta}$ and reveal the role of the intrinsic oscillator parameters, coupling strength and network sizes in controlling the onset of each of the two cluster regimes.

3.3 Possible intercluster dynamics

We first study the existence of possible temporal dynamics on the three-cluster manifold $C_{\Theta\Phi\Psi}$. These dynamics are described by the following system obtained from system (3.2) by removing the indexes i, j, k

$$\begin{aligned}
\beta\ddot{\Theta} + \dot{\Theta} &= \gamma M \sin(\Phi - \Theta - \alpha) - N \sin\alpha, \\
\beta\ddot{\Phi} + \dot{\Phi} &= \gamma N \left[\sin(\Theta - \Phi - \alpha) + \sin(\Psi - \Phi - \alpha)\right] - \\
&\quad - M \sin\alpha, \\
\beta\ddot{\Psi} + \dot{\Psi} &= \gamma M \sin(\Phi - \Psi - \alpha) - N \sin\alpha.
\end{aligned} \tag{3.5}$$

Introducing the differences between the phases $x = \Theta - \Phi$ and $z = \Psi - \Phi$, we obtain the equations that govern the dynamics of the phase differences between the clusters

$$\begin{aligned}
\beta\ddot{x} + \dot{x} &= (M - N)\sin\alpha - \gamma[N \sin(x - \alpha) + \\
&\quad M \sin(x + \alpha) + N \sin(z - \alpha)], \\
\beta\ddot{z} + \dot{z} &= (M - N)\sin\alpha - \gamma[N \sin(x - \alpha) + \\
&\quad M \sin(z + \alpha) + N \sin(z - \alpha)].
\end{aligned} \tag{3.6}$$

3.3.1 Transformation to coupled pendulum equations

Similarly to [14], we set $\Omega = (M - N)\sin\alpha$, $R = \gamma\sqrt{N^2 + M^2 + 2MN\cos 2\alpha}$, and $\delta_0 = \arctan\left(\frac{M-N}{M+N}\tan\alpha\right)$ and use trigonometric formulas to turn the system (3.6) into

$$\begin{aligned}
\beta\ddot{x} + \dot{x} &= \Omega - R\sin(x + \delta_0) - \gamma N \sin(z - \alpha), \\
\beta\ddot{z} + \dot{z} &= \Omega - R\sin(z + \delta_0) - \gamma N \sin(x - \alpha).
\end{aligned} \tag{3.7}$$

Shifting the variables $(x, z) \to (x + \delta_0, z + \delta_0)$, setting $\delta = \alpha + \delta_0$, and rescaling time $\tau = t\sqrt{\frac{\beta}{R}}$, we obtain

$$\begin{aligned}
\ddot{x} + h\dot{x} + \sin x &= \omega - a\sin(z - \delta), \\
\ddot{z} + h\dot{z} + \sin z &= \omega - a\sin(x - \delta),
\end{aligned} \tag{3.8}$$

where $h = \frac{1}{\sqrt{\beta R}}$, $\omega = \frac{\Omega}{R}$, $a = \frac{\gamma N}{R}$, $\dot{x} = \frac{dx}{d\tau}$, and $\dot{z} = \frac{dz}{d\tau}$. Observe that (3.8) is a four-dimensional (4D) system of two coupled pendulums and therefore can exhibit complex dynamics. In some sense, each pendulum equation of (3.8) may also be viewed as a periodically driven nonlinear pendulum which is notorious for its chaotic behavior [22].

3.3.2 Fixed points

Depending on the parameters, the 4D system (3.8) may have up to four fixed points such that each point (x^*, z^*) corresponds to a constant phase shift x^* (z^*) between the first (third) and second clusters. In the following, we will show that two out of the four fixed points may be saddle-foci with a positive saddle value which can undergo a homoclinic bifurcation and induce Shilnikov-type chaotic intercluster dynamics.

System (3.8) is symmetric in x and z and has an invariant manifold $x = z$ which corresponds to the cluster manifold $C_{\Theta\Phi\Theta}$. The dynamics on the manifold $C_{\Theta\Phi\Theta} : \{x = z\}$ is described by the system

$$\ddot{x} + h\dot{x} + \sin x + a\sin(x - \delta) = \omega$$

which can be further reduced to a pendulum equation by combining the sine terms and using a trigonometric identity so that

$$\ddot{x} + h\dot{x} + a_1 \sin(x - \delta_1) = \omega, \tag{3.9}$$

where $a_1 = \sqrt{1 + a^2 + 2a\cos\delta}$ and $\delta_1 = \arctan\frac{a\sin\delta}{1+a\cos\delta}$.

Therefore, for $\omega < a_1$, the system (3.8) has two fixed points

$$\begin{aligned} &O_1(x_s = z_s = \arcsin\tfrac{\omega}{a_1} + \delta_1), \\ &O_2(x_u = z_u = \pi - \arcsin\tfrac{\omega}{a_1} + \delta_1) \end{aligned} \tag{3.10}$$

which belong to $C_{\Theta\Phi\Theta}$. The type and stability of these fixed points along the cluster manifold $C_{\Theta\Phi\Theta}$ is defined through (3.9) whose dynamics are similar to the classical pendulum equation with a constant torque ω [5]. Therefore, O_1 (O_2) is a stable (saddle) fixed point

with respect to the dynamics restricted to $C_{\Theta\Phi\Theta}$. While the directions transversal to $C_{\Theta\Phi\Theta}$ may be unstable, depending on the parameters of system (3.8), the fixed point O_1 (O_2) may become a saddle node (a saddle). As in the classical pendulum equation [5], these fixed points disappear via a saddle-node bifurcation in system (3.9) at $\omega = a_1$.

System (3.8) also has two other fixed points that belong to the three-cluster manifold $C_{\Theta\Phi\Psi}$ but lie outside the manifold $C_{\Theta\Phi\Theta}$ so that $x \neq z$. These fixed points $O_3(x_3, z_3)$ and $O_4(x_4, z_4)$ have the coordinates

$$\begin{aligned} x_{3,4} &= \arctan\left(\tfrac{1-a\cos\delta}{a\sin\delta}\right) \pm \arccos\left(\tfrac{\omega\sqrt{1+a^2-2a\cos\delta}}{1-a^2}\right), \\ z_{3,4} &= \arctan\left(\tfrac{1-a\cos\delta}{a\sin\delta}\right) \mp \arccos\left(\tfrac{\omega\sqrt{1+a^2-2a\cos\delta}}{1-a^2}\right). \end{aligned} \tag{3.11}$$

The detailed calculations of coordinates $x_{3,4}$ and $z_{3,4}$ is as follows. To find the coordinates of O_3 and O_4 in 4D system (3.8), we need to analyze the following system

$$\begin{aligned} \sin x + a\sin(z-\delta) &= \omega, \\ a\sin(x-\delta) + \sin z &= \omega. \end{aligned} \tag{3.12}$$

However, this analysis is not straightforward as one has to deal with a system of two nonlinear equations. A way to solve the system (3.12) is to use its symmetry under the involution $(x, z) \to (z, x)$. This symmetry implies that O_3 and O_4 are symmetric relative to $z = x$ and lie on the line

$$z = \kappa - x, \tag{3.13}$$

where κ is a constant to be determined. Thus, the coordinates of O_3 and O_4 can be written in the form

$$x_3 = z_4 = \kappa/2 + x_0, \quad x_4 = z_3 = \kappa/2 - x_0 \tag{3.14}$$

for some x_0. Substitution of (3.13) into (3.12) gives

$$\sin x + a\sin(-x + \kappa - \delta) = \omega. \tag{3.15}$$

Our goal is to find κ and x_0 in order to identify coordinates $x_3 = z_4$ and $x_4 = z_3$. the coordinates in (3.11). Using a trigonometric identity, we turn equation (3.15) into

$$C_1 \cos x + (1 - a\cos(\kappa - \delta)) \sin x = \omega, \tag{3.16}$$

where $C_1 = a\sin(\kappa - \delta)$. Using another trigonometric identity, we solve equation (3.16) for x to obtain

$$x_{3,4} = g \pm \arccos \frac{\omega}{C_2}, \quad \text{with} \tag{3.17}$$

$$C_2 = \sqrt{1 + a^2 - 2a\cos(\kappa - \delta)}, \tag{3.18}$$

$$g = \arctan\left(\frac{1 - a\cos(\kappa - \delta)}{C_1}\right). \tag{3.19}$$

From (3.14) and (3.17), we obtain $g = \kappa/2$ from which we calculate

$$\kappa/2 = \arctan\left(\frac{1 - a\cos\delta}{a\sin\delta}\right) \tag{3.20}$$

and then

$$\cos(\kappa - \delta) = \frac{2a - (a^2 + 1)\cos\delta}{a^2 + 1 - 2a\cos\delta}. \tag{3.21}$$

Thus (3.18) yields

$$C_2 = \frac{1 - a^2}{\sqrt{1 + a^2 - 2a\cos\delta}} \tag{3.22}$$

so x_0 in (3.14) becomes

$$x_0 = \arccos\left(\frac{\omega\sqrt{1 + a^2 - 2a\cos\delta}}{1 - a^2}\right). \tag{3.23}$$

Substituting (3.20) and (3.23) into (3.14), we finally obtain the explicit expressions (3.11) for $x_3,\ z_3,\ x_4,\ z_4$.

The stability of fixed points $O_1,\ O_2,\ O_3,\ O_4$ of system (3.8) can be evaluated through

the characteristic equation

$$\begin{aligned}(s^2+hs+\cos x^*)(s^2+hs+\cos z^*)-\\ a^2\cos(x^*-\delta)\cos(z^*-\delta)=0,\end{aligned} \tag{3.24}$$

where x^* and z^* are the coordinates of the fixed point in question (see (3.10) and (3.11)). The derivation of general close-form solutions for the fourth-order polynomial equation (3.24) might require the use of symbolic computations or even be out of reach. Here, we take a different route towards placing explicit bounds on the parameters of system (3.8) which guarantee that points O_3 and O_4 are saddle-foci with a positive saddle value. To do so, we set

$$\lambda = s^2+hs \tag{3.25}$$

to turn (3.24) into the biquadratic equation

$$\begin{aligned}\lambda^2+(\cos x^*+\cos z^*)\lambda+\cos x^*\cos z^*\\ -a^2\cos(x^*-\delta)\cos(z^*-\delta)=0.\end{aligned} \tag{3.26}$$

Its roots are

$$\begin{aligned}\lambda_{1,2}=\tfrac{1}{2}\big[-\cos x^*-\cos z^*\pm\\ \sqrt{(\cos x^*+\cos z^*)^2+4a^2\cos(x^*-\delta)\cos(z^*-\delta)}\big].\end{aligned} \tag{3.27}$$

Towards our goal of obtaining sufficient conditions that guarantee that points O_3 and O_4 are saddle-foci, we assume that the discriminant of (3.27) is positive. Note that this assumption can be realized by choosing appropriate values of γ and ω which can change x^* and z^* accordingly, while keeping δ intact. It follows from this assumption that $\lambda_1>0$ and $\lambda_2<0$. Thus, substituting constants (3.27) into (3.25), we obtain a quadratic equation whose solutions are

$$s_{11,12} = -\frac{h}{2} \pm \sqrt{\frac{h^2}{4} + \lambda_1}, \quad s_{21,22} = -\frac{h}{2} \pm i\sqrt{\left|\frac{h^2}{4} + \lambda_2\right|}, \tag{3.28}$$

where $s_{21,22}$ are complex when $|\lambda_2| > h^2/4$. Therefore, under these conditions, the fixed point O_3 (O_4) is a saddle focus with the 1D unstable manifold corresponding to the positive eigenvalue $s_{11} = -\frac{h}{2} + \sqrt{\frac{h^2}{4} + \lambda_1}$, and the 3D stable manifold composed of the 2D stable focus manifold which is determined by the complex eigenvalues $s_{21,22}$ and the 1D stable manifold defined by the negative eigenvalue s_{12}. These saddle-foci O_3 and O_4 have a positive saddle value [91] $\sigma = \mathrm{Re}(s_{21,22}) + s_{11} > 0$ if $\lambda_1 > \frac{3}{4}h^2$. Therefore, the saddle-foci O_3 and O_4 satisfy the Shinikov criterion for spiral chaos [91] which emerges as a result of a Shilnikov homoclinic bifurcation. In the following, we will derive sufficient conditions on the parameters of system (3.8) under which fixed points O_3 and O_4 can undergo homoclinic bifurcations leading to chaotic intercluster dynamics.

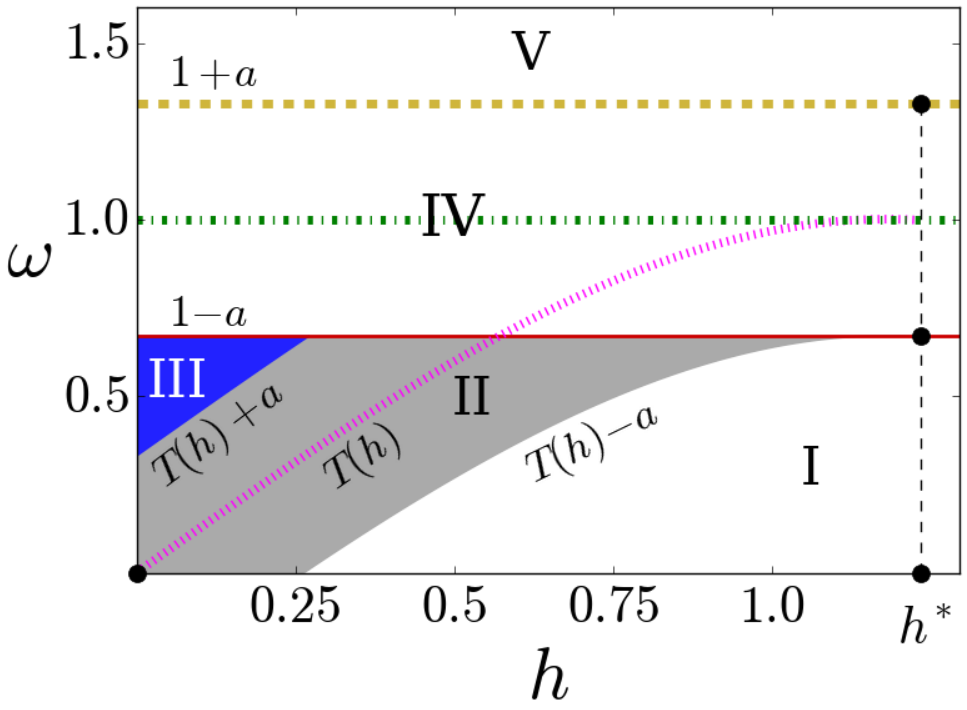

Figure 3.2: Existence diagram for possible phase shift dynamics in system (3.8) (an illustration of Statement 1). Region I ($\omega < T(h) - a$)): Only constant or oscillating phase shifts $x(t)$ and $z(t)$. Region II (light gray): Possible co-existence of constant, oscillating, rotating, and mixed-mode phase shifts. Homoclinic bifurcations of fixed points O_3 and O_4 take place only in this region. Region III (blue): the co-existence of the phase shifts of all three types is guaranteed. Region IV ($1 - a < \omega < 1 + a$): Possible co-existence of oscillating, rotating, and phase shifts. Region V ($\omega > 1 + a$): Only rotating phase shifts are possible. $T(h)$ is the Tricomi homoclinic curve (3.30) of pendulum equation (3.29) (pink dashed line). Damping $h = \frac{1}{\sqrt{\beta R}}$, where $R = \gamma\sqrt{N^2 + M^2 + 2MN\cos 2\alpha}$. Fixed parameters are $M = 12$, $N = 5$, $\gamma = 0.4$, and $\alpha = \pi/6$.

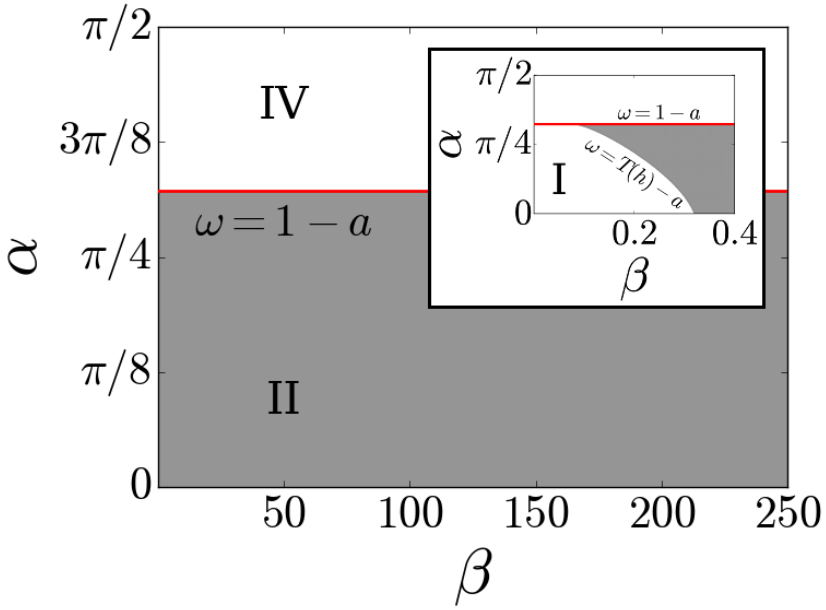

Figure 3.3: Existence diagram of Fig. 3.2 recast into the original parameters α and β of system (3.2) for $M = 25$, $N = 24$, and $\gamma = 0.4$. Only Regions I, II, and IV are present. The red line corresponds to the curve $\omega = 1 - a$ in Fig. 3.2. The inset shows the region of small values of β where Region I exists.

3.3.3 Oscillatory, rotatory and mixed-mode phase shifts

In addition to the fixed points which, when stable, induce constant intercluster phase shifts x and z, system (3.8) may have three main types of non-trivial, possibly chaotic, dynamics such as

1. oscillatory trajectories which do not rotate around the cylinder projection $(x, \dot{x})$ or $(z, \dot{z})$ and are centered around the fixed point O_1.

2. rotatory trajectories that encircle the cylinder projection $(x, \dot{x})$ or $(z, \dot{z})$, similarly to the limit cycle of a rotatory type in the classical pendulum equation (3.29).

3. mixed-mode trajectories that make several oscillatory turns while traveling around the cylinder.

Note that this classification distinguishes between the motions along the $(x, \dot{x})$ and $(z, \dot{z})$ projections so each phase shift x or z may individually exhibit oscillatory, rotatory, or mixed-mode dynamics. As a result, the relative evolution of x and z may be a combination of the three dynamics, yielding oscillating/oscillating, oscillating/rotating, rotating/rotating, mixed-mode/oscillating, or mixed-mode/rotating phase shifts. In this classification, the term oscillating/rotating refers to the case where the phase shift x oscillates around the fixed point with a small amplitude, whereas the phase shift z rotates from 0 to 2π around the cylinder. This classification can also be extended to incorporate the co-existence of constant and time-varying shifts. While a complete analytical study of possible dynamics of 4D system (3.8) is complicated and maybe out of reach, we adapt the auxiliary system method [19] to derive bounds that single out regions of parameters with possible homoclinic bifurcations of the fixed points and oscillatory, rotatory and mixed-mode phase shifts.

Statement 1 [sufficient conditions]. *Consider the partition of the (h, ω) parameter space of system* (3.8) *shown in Fig. 3.2. Let $T(h)$ denote the Tricomi homoclinic curve [104] of the pendulum equation*

$$\ddot{x} + h\dot{x} + \sin x = \omega \tag{3.29}$$

which can be approximated as in [14] by:

$$\omega = T(h) \approx \begin{cases} \frac{4}{\pi}h - 0.305h^3 & \text{for} \quad 0 < h < h^* \approx 1.22 \\ 1 & \text{for} \quad h > h^*. \end{cases} \tag{3.30}$$

Then five regions of the parameter partition correspond to the following dynamics of system (3.8).

1. *Region I: $\omega < T(h) - a$. Only oscillatory trajectories that do not encircle the cylinder projections $(x, \dot{x})$ and $(z, \dot{z})$ are permissible.*

2. *Region II: $\{\omega < 1-a\} \bigcap \{\omega < T(h)+a\} \bigcap \{\omega > T(h)-a\}$. Fixed points O_3 and O_4 of system* (3.8) *undergo homoclinic bifurcations only in this region. Oscillatory, rotatory*

and mixed-mode trajectories are possible.

3. *Region III:* $T(h) + a < \omega < 1 - a$. *The co-existence of oscillatory and rotatory trajectories is guaranteed. Mixed-mode oscillations are impossible.*

4. *Region IV:* $1 - a < \omega < 1 + a$. *Trajectories of all three types are possible, with the prevalence of rotatory and mixed-mode phase shift trajectories.*

5. *Region V:* $\omega > 1 + a$. *Only rotatory trajectories that encircle the cylinder projections* $(x, \dot{x})$ *and* $(z, \dot{z})$ *are possible.*

Proof. Adapting the auxiliary system method [19], we introduce two 2D auxiliary systems $A_x^{\pm}$ obtained from the x equation of system (3.8) by replacing $\sin(z - \delta)$ with ∓ 1 :

$$\begin{aligned} A_x^+ : &\quad \ddot{x} + h\dot{x} + \sin x = \omega + a \\ A_x^- : &\quad \ddot{x} + h\dot{x} + \sin x = \omega - a. \end{aligned} \tag{3.31}$$

Similarly, we introduce the systems $A_z^{\pm}$:

$$\begin{aligned} A_z^+ : &\quad \ddot{z} + h\dot{z} + \sin z = \omega + a \\ A_z^- : &\quad \ddot{z} + h\dot{z} + \sin z = \omega - a. \end{aligned} \tag{3.32}$$

Our goal is to demonstrate that the trajectories of auxiliary systems (3.31) and (3.32) bound trajectories of system (3.8) and govern their flow thereby determining possible types of phase shift dynamics of $x(t)$ and $z(t)$ and predicting qualitative changes of the vector flow that are accompanied by homoclinic bifurcations. Our approach is based on the property that the vector flows of auxiliary systems (3.31) and (3.32) are transversal to any non-trivial trajectory of system (3.8) at each point on the cylinders $(x, \dot{x})$, $x \neq 0$ and $(z, \dot{z})$, $z \neq 0$. More specifically, the vertical component of vector fields $(x, \dot{x})$ and $(z, \dot{z})$ of systems A_x^+ and A_z^+ is larger than that of system (3.8), except for the points where $\sin(z - \delta) = -1$ and $\sin(x - \delta) = -1$ and systems (3.31) and (3.32) coincide with (3.8). As a result, the trajectories

of system (3.8) cross the trajectories of systems A_x^+ and A_z^+ in the downward direction. And vice versa, the trajectories of system (3.8) cross the trajectories of systems A_x^- and A_z^- in the upward direction (see Fig. 3.4). Therefore, these properties allow for controlling the flow of system (3.8) with the help of separatrices and limit cycles of systems $A_x^\pm$ and $A_z^\pm$. Recall that the 4D system (3.8) turns into two uncoupled 2D pendulum equations for x and z with $a = 0$. The dynamics of pendulum equation (3.29) in the parameter space (h, ω) is controlled by the so-called Tricomi curve, $T(h)$, (3.30) (see Fig. 3.2) which corresponds to a homoclinic bifurcation of a saddle fixed point for $h < h^*$ and a saddle-node bifurcation for $h > h^*$ [5] (see Fig. 3.2).

In terms of the bifurcation diagram (h, ω) of Fig. 3.2, the Tricomi homoclinic curve $T(h)$ (pink dashed line) and the saddle-node curve $\omega = 1$ (green dash-dotted line) separate the bifurcation diagram into three regions with distinct dynamics of 2D pendulum equation (3.8) with $a = 0$ for x or z. These dynamics are (i) a stable fixed point which co-exists with a saddle fixed point (region under the Tricomi curve $T(h)$); (ii) the co-existence of the stable fixed point and a limit cycle (region bounded by the Tricomi and saddle-node curves); and (iii) a globally stable limit cycle.

We adapt these baseline boundaries for auxiliary systems (3.31) and (3.32) with $a \neq 0$ to derive sufficient conditions on permissible dynamics of the 4D system (3.8) which in turn determines the existence of phase shift dynamics in the three-group network (3.2). The dynamics of auxilary systems A_x^+ and A_z^+ (A_x^- and A_z^-) are symmetric. Therefore, it is sufficient to characterize possible trajectories of systems A_x^+ and A_x^- in the $(x, \dot{x})$ projection which also yields the symmetrical trajectories in the $(z, \dot{z})$ projection. A combination of two (identical or different) dynamics in the $(x, \dot{x})$ and $(z, \dot{z})$ projections will represent the behavior of 4D system (3.8).

Notice that the presence of $+a$ $(-a)$ term in auxiliary system A_x^+ (A_x^-) shifts the bifurcation diagrams and yields the new Tricomi homoclinic curve $\omega = T(h) - a$ $(\omega = T(h) + a)$ and the saddle-node curve $\omega = 1 - a$ $(\omega = 1 + a)$ in system (3.31). These curves formally partition the bifurcation diagram of Fig. 3.2 into five regions which correspond to the fol-

lowing dynamics.

Region I: $\omega < T(h) - a$. In this region both auxiliary systems A_x^+ and A_x^- may only have trivial dynamics in the form of the stable fixed point co-existing with the saddle fixed point. Figure 3.4 shows the arrangement of typical trajectories of auxiliary systems A_x^+ (A_z^+) (red lines) and A_x^- (A_z^-) (blue lines). The auxiliary system A_x^+ has the stable fixed point $E_x^+(x = \arcsin(\omega + a))$ and the saddle $S_x^+(x = \pi - \arcsin(\omega + a))$ [not shown in Fig. 3.4]. Similarly, the auxiliary system A_x^- has the stable fixed point $E_x^-(x = \arcsin(\omega - a))$ and the saddle $S_x^-(x = \pi - \arcsin(\omega - a))$. As a result, the trajectories of the two auxiliary systems which approach the corresponding stable fixed points E_x^- and E_x^+ form a "river" which traps trajectories of system (3.8) in the $(x, \dot{x})$ projection of the 4D phase space. Therefore, these trajectories of system (3.8) eventually reach the stable trapping region g_x^s bounded in x by E_x^- and E_x^+ (the green disk in Fig. 3.4a (left)) and stay inside it. The dynamics of system (3.8) in the $(z, \dot{z})$ projection is identical so that there also exists the stable trapping region g_x^s (the green disk in Fig. 3.4a (right)). These two disks form a topological ball $g_x^s \times g_z^s$ in the 4D phase space of system (3.8) which contains the fixed point O_1 [not shown]. The dynamics inside the ball may be periodic or even chaotic; however, the trajectories confined inside the ball may not rotate around the cylinders $(x, \dot{x})$ and $(z, \dot{z})$ so that only oscillatory motions with small amplitudes in x and z are allowed. Similarly, the stable manifolds of saddles S_x^+ and S_x^- form a "river" which contains the saddle O_2 of (3.8) [not shown] and the $(x, \dot{x})$ projection of its stable manifold. However, due to the flow arrangement, other trajectories of (3.8) leave this "river" and the saddle "cell" g_x^{sd} formed by the stable and unstable manifolds of saddles S_x^+ and S_x^- (the pink diamond-shaped region in Fig. 3.4a (left)) and approach the stable trapping zone. In the full 4D phase space of (3.8), the fixed point O_2 lies in a region represented by a topological product of saddle "cells" g_x^{sd} and g_z^{sd}. At the same time, the fixed point O_3 (O_4) of (3.8) lies in the region $g_x^{sd} \times g_z^s$ ($g_x^s \times g_z^{sd}$).

Region II: $H_1 : \{\omega < 1 - a\} \bigcap H_2 : \{\omega < T(h) + a\} \bigcap H_3 : \{\omega > T(h) - a\}$*) (the gray region in Fig. 3.2).* The lower border of Region II is determined by the part of the Tricomi curve $\omega = T(h) - a$ which corresponds to a homoclinic bifurcation of saddle E_x^- (E_z^-) in auxiliary

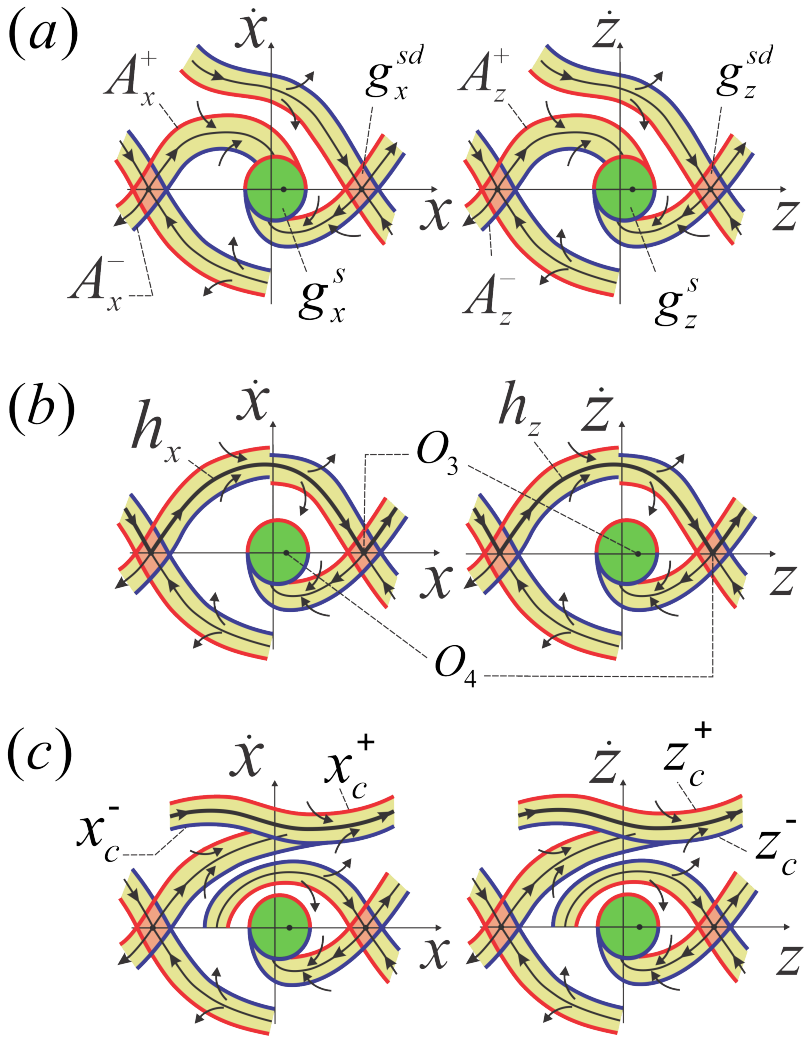

Figure 3.4: Schematic diagrams for $(x, \dot{x})$ and $(z, \dot{z})$ projections of vector flow (3.8), bounded by the trajectories of $2D$ auxiliary systems A_x^+ and A_z^+ (A_x^- and A_z^-) depicted in red (blue). (a). Typical arrangement of vector flow (3.8) corresponding to Region I (see Fig. 3.2). The unstable manifolds of the auxiliary systems' saddles form trapping regions ("rivers") that attract the trajectories of system (3.8) and guide them into trapping disks g_x^s and g_z^s (green). (b). Arrangement of vector flow (3.8) from Region II which allows the formation of the homoclinic orbit h_x (h_z) of saddle-focus O_3 (O_4). Note that the saddle-focus O_3 lies inside saddle cell g_x^{sd} (pink diamond-shaped region) in the $(x, \dot{x})$ projection and inside stable region g_z^s (green disk) in the $(z, \dot{z})$ projection representing its focus part. Saddle-focus point O_4 is symmetric to O_3, with its x (z) coordinate inside g_x^s (g_z^{sd}). (c). Region III. The auxiliary systems are bistable, each having a stable fixed point and a stable limit cycle. These limit cycles x_c^+ and x_c^- (z_c^+ and z_c^-) form a trapping "river" (the upper horizontal strip) which contains rotatory trajectories of (3.8). Trapping disks g_x^s and g_z^s (green) contain oscillatory trajectories of (3.8).

system A_x^- (A_z^-). In terms of Fig. 3.4a (left), this bifurcation occurs when the red curve emanating from the left saddle cell g_x^{sd} (the pink diamond-shaped region) would no longer go towards the green disk but rather merge with the red curve going into the right saddle cell to form a homoclinic orbit which connects the left and right saddle cells g_x^{sd} [not shown]. This homoclinic connection reroutes the vector flows so that the trajectories of system (3.8) can travel from the left to the right saddle cell. Entering the Region II, via, for example, increasing ω leads to the rearrangement of the "rivers" as shown in Fig. 3.4b where the unstable manifold of saddle-focus (or saddle) O_3 returns to O_3 and forms the homoclinic orbit h_x. Notice that due to the cyclic structure of the equations, the left and right saddle cells represent the same cell and contain the same fixed point O_3, so that the black curve connecting the fixed points in the two saddle cells is a homoclinic (not heteroclinic) orbit. The mutual arrangement of the "rivers" in the region $\dot{x} > 0$ allows the trajectories to either rotate around the cylinder as in the case of the homoclinic loop or reach the green disk to exhibit oscillatory dynamics. As the dynamics of systems A_z^+ and A_z^- are symmetric to those of systems A_x^+ and A_x^-, the overall dynamics of 4D system (3.8) is a combination of the trajectories depicted in the left and right diagrams of Fig. 3.4b. Therefore, all combinations of rotating, oscillating, and mixed-mode phases shifts are possible.

While this qualitative analysis does not allow for determining the exact values of parameters at which the homoclinic loop h_x is formed, it proves that system (3.8) has to undergo this homoclinic bifurcation in Region II where the "rivers" form a passage from one saddle cell to the other. This passage does not exist for the parameters from Region I (see Fig. 3.4a) and ceases to exist when the system reaches the border of Region III at which auxiliary systems A_x^+ and A_z^+ undergo a homoclinic bifurcation at $\omega = T(h) + a$ (see Fig. 3.2). In terms of Fig. 3.4b, this happens when the unstable and stable manifolds of saddle S_x^+ in system A_x^+ (the blue curves) merge together at the $x = 0$ coordinate axis for $\dot{x} > 0$ [not shown]. Therefore, the "rivers" formed by the stable and unstable manifolds of the saddle in auxiliary systems A_x^+ and A_x^- (A_z^+ and A_z^-) exchange their mutual arrangement when changing the parameters brings the system from Region I to Region III (cf. Fig. 3.4a and

Fig. 3.4c). Hence, there always exist bifurcation points in Region II at which the stable and unstable manifolds of O_3 (O_4), confined inside the "rivers," form the homoclinic loop h_x (h_z). Each of these bifurcation points lies on any path from Region I to Region III in parameter space (h, ω) which lies entirely inside Region II. Since the passage from one saddle cell to the other only exists in Region II, other multi-loop homoclinic bifurcations of O_3 and O_4 may also be only possible in Region II.

Region III: $T(h)+a < \omega < 1-a$ *(the blue region in Fig. 3.2).* Entering this region from Region II disconnects the "rivers" centered around the stable and unstable manifolds as shown in Fig. 3.4c. In Region III, each system A_x^- and A_x^+ is bistable and has a stable fixed point (inside the green disk) and a limit cycle of rotatory type, born as a result of the homoclinic bifurcations at $\omega = T(h)-a$ and $\omega = T(h)+a$, respectively. Therefore, the trajectories of $4D$ system (3.8) eventually reach and remain trapped either inside the green disk or inside the "river" formed by two stable limit cycles x_c^- and x_c^+ (the horizontal river in the upper part of Fig. 3.4c (left)). As a result, this arrangement guarantees (i) the bistability of oscillatory and rotatory trajectories which may be periodic or chaotic and (ii) the absence of mixed-mode oscillations since the trajectories cannot switch between the two trapping regions. Again, combining the dynamics of the left and right diagrams of Fig. 3.4c guarantees the existence of rotating/rotating, rotating/oscillating, oscillating/oscillating phase shift regimes in the network.

Region IV: $1-a < \omega < 1+a$. System A_x^+ only has a stable limit as the stable and saddle fixed points E_x^+ and S_x^+ had disappeared via a saddle-node bifurcation at $\omega = 1-a$. At the same time, system A_x^- has the same structure as in Region III. In terms of Fig. 3.4c, this amounts to the disappearance of all red curves [not shown], except for the upper border of the horizontal "river" representing the stable limit cycle x_c^+. As the trapping disk has partly disintegrated, the trajectories of the $4D$ system (3.8) may escape it and reach the trapping "river" with rotatory trajectories. Hence, all possible dynamics of phase shifts are possible, with the prevalence of rotatory trajectories.

Region V: $\omega > 1+a$. Similarly to system A_x^+ at the border between Region III and Region

IV, system A_x^- undergoes a saddle-node bifurcation at $\omega = 1 + a$. Thus, in Region V both systems A_x^- and A_x^+ only have globally stable limit cycles x_c^- and x_c^+ which form a unique trapping region ("river") for all the system's trajectories, yielding the existence of only rotatory trajectories in the system (3.8). □

Figure 3.3 relates these regions of parameters h and ω to the original parameters of network (3.2). Hereafter, we choose the phase lag α and inertia β as control parameters, and fix the group sizes $N = 24$ and $M = 25$ and the ratio between the intra- and inter group coupling $\gamma = 0.4$. We aim to show that even a minimal difference between the sizes of the first (third) group of N oscillators and the second group of M oscillators can yield phase shift chaos. In this case, the (h, ω) diagram of Fig. 3.2 typically does not contain Region III as the curve $\omega = T(h) + a$ is located above the line $\omega = 1 - a$. Recast in the parameters α and β, this diagram typically maximizes the size of Regions II and IV and minimizes Region I over a large range of inertia β (see Fig. 3.3).

The parameter partition of Fig. 3.2 characterizes the regions of parameters where different types of phase shifts are possible and where homoclinic bifurcations of O_3 and O_4 leading to the emergence of chaotic dynamics take place. More specifically, in Region I, the phase shifts $x(t)$ and $z(t)$ may only be constant or may periodically or chaotically oscillate with a small amplitude. Region II corresponds to the richest dynamics where all three types of time-varying phase shifts are possible thereby allowing for oscillatory, rotatory, and mixed-mode chaos. In this region, O_3 and O_4 undergo homoclinic bifurcations, yielding Shilnikov spiral chaos. While chaotic shift dynamics may be observed in the other regions of the parameter partition, this spiral chaos originates from Region II due to the homoclinic bifurcations and persists beyond this region. The dynamics in Region III are similar to those in Region II, except that the co-existence of oscillating, rotating, and mixed-mode phase shifts is guaranteed by Statement 1. Region IV represents a transition zone, where, similar to Regions II and III all three types of time-varying phase shifts may appear. However, the rotatory phase shifts become more frequent as ω increases toward $\omega = 1 + a$, finally entering into Region V

where only rotatory phase shifts are possible.

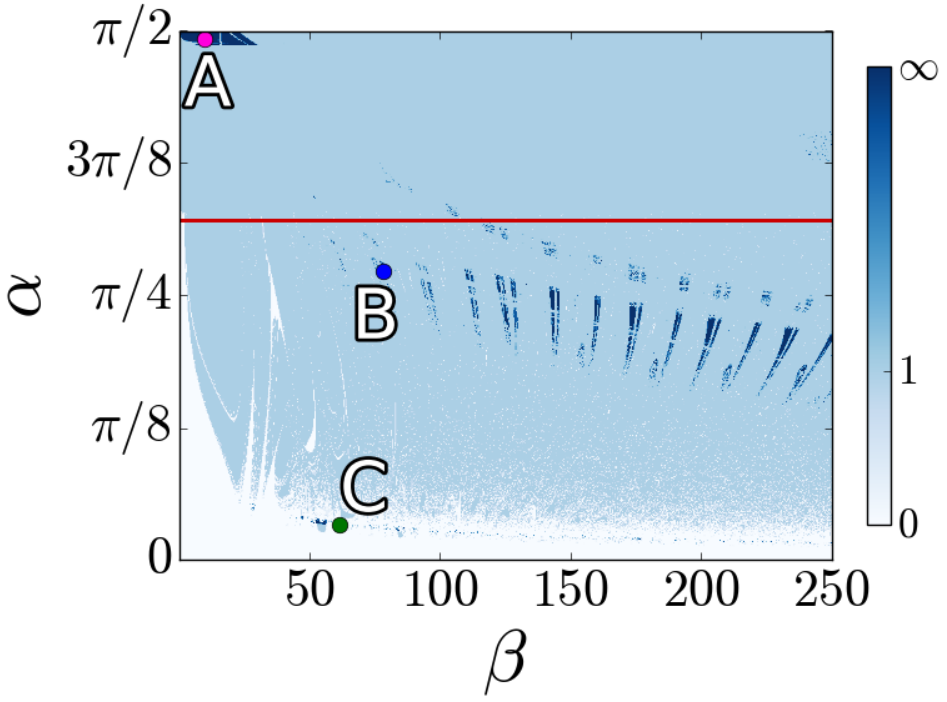

Figure 3.5: Regular and chaotic phase shift dynamics of system (3.8) evaluated numerically as a function of parameters α and β. The color-coding corresponds to the period of a limit cycle. White regions correspond to fixed points with a zero winding number; light blue regions correspond to a winding number of 1 (period-one limit cycles); dark blue regions correspond to chaotic orbits with infinitely large winding numbers. Sample points A with $(\beta, \alpha) = (10, 397\pi/800)$, B with $(\beta, \alpha) = (78.125, 437\pi/1600)$, and C with $(\beta, \alpha) = (61.5625, 27\pi/800)$ correspond to chaotic mixed-mode/mixed-mode, rotating/rotating, and oscillating/rotating phase shift regimes, respectively (see Figs. 3.6-3.8). The red horizontal line corresponds to the line $\omega = 1 - a$ in Fig. 3.3. The region under the red line is Region II, where homoclinic bifurcations give birth to chaos. Other parameters are as in Fig. 3.3.

To support our analytical analysis and prediction, we have numerically studied the dynamics of phase shifts in system (3.8) (see Fig. 3.5) and found regions of parameters which yield chaotic mixed-mode/mixed mode (sample point A, Fig. 3.6), rotating/rotating

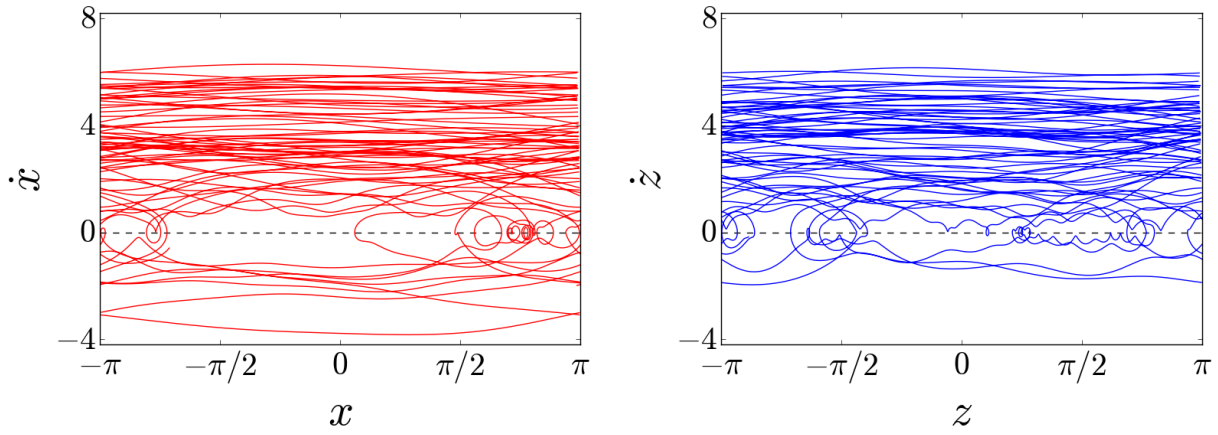

Figure 3.6: Mixed-mode/mixed-mode phase shift regime corresponding to point A in Fig. 3.5. Both x and z phase shifts are of mixed-mode type with the prevalence of chaotic rotatory motions. The values of x and z are projected onto a flattened cylinder where $x \to (x - \pi) \mod (2\pi) - \pi$ and $z \to (z - \pi) \mod (2\pi) - \pi$.

(sample point B, Fig. 3.7), and rotating/oscillating (sample point C, Fig. 3.8) phase shift regimes. As expected, a majority of the chaotic regions lie in Region II (cf. Fig. 3.5 and Fig. 3.3) where homoclinic bifurcations of fixed points O_3 and O_4 give birth to spiral chaos. A detailed analysis of these homoclinic bifurcations and transitions to chaos is beyond the scope of this Chapter and will be reported elsewhere. However, we have verified the eigenvalues of fixed points O_3 and O_4 at sample points A, B, and C. These eigenvalues are identical for both O_3 and O_4 due to the symmetries of (3.11) and (3.24). For the parameters corresponding to sample points B and C, the eigenvalues satisfy the assumption that $\lambda_1 > 0$ and $\lambda_2 < 0$ (cf. (3.27)), and therefore can be calculated analytically through (3.28). This yields the eigenvalues $s_{11} = 0.7499$, $s_{12} = -0.7815$, and $s_{21,22} = -0.0158 \pm 0.8609i$ (for sample point B) and $s_{11} = 0.9184$, $s_{21} = -0.9472$, and $s_{21,22} = -0.0144 \pm 0.9330i$ (for sample point C). Thus, fixed points O_3 and O_4 are saddle-foci with a positive saddle value σ and have 1D unstable and 3D stable manifolds. As a result, O_3 and O_4 satisfy the Shilnikov criterion [90] and offer a possible mechanism for the emergence of different forms of spiral chaos in system (3.8) and, ultimately, in the three-group network (3.2). In particular, Fig. 3.8 corresponding to sample point C demonstrates the existence of a representative spiral chaotic regime where

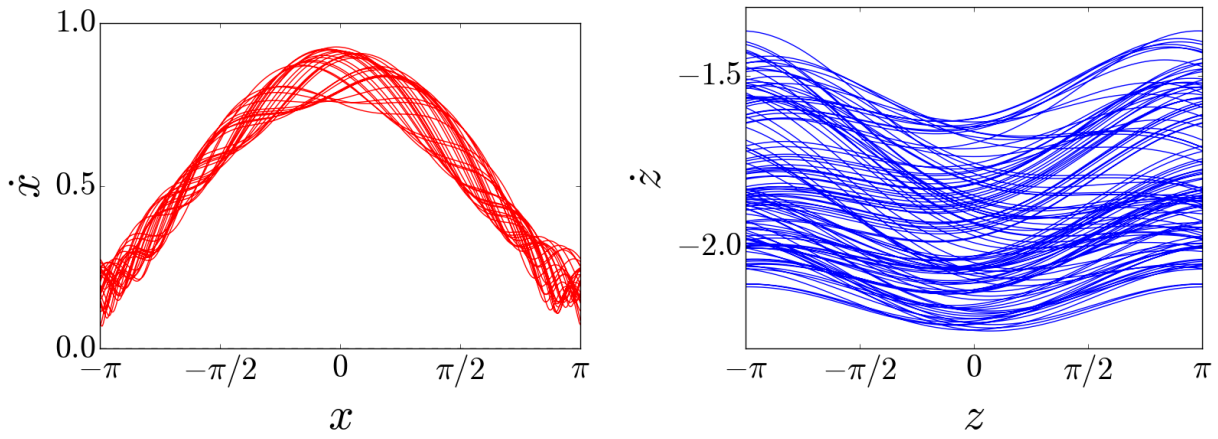

Figure 3.7: Rotating/rotating phase shift regime corresponding to point B in Fig. 3.5. Both x and z phase shifts chaotically rotate around the cylinder.

the phase shift $x(t)$ between the first and second groups of synchronized oscillators in network (3.2) rotates chaotically between $-\pi$ and π, whereas the phase shift $z(t)$ oscillates chaotically within a smaller range of $z(t) \in (-1.0, 1.0)$.

3.4 Stability analysis

Having studied the existence of possible phase shift regimes between the synchronized groups defined by the cluster manifold $C_{\Theta\Phi\Psi}$, we proceed with a stability analysis which indicates what phase shifts can stably emerge in the network.

3.4.1 Stability of three-cluster manifold $C_{\Theta\Phi\Psi}$

To determine the conditions under which the synchronous three-group cluster with constant, periodic, or chaotic shifts $x(t)$ and $z(t)$ can stably emerge in the network, we linearize system (3.2) about the synchronous cluster solution $C_{\Theta\Phi\Psi} : \{\Theta, \dot{\Theta}, \Phi, \dot{\Phi}, \Psi, \dot{\Psi}\}$.

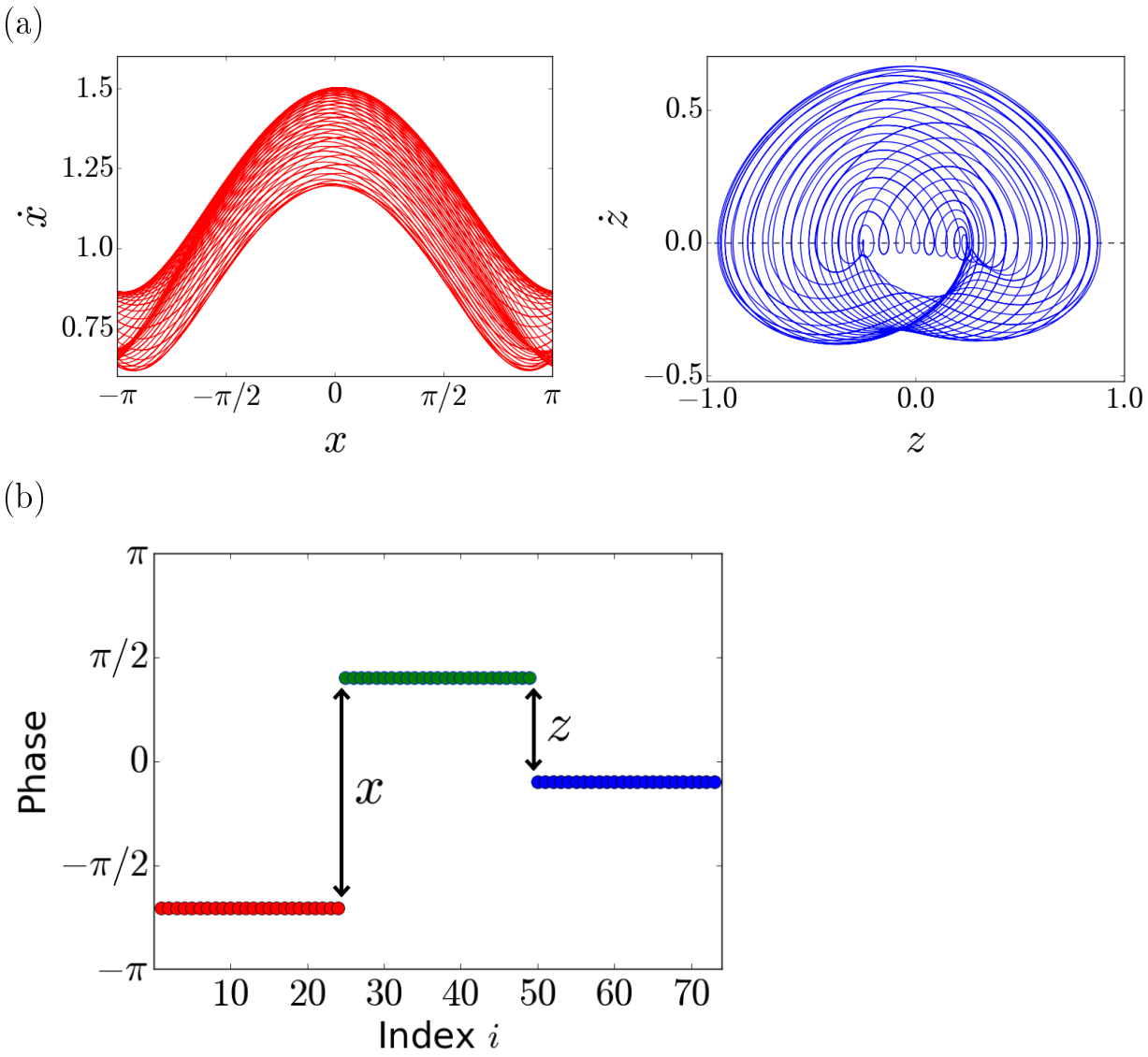

Figure 3.8: (a). Rotating/oscillating phase shift regime corresponding to point C in Fig. 3.5. The x and z phase shifts exhibit rotatory and oscillatory chaos, respectively. (b). Snapshot of the corresponding three-cluster pattern in network (3.2) of $M + 2N$ oscillators with $M = 25$ and $N = 24$. The initial states are chosen on the manifold $C_{\Theta\Phi\Psi}$ to form the corresponding three clusters where the colored dot indicates the instantaneous phase of oscillator with index i. The initial conditions for $x(t)$ and $z(t)$ are chosen randomly from $(0, 1)$. The rotating phase shift between the first (red dots) and second (green dots) clusters is governed by $x(t)$ and makes large chaotic excursions between $-\pi$ and π. The oscillating phase shift between the second (green dots) and third (blue dots) clusters is driven by $z(t)$ and therefore oscillates between -1 and 1.

This yields

$$\begin{aligned}
\beta\ddot{\xi}_i + \dot{\xi}_i &= -q_1 + \cos\alpha \sum_{j=1}^{N} \xi_j + \gamma\cos(x+\alpha) \sum_{j=1}^{M} \eta_j, \\
\beta\ddot{\eta}_k + \dot{\eta}_k &= -q_2\eta_k + \cos\alpha \sum_{j=1}^{M} \eta_j + \gamma\cos(x-\alpha) \sum_{j=1}^{N} \xi_j \\
&\quad + \gamma\cos(z-\alpha) \sum_{j=1}^{N} \xi_j, \\
\beta\ddot{\zeta}_l + \dot{\zeta}_l &= -q_3\zeta_\ell + \cos\alpha \sum_{j=1}^{N} \zeta_j + \gamma\cos(z+\alpha) \sum_{j=1}^{M} \eta_j,
\end{aligned} \tag{3.33}$$

where ξ_i, $i = 1, ..., N$, η_k, $k = 1, ..., M$, ζ_l, $l = 1, ..., N$ are infinitesimal perturbations of the i-th oscillator's synchronous solution Θ, Φ, Ψ, respectively, and

$$q_1 = N\cos\alpha + \gamma M\cos(x+\alpha), \tag{3.34a}$$

$$q_2 = M\cos\alpha + \gamma N[\cos(x-\alpha) + \cos(z-\alpha)], \tag{3.34b}$$

$$q_3 = N\cos\alpha + \gamma M\cos(z+\alpha). \tag{3.34c}$$

Hereafter, we go back to the original notations $x = \Theta - \Phi$ and $z = \Psi - \Phi$ which differ from the shifted variables x and z, used in system (3.8) and in the remainder of Sec. 3.3, by the constant δ_0. This abuse of notation simplifies the exposition as x and z always denote the phase shifts between the cluster groups. At the same time, the use of the original notations makes the stability analysis more manageable and leads to stability conditions which are easier to express in terms of the original parameters of network model (3.2).

In a similar manner to [14], we study the transversal stability of $C_{\Theta\Phi\Psi}$ by introducing the difference variables

$$\begin{aligned}
s_i &= \xi_i - \xi_{i+1}, \quad i = 1, \ldots, N-1, \\
u_k &= \eta_k - \eta_{k+1}, \quad k = 1, \ldots, M-1, \\
w_\ell &= \zeta_\ell - \zeta_{\ell+1}, \quad \ell = 1, \ldots, N-1
\end{aligned} \tag{3.35}$$

and subtracting the corresponding equations in (3.33) to obtain

$$\beta\ddot{s}_i + \dot{s}_i + q_1 s_i = 0,\ i = 1, ..., N, \tag{3.36a}$$

$$\beta\ddot{u}_k + \dot{u}_k + q_2 u_k = 0,\ k = 1, ..., M, \tag{3.36b}$$

$$\beta\ddot{w}_l + \dot{w}_l + q_3 w_l = 0,\ l = 1, ..., N. \tag{3.36c}$$

Here, the sum terms from (3.33) have collapsed into q_1, q_2, and q_3 due to the symmetry of the global intra and inter-cluster coupling, thereby decoupling the equations (3.36a)-(3.36c) and significantly simplifying their stability analysis.

The linearized equations (3.36a)-(3.36c) are governed by the phase shifts x and z through (3.7). Therefore, in the simple case where $x_e = x_s - \delta_0$ and $z_e = z_s - \delta_0$ are constant and determined by fixed point $O_1(x_s, z_s)$ when it exists and is stable, the analysis of (3.36a)-(3.36c) amounts to evaluating the signs of q_1, q_2, and q_3 at x_e, z_e. Hence, the stability of (3.36a)-(3.36c) is guaranteed iff

$$q_{1,2,3}|_{x_e,z_e} > 0. \tag{3.37}$$

This claim can be easily checked by looking at the characteristic equations $\beta p^2 + p + q_{1,2,3} = 0$ for the linear differential equations (3.36a)-(3.36c) with constant coefficients. Here, $q_{1,2,3}$ must be positive for the real parts of the characteristic equations to be negative.

The criterion (3.37) represents the necessary and sufficient condition for the stability of the synchronous cluster solution $C_{\Theta\Phi\Psi}$ with constant phase shifts x_e and z_e and can be easily applied as long as the fixed point O_1 exists for $\omega < a_1$.

In the more complex case where the phase shifts x_s and z_s are time-varying, the linear equations (3.36a)-(3.36c) contain time-dependent coefficients q_1, q_2, q_3. Therefore, the exact stability conditions of (3.36a)-(3.36c) can only be obtained numerically by calculating the Lyapunov exponents. However, we manage to analytically derive sufficient conditions which guarantee that the cluster solution $C_{\Theta\Phi\Psi}$ with even chaotic phase shifts $x(t)$ and $z(t)$ is locally stable. This leads to the following assertion.

Statement 2 [sufficient conditions]. *The cluster solution $C_{\Theta\Phi\Psi}$ with oscillating or rotating phase shifts $x(t)$ and $z(t)$ is locally stable in the transversal direction if*

$$\sqrt{2}\gamma < \cos\alpha < \min\left\{\frac{1-4\beta\gamma M}{4\beta N}, \frac{1-8\beta\gamma N}{4\beta M}\right\}. \tag{3.38}$$

Proof. Since the coefficients $q_1(t)$, $q_2(t)$, and $q_3(t)$ become time-dependent when the phase shifts $x(t)$ and $z(t)$ vary in time, the stability condition (3.37) for the variational equations (3.36a)-(3.36c) is no longer sufficient. To derive such a sufficient condition, we use the stability criterion [38] which guarantees that a linear second-order equation with a time-varying coefficient $q(t)$

$$\beta\ddot{v} + \dot{v} + q(t)v = 0 \tag{3.39}$$

is stable if

$$q(t) > 0, \tag{3.40a}$$

$$D(t) = 1 - 4\beta q(t) > 0 \text{ for } \forall t, \tag{3.40b}$$

where $D(t)$ is the discriminant of the characteristic equation $\beta p^2 + p + q(t) = 0$ with the frozen time t. In other words, this conservative criterion guarantees that the linear equation (3.39) with time-varying coefficient $q(t)$ is stable as long as the fixed point $v = 0$ is a stable node for any $t > 0$ and never becomes a stable focus or a degenerate node.

Applying the criterion (3.40a)-(3.40b) to the variational equations (3.34a)-(3.34c), we first verify the condition (3.40a) for $q_1(t)$, $q_2(t)$, and $q_3(t)$. To impose conservative conditions on $q_{1,2,3}$ to be positive, we consider the worst-case bounds which minimize $q_{1,2,3}$ in (3.34a)-(3.34c):

$$\begin{aligned} &\cos(x(t)+\alpha) = -1,\ \cos(x(t)-\alpha) = -1, \\ &\cos(z(t)-\alpha) = -1,\ \cos(z(t)+\alpha) = -1. \end{aligned} \tag{3.41}$$

This implies that

$$q_{1,3}(t) > 0 \text{ for } \forall t \text{ if } \cos\alpha > \gamma M/N, \tag{3.42a}$$

$$q_2(t) > 0 \text{ for } \forall t \text{ if } \cos\alpha > 2\gamma N/M. \tag{3.42b}$$

Solving the inequality in (3.42a) for N/M and then substituting $N/M = \gamma/\cos\alpha$ into (3.42b), we obtain the condition that guarantees that $q_{1,2,3} > 0$ for any t if

$$\cos\alpha > \sqrt{2}\gamma. \tag{3.43}$$

This bound yields the left-hand side part of inequality (3.38).

Finally, to verify the condition (3.40b) for discriminants $D_{1,2,3}(t)$ to be positive for (3.34a)-(3.34c), we consider the worst-case scenario bounds which maximize $q_{1,2,3}$. These are the conditions (3.41) with -1 replaced with $+1$. Thus, the condition (3.40b) is satisfied for (3.34a)-(3.34c) for any time $t > 0$ if

$$4\beta(N\cos\alpha + \gamma M) < 1,\ 4\beta(M\cos\alpha + 2\gamma N) < 1. \tag{3.44}$$

Solving (3.44) for $\cos\alpha$ and choosing the lowest on the two bounds yields the right-hand side part of the inequality (3.38). □

Remark 1. If the sizes of the cluster groups are such that $2N > M$ (as in the numerical examples of Figs 3.3-3.8), then the condition (3.38) becomes

$$\sqrt{2}\gamma < \cos\alpha < \frac{1 - 8\beta\gamma N}{4\beta M} \tag{3.45}$$

as this right-hand side bound is always the minimum of the two in (3.38).

Remark 2. The bound (3.38) is very conservative due to the use of the worst-case stability conditions. Therefore, it should be considered as a proof of concept that analytically demonstrates that the cluster solution $C_{\Theta\Phi\Psi}$ with time-varying, possibly chaotic phase shifts $x(t)$

and $z(t)$ can be stable. Moreover, this stability condition clearly reveals a destabilizing role of the inertia β in the stability of $C_{\Theta\Phi\Psi}$. Indeed, increasing β reduces the right-hand side of inequality (3.38) and therefore diminishes the range of α in which the cluster solution is stable, thereby eventually making the cluster solution unstable for higher β (see Fig. 3.9 for the actual stability regions revealed via numerical simulations and Fig. 3.10 for the comparison with the conservative bound (3.38)).

Figure 3.9 demonstrates stability diagrams for synchronization of the oscillators within each of the three groups, evaluated via the Kuramoto order parameter $r = \frac{1}{n}\sum_{j=1}^{n}\langle e^{i\varphi_j}\rangle$, calculated separately for the phases within the first ($\varphi_j = \Theta_j$, $j = 1, .., N$), second ($\varphi_j = \Phi_j$, $j = 1, .., M$), and third ($\varphi_j = \Psi_j$, $j = 1, .., N$) groups, where $\langle ...\rangle$ denotes a time average. Notice that the three-cluster solution $C_{\Theta\Phi\Psi}$ with the mixed-mode/mixed-mode chaotic shifts depicted in Fig. 3.6 and corresponding to point A in the existence (Fig. 3.5) and stability (Fig. 3.9) diagrams is unstable. This is in qualitative agreement with the sufficient condition of Statement 2 which predicts a general tendency of increased phase lag parameter $\alpha \in [0, \pi/2)$ to hinder the stability of the cluster solution via decreasing $\cos\alpha$ in (3.38). In fact, the point A is located in a region of α close to $\pi/2$, where $\cos\alpha$ is close to 0, thereby making the stability conditions (3.40a)-(3.40b) impossible to satisfy. At the same time, lower values of α yield the stability of the three-cluster solution with the rotating/rotating and rotating/oscillating chaotic phase shifts, corresponding to points B and C, respectively.

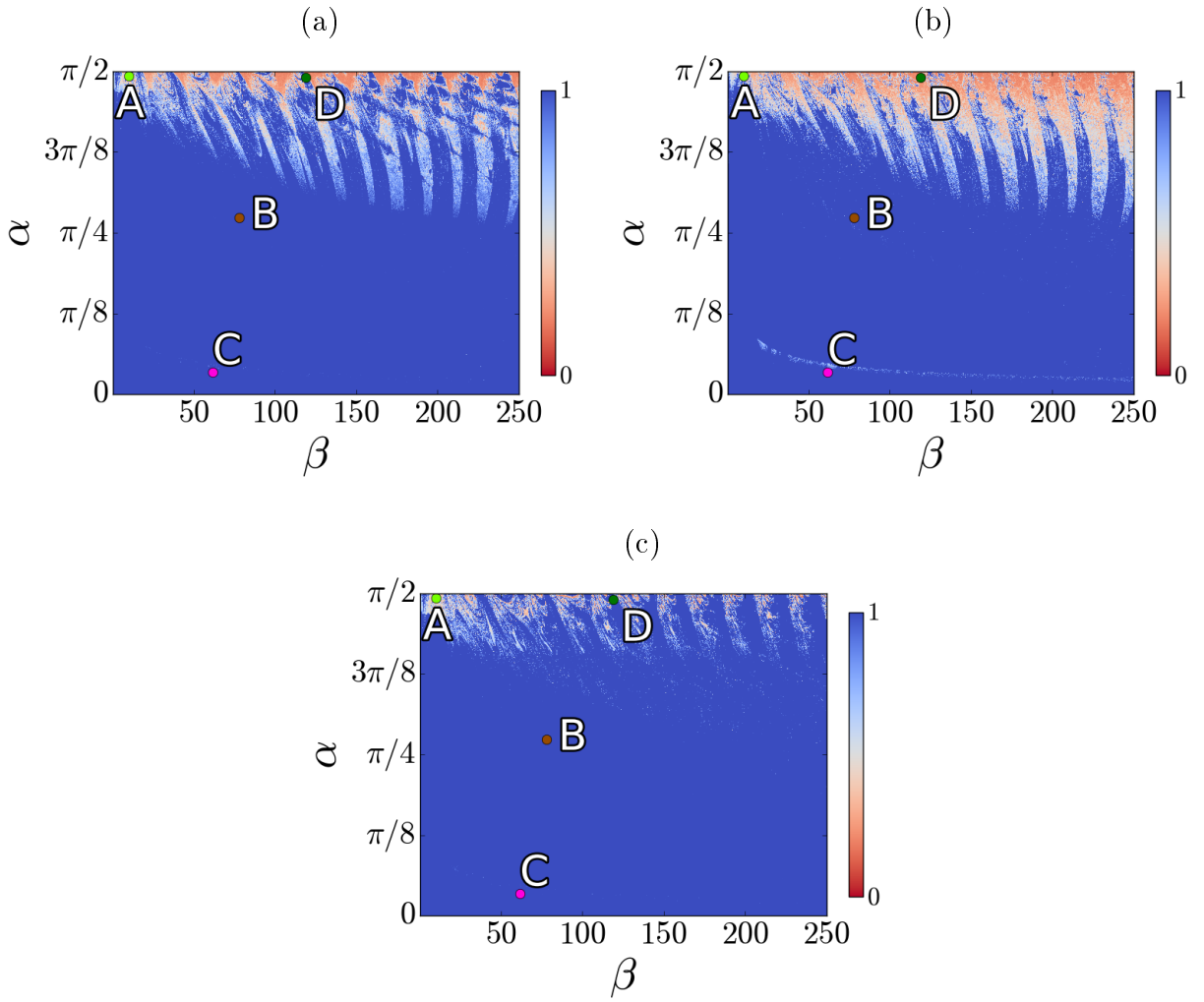

Figure 3.9: Numerical stability diagrams for synchronization within the first (a), second (b), and third (c) groups of oscillators. The color bar indicates the Kuramoto order parameter r calculated for the oscillators' phases within each group. The blue regions with $r = 1$ indicate synchronization within the corresponding group. Points A, B, C correspond to sample points A, B, C from the existence diagram of Fig. 3.5. Point A lies in the instability (red) zones of all three diagrams, rendering the cluster manifold $C_{\Theta\Phi\Psi}$ unstable. Points B and C correspond to a stable $C_{\Theta\Phi\Psi}$. Notice point D with $\alpha = 49\pi/100$ and $\beta = 475/4$ which lies in the stability (blue) regions of diagrams (a) and (c) and in the instability (red) region of diagram (b), thereby corresponding to a one-headed chimera (see Fig. 3.11). Initial conditions are chosen close to the cluster manifold $C_{\Theta\Phi\Psi}$ (see the text for the details). Parameters are as in Fig. 3.5.

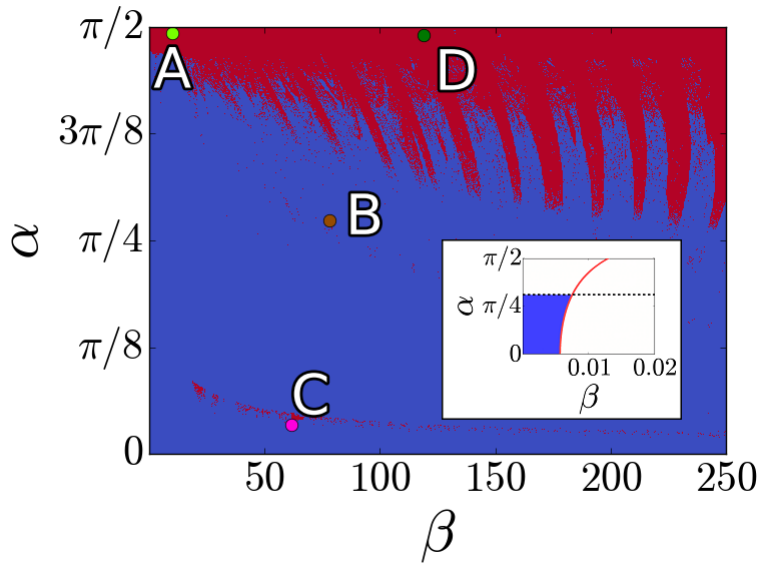

Figure 3.10: Complete diagram for the stability of the three-cluster manifold $C_{\Theta\Phi\Psi}$ combined from the three stability diagrams of Fig. 3.9. Blue indicates regions where all three clusters are stable, and red indicates regions where at least one cluster is unstable. The insert demonstrates the conservative analytical condition (3.38), with its left-hand side bound $\alpha = \arccos\sqrt{2}\gamma$ and right-hand side bound $\alpha = \arccos\frac{1-8\beta\gamma N}{4\beta M}$ plotted by the black dashed and red solid lines, respectively.

Recall that the analytical stability conditions (3.40a)-(3.40b) are applied to each of $q_1(t)$, $q_2(t)$, and $q_3(t)$ to guarantee the stability of the uncoupled variational equations (3.36a), (3.36b), and (3.36c), respectively. Therefore, when the conditions (3.40a)-(3.40b) are violated for q_2, while remaining valid for q_1 and q_3, the trivial fixed point of the variational equations (3.36a)-(3.36c) can become a saddle. In this case, this saddle fixed point can yield a *chimera state*, in which the oscillators within the first and third groups of size N may remain synchronized (as the conditions (3.40a)-(3.40b) for q_1 and q_3 are satisfied), while the oscillators from the second group of size M form an incoherent state. The numerical stability diagrams of Fig. 3.9 indicate that the instability region is the largest for the second cluster (see Fig. 3.9b), and therefore confirm our analytical prediction that the stability conditions

(3.38) are typically violated first through $q_2(t)$ when β increases and $2N > M$, rendering the second cluster unstable. A representative example is the point D which lies in the stability regions of Fig. 3.9a and Fig. 3.9c and in the instability region of Fig. 3.9b. This point corresponds to a one-headed chimera with the "head" being an incoherent state represented by the unstable second cluster, and the "shoulders" determined by the first and third stable clusters (see Fig. 3.11).

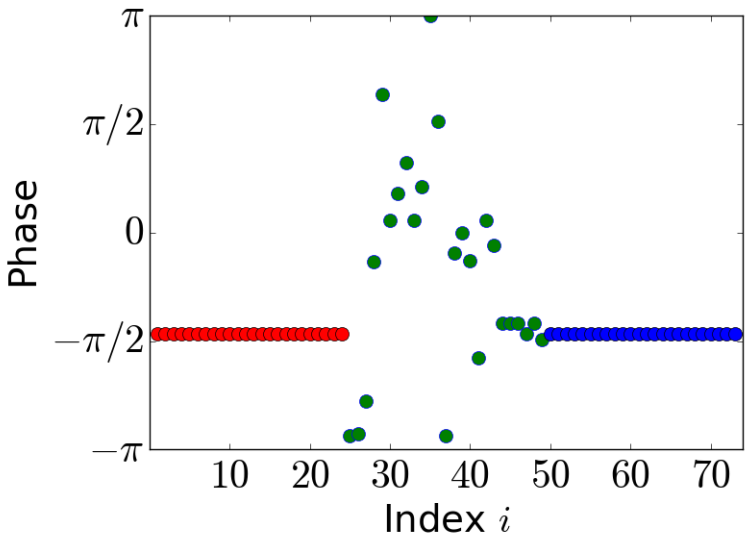

Figure 3.11: Snapshot of a one-headed chimera corresponding to the point D in Fig. 3.9. The oscillators from the second cluster form an incoherent state representing the "head" of the chimera. The phases of oscillators from the first and third clusters are synchronized and rotate around the cylinder in unity, with $y = \Theta - \Psi = 0$.

3.4.2 Co-existing clusters and solitary/chimera states

The initial conditions for calculating the stability diagrams of Fig. 3.9 were chosen close to the three-cluster solution $C_{\Theta\Phi\Psi}$ by perturbing the initial cluster state

$$\begin{aligned} &\Theta(0) = 0,\ \Phi(0) = 0,\ \Psi(0) = 2, \\ &\dot{\Theta}(0) = -1,\ \dot{\Phi}(0) = 0,\ \dot{\Psi}(0) = -2 \end{aligned} \tag{3.46}$$

with an offset ε_l, $l = 1, 2N + M$ of phases Θ_i, $i = 1, ..., N$, Φ_j, $i = 1, ..., M$, and Ψ_k, $k = 1, ..., N$. This offset is spread across the network, linearly increasing from the first oscillator in the first group with $\varepsilon_1 = 0.000014$ to the last oscillator in the third group with $\varepsilon_{2N+M} = \Delta = 0.001$.

To study the non-local stability of synchronization within each of the three cluster groups, we numerically investigate the corresponding basins of attraction. This is performed via calculating the order parameter r for each cluster group, Θ, Φ, and Ψ, as a function of initial phase difference Δ (see Fig. 3.12). The basins of attraction can be highly irregular and depend on the choice of the initial cluster state. More specifically, our simulations indicate that the rotating/rotating chaotic phase shift regime from point B in Fig. 3.9 is fragile and disintegrates as the initial phase difference Δ is initially increased, giving rise to solitary states and chimeras (Fig. 3.12a), when the initial cluster state (3.46) is chosen. Remarkably, this cluster pattern regains its stability with a further increase in Δ and stays stable in a fairly large interval starting from about $\Delta = \pi/8$. The rotating/oscillating chaotic phase shift regime from point C in Fig. 3.9 is robust and remains stable up to initial phase difference $\Delta = 3\pi/8$. Further increase of Δ yields three different solitary states where only very few oscillators within one or two oscillator groups become incoherent (Fig. 3.12b). Figure 3.12c demonstrates the co-existence of the one-headed chimera corresponding to point D in Fig. 3.9 with a hybrid solitary/chimera state (right subplot) where (i) the first group (red) with three out of 24 oscillators being out of synchrony represents a solitary state, (ii) the second group (green) corresponds to an incoherent state, and (iii) the third group represents a fully coherent state. It is important to emphasize that a different choice of the initial cluster state $\Theta(0) = 0,\ \Phi(0) = 0,\ \Psi(0) = \pi,\ \dot{\Theta}(0) = 0,\ \dot{\Psi}(0) = 0,\ \dot{\Phi}(0) = 0$ significantly enlarges the atrraction basin of $C_{\Theta\Phi\Psi}$ at points B and C. That is, the cluster pattern $C_{\Theta\Phi\Psi}$ remains stable across the full range of initial phase difference Δ, varying from 0 to $\pi/2$. In terms of Fig. 3.12, this would imply that the order parameter r for each of the three cluster groups would remain equal to 1 for $\Delta \in [0, \pi/2]$, yielding a trivial diagram with three (red, green, and blue) horizontal lines $r = 1$ and therefore, not shown.

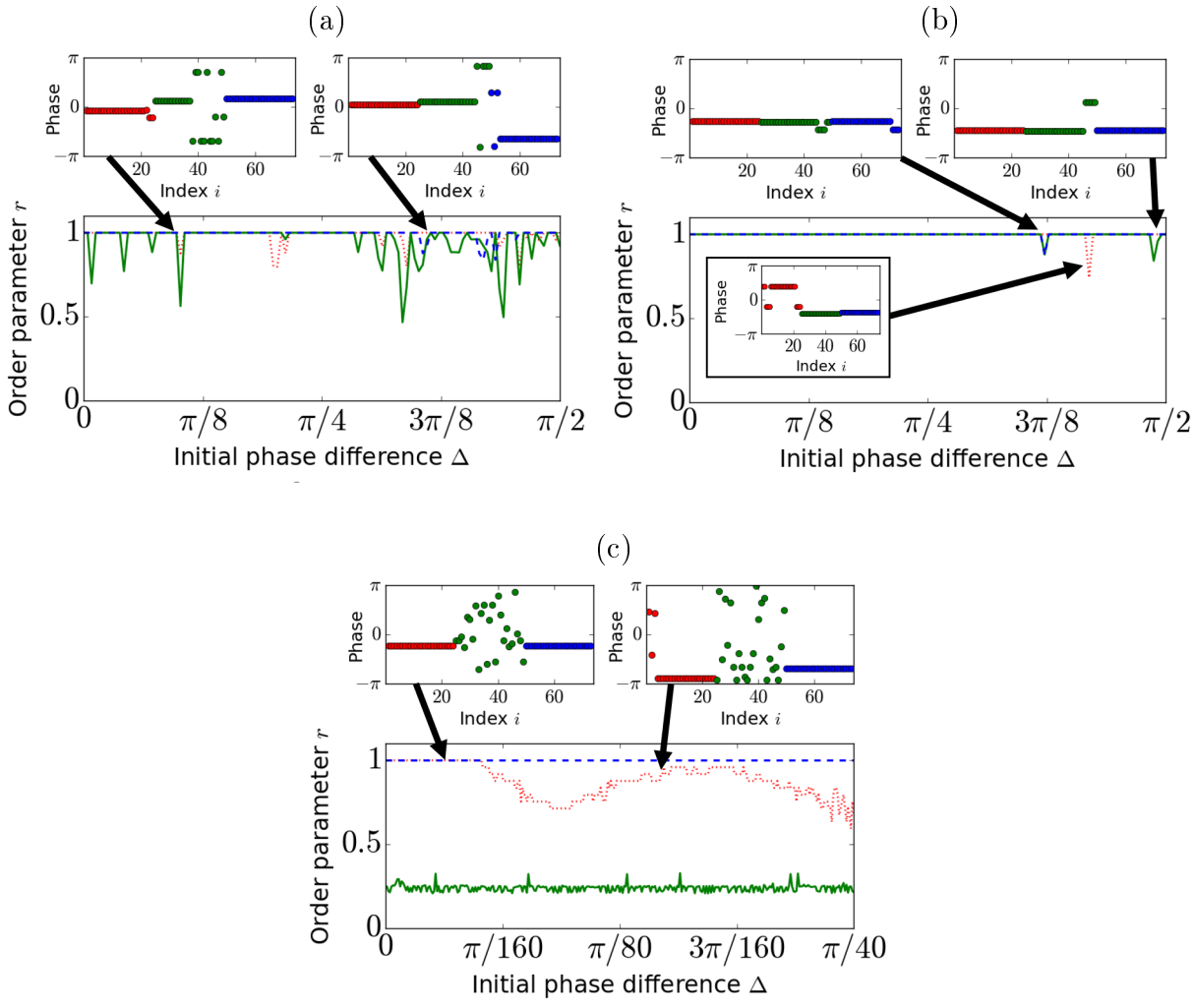

Figure 3.12: Stability of synchronization within each of three cluster groups, Θ, Φ, Ψ, as a function of maximum initial phase difference Δ. Order parameter r is calculated separately for phases $\Theta_1 \dots \Theta_N$ (red dotted line), $\Phi_1 \dots \Phi_M$ (green solid line), and $\Psi_1 \dots \Psi_N$ (blue dashed line). (a): Attraction basin of three-cluster solution $C_{\Theta\Phi\Psi}$ from point B in Fig. 3.9 is highly irregular. The left subplot presents a snapshot of a chimera with only oscillators within the third group (blue) remaining fully synchronized with $r = 1$. The right subplot represents a chimera with the first group (red) being the coherent state with $r = 1$. (b): Wide attraction basin of three-cluster solution $C_{\Theta\Phi\Psi}$ from point B. Significant increase of Δ up to $3\pi/8$ yields three different chimera states (three subplots). (c): Co-existence of two chimeras corresponding to point D from Fig. 3.9 at which the cluster solution $C_{\Theta\Phi\Psi}$ is unstable. The one-headed chimera of Fig. 3.11 (left subplot) remains stable up to $\pi/190$. Note the emergence of solitary states in a region of Δ between $\pi/80$ and $3\pi/160$, where the red dotted curve approaches $r = 1$. The initial cluster state is chosen and perturbed as in (3.46). The plots are displayed after a transient time $T = 10^4$.

3.4.3 Stability of the embedded two-cluster manifold

The diagrams of Figs. 3.9-3.10 provide plenty of insight on the stability of synchronization within the three cluster groups, and therefore, indicate when the three-cluster manifold $C_{\Theta\Phi\Psi}$ is locally stable. However, the stability of $C_{\Theta\Phi\Psi}$ does not necessarily imply the emergence of the corresponding three-cluster pattern with distinct phase shifts x and z. This is due to the fact that the cluster manifold $C_{\Theta\Phi\Psi}$ contains the submanifold $C_{\Theta\Phi\Theta}$ (cf. (3.4)) which represents the largest possible cluster partition of network (3.2) into two clusters where the first and third groups of synchronized oscillators form one cluster, making the phase shifts x and z equal.

In the following, we will analyze the conditions under which the two-cluster solution $C_{\Theta\Phi\Theta}$ is stable, and therefore determine which of the two cluster patterns defined by $C_{\Theta\Phi\Psi}$ and $C_{\Theta\Phi\Theta}$ can stably appear in the network.

Similarly to phase shifts x and z, we introduce the phase difference $y = \Theta - \Psi$ between the phases of the synchronized oscillators in the first and third cluster groups. Note that $y = z - x$. As $\Theta = \Psi$ on the cluster manifold $C_{\Theta\Phi\Theta}$, the stability of solution $y = 0 : \{x = z\}$ implies the stability of $C_{\Theta\Phi\Theta}$ within the larger cluster manifold $C_{\Theta\Phi\Psi}$.

The dynamics on the cluster manifold $C_{\Theta\Phi\Theta}$ is governed by the equation

$$\beta\ddot{x} + \dot{x} = \Omega - \gamma[2N\sin(x-\alpha) + M\sin(x+\alpha)], \tag{3.47}$$

obtained from (3.6) by replacing z with x. Combining the sine terms, we obtain

$$\beta\ddot{x} + \dot{x} + R_1\sin(x+\delta_2) = \Omega, \tag{3.48}$$

where $R_1 = \gamma\sqrt{4N^2 + M^2 + 4MN\cos 2\alpha}$ and $\delta_2 = \arctan\left(\frac{M-2N}{M+2N}\tan\alpha\right)$; the derivation of this equation is similar to that in [14]. Equation (3.48) is a $2D$ pendulum equation which cannot exhibit complex dynamics, so that the phase shift $x = z$ can only be constant or can periodically rotate from $-\pi$ to π as in the classical pendulum equation with a constant

torque [5].

The stable constant phase shift

$$x_e = \arcsin \frac{\Omega}{R_1} - \delta_2 \tag{3.49}$$

is defined by a stable fixed point $E_1(x_e)$ of 2D pendulum equation (3.48) which corresponds to the fixed point $O_1(x_s = x_e + \delta_0)$ of 4D system (3.8). The equation (3.48) also has a saddle point $E_2(x_{sd})$ corresponding to the phase shift

$$x_{sd} = \pi - \arcsin \frac{\Omega}{R_1} + \delta_2. \tag{3.50}$$

The rotating phase shift $x_c(t)$ is determined by a stable limit cycle which is born as a result of a homoclinic bifurcation of saddle E_2 (see [14] for more details on the analysis of the phase shift dynamics in this $2D$ case).

To analyze the stability of cluster manifold $C_{\Theta\Phi\Theta}$ within $C_{\Theta\Phi\Psi}$, we derive the following equation for the difference $y = z - x$:

$$\ddot{y} + \dot{y} = \gamma M(\sin(x + \alpha) - \sin(z + \alpha)), \tag{3.51}$$

obtained by subtracting the x equation from the z equation in (3.6). Using a simple trigonometric identity, we obtain

$$\ddot{y} + \dot{y} = -2\gamma M \sin(y/2) \cos(y/2 + x + \alpha). \tag{3.52}$$

In the limit of infinitesimal y when $\sin(y/2) \approx y/2$ and $\cos(y/2 + x + \alpha) \approx \cos(x + \alpha)$, we turn (3.52) into the equation

$$\ddot{y} + \dot{y} + \gamma M \cos(x + \alpha) y = 0 \tag{3.53}$$

which determines the local stability of the origin corresponding to phase shift $y = 0$. Note

that (3.53) is a linear equation with a coefficient which is governed by phase shift x that may be constant or vary in time.

Case I: Constant phase shift x_e. In this simple case, the equation (3.53) becomes a linear equation with a constant coefficient. As a result, it is stable at fixed point $E_1(x_e)$ iff

$$\cos(x_e + \alpha) > 0, \tag{3.54}$$

yielding the condition $\alpha < \pi/2 - x_e$. Thus, we obtain the following necessary and sufficient condition for the local stability of cluster solution $C_{\Theta\Phi\Theta}$ with a constant phase shift x_e :

$$\alpha < \alpha_{cr} = \pi/2 - \arcsin\frac{\Omega}{R_1} + \delta_2, \tag{3.55}$$

provided that $\Omega = (M - N)\sin\alpha \leq R_1$, ensuring the existence of fixed point $E_1(x_e)$.

Checking the stability condition (3.54) for the saddle point $E_2(x_{sd})$ with x_{sd} defined in (3.50), we obtain the inequality $\alpha < \pi/2 - x_{sd}$ which guarantees that saddle $E_2(x_{sd})$ is locally stable in the transversal direction to $C_{\Theta\Phi\Theta}$. Substituting (3.50) into this inequality yields $\alpha < x_e - \pi/2$ which becomes the following transversal stability condition for saddle $E_2(x_{sd})$:

$$\alpha < \alpha^* = -\pi/2 + \arcsin\frac{\Omega}{R_1} - \delta_2 = -\alpha_{cr}. \tag{3.56}$$

Comparing (3.55) and (3.56), we conclude that two fixed points $E_1(x_e)$ and $E_2(x_{sd})$ cannot be stable simultaneously so that the transversal stability of point $E_1(x_e)$ guarantees the transversal instability of saddle $E_2(x_{sd})$ on cluster manifold $C_{\Theta\Phi\Theta}$. This property provides an escape mechanism by which trajectories close to saddle $E_2(x_{sd})$ can leave $C_{\Theta\Phi\Theta}$, while staying on the larger-dimensional manifold $C_{\Theta\Phi\Psi}$ when the latter is stable. This leads to the *bistability* of two cluster patterns which is indeed observed in the network (see Fig. 3.13a). Notice that the initial conditions used for generating the stability diagrams of Figs. 3.9-3.10 yield the instability of two-cluster solution $C_{\Theta\Phi\Theta}$ with a time-varying phase shift at points B and C (Fig. 3.13a). However, the analytical condition (3.55) (red horizontal dashed line)

guarantees that the two-cluster solution $C_{\Theta\Phi\Theta}$ with a constant phase shift $x_e = z_e$ is locally stable at points B and C. This is in perfect agreement with the above stability argument and indicates the bistability of the co-existing three-cluster solution $C_{\Theta\Phi\Psi}$ with the chaotic shifts (see Figs. 3.7-3.8) and the two-cluster pattern $C_{\Theta\Phi\Theta}$ with the constant phase shift $x_e = z_e$. We have numerically verified that the attraction basin of this two-cluster solution is significantly smaller than that of the three-cluster solution with the chaotic phase shifts [not shown]. This bistability is present in a large region of parameters (the yellow region under the red dashed line) and ceases to exist for smaller values of parameter α (the green region). Sample point E corresponds to the two-cluster solution $C_{\Theta\Phi\Theta}$ with a constant phase shift (Fig. 3.13b) which remains stable as guaranteed by the stability condition (3.55) whereas the three-cluster solution becomes unstable.

Comparing the stability diagram of Fig. 3.13a with the existence diagram of Fig. 3.3 suggests that the three-cluster pattern defined by $C_{\Theta\Phi\Psi}$ with constant phase shifts $x(t) \neq z(t)$ does not stably appear in the network, at least for the chosen initial conditions. To verify this claim, one should notice that the existence region of $C_{\Theta\Phi\Psi}$ with constant phase shifts $x(t) \neq z(t)$ (the highly irregular white region in Fig. 3.3) coincides with the stability region for two-cluster pattern $C_{\Theta\Phi\Theta}$ with a constant shift $x_e = z_e$ (the green region in Fig. 3.13a). As a result, this three-cluster pattern becomes transient and eventually transforms into the two-cluster pattern with a constant shift.

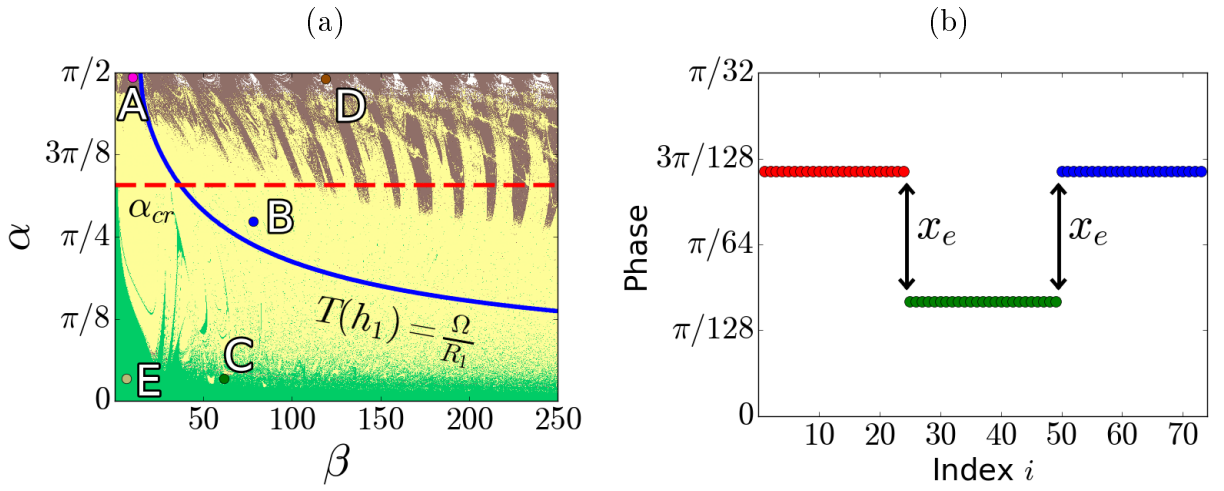

Figure 3.13: (a): Stability diagram of two-cluster solution $C_{\Theta\Phi\Theta}$ with $y = z - x = 0$. Green indicates stability regions where $C_{\Theta\Phi\Theta}$ with a constant phase shift $x_c = z_c$ is stable ($y = 0$ is stable). Yellow depicts regions where $C_{\Theta\Phi\Theta}$ is unstable for the chosen initial conditions but the three-cluster solution $C_{\Theta\Phi\Psi}$ with time-varying shifts $x(t)$ and $z(t)$ is stable. Brown indicates regions where both $C_{\Theta\Phi\Theta}$ and $C_{\Theta\Phi\Psi}$ are unstable. White depicts the regions where one-headed chimeras with stable $y = \Theta - \Psi = 0$ emerge (the chimera of Fig. 3.11 is an example). Sample points A, B, C, and D are as in Figs. 3.9-3.10. Points B and C lie in the instability (yellow) regions of $y = 0$. The region under the horizontal dashed line $\alpha = \alpha_{cr} = 1.0335$ corresponds to the stability condition (3.55). Sample point E lies in the stability region. The blue solid line indicates the Tricomi homoclinic curve $\Omega/R_1 = T(h_1)$ in system (3.48). Initial conditions and other parameters are as in Figs. 3.9-3.10. (b): Snapshot of the two-cluster pattern with constant phase shift x_e, corresponding to point E.

Case II: Rotating phase shift $x_c(t)$. A stable limit cycle $x_c(t)$ exists in the pendulum system (3.48) when $\Omega/R_1 > T(h_1)$, where $T(h_1)$ is the Tricomi homoclinic curve (3.30) with $h_1 = 1/\sqrt{\beta R_1}$. Since $x_c(t)$ periodically varies from $-\pi$ to π, the factor $\cos(x + \alpha)$ in (3.53) oscillates between positive and negative numbers. Therefore, the stability condition $\cos(x_c(t) + \alpha) > 0$ may only be satisfied on average, thereby preventing a general analytical analysis and requiring the use of numerical simulations. However, we manage to approximately estimate the stability of $\cos(x_c(t) + \alpha) > 0$ in a particular case where the parameters

β and α are chosen slightly above the Tricomi homoclinic curve $\Omega/R_1 = T(h_1)$ (the blue solid line in Fig. 3.13a). Here, the stable limit cycle $x_c(t)$ inherits the shape of the homoclinic orbit of $E_2(x_{sd})$ from which it was born. Therefore, the limit cycle spends most of the time in a vicinity of saddle $E_2(x_{sd})$ with an exception of a comparably short time of switching from x_{sd} to $x_{sd}+2\pi$, so that $x_c(t) \approx x_{sd}$. Therefore, the condition for its transversal stability can be approximated as follows

$$\cos(x_c(t) + \alpha) \approx \cos(x_{sd} + \alpha) > 0 \tag{3.57}$$

which coincides with condition (3.56) for the transversal stability of saddle $E_2(x_{sd})$. This implies that the stability condition (3.57) cannot be satisfied as long as the two-cluster solution $C_{\Theta\Phi\Theta}$ with a constant phase shift x_e is stable (cf. (3.55) and (3.56)). Hence, we can conclude that two-cluster pattern $C_{\Theta\Phi\Theta}$ with a rotating phase shift $x_c(t) = z_c(t)$ is unstable in a parameter region slightly above the Tricomi homoclinic curve $\Omega/R_1 = T(h_1)$ and below the stability line $\alpha = \alpha_{cr}$ (red dashed line). Sample point B is located in this parameter region; our numerical simulations confirm that the two-cluster pattern $C_{\Theta\Phi\Theta}$ with a time-varying shift $x_c(t)$ is unstable at point B, thereby preserving the bistability of three-cluster pattern $C_{\Theta\Phi\Psi}$ with chaotic rotating/rotating phase shift and two-cluster pattern $C_{\Theta\Phi\Psi}$ with a constant phase shift.

3.5 Conclusions and discussion

The classical Kuramoto model of coupled first-order phase oscillators is known to exhibit various forms of spatio-temporal chaotic behavior, including phase chaos [85], mean-field chaotic dynamics in infinite [76] and finite-size networks [26, 25], chaotic weak chimeras [24, 64], and chaotic transients [108]. The emergence of chaos in the macroscopic dynamics of the Kuramoto model is traditionally attributed to oscillators' heterogeneity (see [76, 92] and references therein). However, it was also shown that even symmetric systems of identical oscillators can induce chaotic dynamics in small-size Kuramoto networks of two populations

[26, 25].

In this chapter, we have revealed and carefully analyzed a different form of chaotic behavior such as chaotic inter-cluster phase dynamics in a three-group network of identical second-order Kuramoto oscillators with inertia. The groups have different sizes and can split into clusters where the oscillators synchronize within a cluster while there is a pairwise phase shift between the dynamics of the clusters. Due to the presence of inertia, which increases the dimensionality of the oscillator dynamics, these phase shifts can exhibit different forms of chaotic behavior, including oscillatory, rotatory, and mixed-mode oscillations. We demonstrated that the phase shift dynamics is governed by a 4D system of two nonlinearly coupled driven pendulums. We have applied an auxiliary system approach to analyzing possible solutions of the 4D system and derived bounds on parameter partitions that support the co-existence of different chaotic inter-cluster dynamics. A representative example of these dynamics is a regime in which the phase shift between the first and second groups of oscillators chaotically oscillates within a small phase range, while the phase shift between the second and third groups chaotically rotates from $-\pi$ to π. The bounds that separate the parameter regions of oscillatory and rotatory dynamics are explicit in the parameters of the network model. Therefore, they clearly highlight possible routes of transitions between the chaotic dynamics which can be induced by varying only one control parameter such as phase lag α or inertia β. To identify a primary cause of chaotic dynamics in the 4D system, we have proved the existence of a Shilnikov homoclinic orbit to a saddle-focus which leads to the emergence of spiral chaos [91].

Remarkably, the addition of only one oscillator to the three-group network with equal group sizes $M = N$, which yields asymmetry and the existence of the three-cluster pattern, is sufficient to induce large-amplitude chaotic oscillations of the phase shifts. Our extensive numerical analysis not reported in this chapter also suggests that, in contrast to one's expectations, smaller differences in the group sizes are more effective in promoting phase shift chaos. Ultimately, the smallest network which can exhibit chaotic phase-shifts consists of four second-order oscillators, with two oscillators forming the second group ($M = 2$) and

one oscillator in each of the first and third groups ($N = 1$). The chosen network setup with no direct connections between the first and third groups could be viewed as an optimal configuration which minimizes the complexity of the governing 4D system. Connecting the two groups could make the phase shift dynamics even richer but it would introduce additional terms and make the 4D system less tractable analytically. Extending our analysis of inter-cluster phase dynamics to finer cluster partitions within each group, including solitary cluster states, is possible. However, the governing system will have a high dimension and might not necessary be represented by a system of well separated coupled pendulums. Again, rigorous analysis of its possible chaotic states and transitions between them becomes more challenging. These problems are a subject of future study.

We have also analyzed the stability of the three-cluster pattern and its embedding, a two-cluster pattern, in which the first and third groups of oscillators become synchronized. Our analysis has explicitly demonstrated that the phase shift dynamics can be multistable, including the case where the three-cluster pattern with chaotically oscillating phase shift stably co-exists with the two-cluster pattern with a constant shift. Our stability conditions also have implications to the emergence of chimera states. Due to the simple network structure, these conditions are uncoupled and applied to each group of oscillators separately. Thus, the simultaneous fulfillment of the stability condition for synchronization within one group and its failure for synchronization within the others can offer a key to predicting the emergence of a chimera state. These observations are in good agreement with our numerical results that confirmed the emergence of a plethora of co-existing chimera states in the network.

Our analysis can also be extended to networks with evolving [11], stochastically switching [51] or adaptive connections [23]. These networks exhibit highly-nontrivial dynamics, including the emergence of macroscopic chaos [94, 93], ghost attractors [9] and windows of opportunity [55, 44] due to time-varying coupling. The role of time-varying connections in the emergence of stable or meta-stable clusters and ghost patterns in Kuramoto networks with inertia is to be explored.

Although our analysis provides an unprecedented understanding of the emergence and

co-existence of stable clusters with chaotic inter-cluster phase dynamics, we have only scratched the surface of a complex interplay between the existence of possible clusters, intrinsic oscillator dynamics, and nonlinear interactions of phases. The richness of the dynamics in our fairly simple and analytically tractable network model opens the door to further discovering new types of dynamical effects and cooperative structures in multi-population networks of phase oscillators with inertia.

REFERENCES

[1] Daniel M Abrams, Rennie Mirollo, Steven H Strogatz, and Daniel A Wiley. Solvable model for chimera states of coupled oscillators. *Physical Review Letters*, 101(8):084103, 2008.

[2] Daniel M Abrams and Steven H Strogatz. Chimera states for coupled oscillators. *Physical Review Letters*, 93(17):174102, 2004.

[3] JA Acebron, LL Bonilla, CPJ Vicente, F Ritort, and R Spigler. A simple paradigm for synchronization phenomena: The kuramoto model. *Rev. Mod. Phys*, 77:137–185, 2005.

[4] Juan A Acebrón, Luis L Bonilla, Conrad J Pérez Vicente, Félix Ritort, and Renato Spigler. The kuramoto model: A simple paradigm for synchronization phenomena. *Reviews of modern physics*, 77(1):137, 2005.

[5] Aleksandr Aleksandrovich Andronov, Aleksandr Adol'fovich Vitt, and Semen Emmanuilovich Khaikin. *Theory of Oscillators: Adiwes International Series in Physics*, volume 4. Elsevier, 2013.

[6] Peter Ashwin and Oleksandr Burylko. Weak chimeras in minimal networks of coupled phase oscillators. *Chaos: An Interdisciplinary Journal of Nonlinear Science*, 25(1):013106, 2015.

[7] Ernest Barreto, Brian Hunt, Edward Ott, and Paul So. Synchronization in networks of networks: The onset of coherent collective behavior in systems of interacting populations of heterogeneous oscillators. *Physical Review E*, 77(3):036107, 2008.

[8] I Belykh, V Belykh, K Nevidin, and M Hasler. Persistent clusters in lattices of coupled nonidentical chaotic systems. *Chaos: An Interdisciplinary Journal of Nonlinear Science*, 13(1):165–178, 2003.

[9] Igor Belykh, Vladimir Belykh, Russell Jeter, and Martin Hasler. Multistable randomly switching oscillators: The odds of meeting a ghost. *The European Physical Journal Special Topics*, 222(10):2497–2507, 2013.

[10] Igor Belykh, Enno De Lange, and Martin Hasler. Synchronization of bursting neurons: What matters in the network topology. *Physical review letters*, 94(18):188101, 2005.

[11] Igor Belykh, Mario Di Bernardo, Jürgen Kurths, and Maurizio Porfiri. Evolving dynamical networks. *Physica D: Nonlinear Phenomena*, 267:1–6, 2014.

[12] Igor Belykh and Martin Hasler. Mesoscale and clusters of synchrony in networks of bursting neurons. *Chaos: An Interdisciplinary Journal of Nonlinear Science*, 21(1):016106, 2011.

[13] Igor Belykh, Russell Jeter, and Vladimir Belykh. Foot force models of crowd dynamics on a wobbly bridge. *Science Advances*, 3(11):e1701512, 2017.

[14] Igor V Belykh, Barrett N Brister, and Vladimir N Belykh. Bistability of patterns of synchrony in kuramoto oscillators with inertia. *Chaos: An Interdisciplinary Journal of Nonlinear Science*, 26(9):094822, 2016.

[15] Igor V Belykh, Russell Jeter, and Vladimir N Belykh. Bistable gaits and wobbling induced by pedestrian-bridge interactions. *Chaos: An Interdisciplinary Journal of Nonlinear Science*, 26(11):116314, 2016.

[16] Vladimir N Belykh, Igor V Belykh, and Martin Hasler. Hierarchy and stability of partially synchronous oscillations of diffusively coupled dynamical systems. *Physical Review E*, 62(5):6332, 2000.

[17] Vladimir N Belykh, Igor V Belykh, and Martin Hasler. Connection graph stability method for synchronized coupled chaotic systems. *Physica D: Nonlinear Phenomena*, 195(1-2):159–187, 2004.

[18] Vladimir N Belykh, Igor V Belykh, and Erik Mosekilde. Cluster synchronization modes in an ensemble of coupled chaotic oscillators. *Physical Review E*, 63(3):036216, 2001.

[19] Vladimir N Belykh and Evgeniya V Pankratova. Shilnikov chaos in oscillators with huygens coupling. *International Journal of Bifurcation and Chaos*, 24(08):1440007, 2014.

[20] Vladimir N Belykh, Valentin S Petrov, and Grigorii Vladimirovich Osipov. Dynamics of the finite-dimensional kuramoto model: Global and cluster synchronization. *Regular and Chaotic Dynamics*, 20(1):37–48, 2015.

[21] VN Belykh, Maxim Ilich Bolotov, and Grigory Vladimirovich Osipov. Kuramoto phase model with inertia: bifurcations leading to the loss of synchrony and to the emergence of chaos. *Modeling and Analysis of Information Systems*, 22(5):595–608, 2015.

[22] VN Belykh, Niels Falsig Pedersen, and OH Soerensen. Shunted-josephson-junction model. i. the autonomous case. *Physical Review B*, 16(11):4853, 1977.

[23] Rico Berner, Eckehard Scholl, and Serhiy Yanchuk. Multiclusters in networks of adaptively coupled phase oscillators. *SIAM Journal on Applied Dynamical Systems*, 18(4):2227–2266, 2019.

[24] Christian Bick and Peter Ashwin. Chaotic weak chimeras and their persistence in coupled populations of phase oscillators. *Nonlinearity*, 29(5):1468, 2016.

[25] Christian Bick, Mark J Panaggio, and Erik A Martens. Chaos in kuramoto oscillator networks. *Chaos: An Interdisciplinary Journal of Nonlinear Science*, 28(7):071102, 2018.

[26] Christian Bick, Marc Timme, Danilo Paulikat, Dirk Rathlev, and Peter Ashwin. Chaos in symmetric phase oscillator networks. *Physical Review Letters*, 107(24):244101, 2011.

[27] Karen Blaha, Ryan J Burrus, Jorge L Orozco-Mora, Elvia Ruiz-Beltrán, Abu B Siddique, V D Hatamipour, and Francesco Sorrentino. Symmetry effects on naturally

arising chimera states in mechanical oscillator networks. *Chaos: An Interdisciplinary Journal of Nonlinear Science*, 26(11):116307, 2016.

[28] Stefano Boccaletti, Jürgen Kurths, Grigory Osipov, DL Valladares, and CS Zhou. The synchronization of chaotic systems. *Physics reports*, 366(1-2):1–101, 2002.

[29] Stefano Boccaletti, Vito Latora, Yamir Moreno, Martin Chavez, and D-U Hwang. Complex networks: Structure and dynamics. *Physics Reports*, 424(4-5):175–308, 2006.

[30] Barrett N Brister, Igor V Belykh, and Vladimir N Belykh. Multistable cluster rhythms in networks of coupled rotators. *Proceedings of the 9th International Conference "Physics and Control"*, pages 1–6, 2019.

[31] Barrett N Brister, Vladimir N Belykh, and Igor V Belykh. When three is a crowd: Chaos from clusters of kuramoto oscillators with inertia. *Physical Review E*, 101(6):062206, 2020.

[32] John Buck and Elisabeth Buck. Synchronous fireflies. *Scientific American*, 234(5):74–85, 1976.

[33] Scott Camazine, Jean-Louis Deneubourg, Nigel R Franks, James Sneyd, Eric Bonabeau, and Guy Theraulaz. *Self-organization in Biological Systems*, volume 7. Princeton University Press, 2003.

[34] Young-Pil Choi, Seung-Yeal Ha, and Seok-Bae Yun. Complete synchronization of kuramoto oscillators with finite inertia. *Physica D: Nonlinear Phenomena*, 240(1):32–44, 2011.

[35] Patricia S Churchland and Terrence J Sejnowski. *The Computational Brain*. MIT press, 2016.

[36] James J Collins and Ian N Stewart. Coupled nonlinear oscillators and the symmetries of animal gaits. *Journal of Nonlinear Science*, 3(1):349–392, 1993.

[37] Pietro DeLellis, Giovanni Polverino, Gozde Ustuner, Nicole Abaid, Simone Macrì, Erik M Bollt, and Maurizio Porfiri. Collective behaviour across animal species. *Scientific reports*, 4:3723, 2014.

[38] Boris Pavlovich Demidovich. *Lectures on Stability Theory*. Nauka, Moscow, 1967.

[39] Jiajie Ding, Igor Belykh, Alireza Marandi, and Mohammad-Ali Miri. Dispersive versus dissipative coupling for frequency synchronization in lasers. *Physical Review Applied*, 12(5):054039, 2019.

[40] Florian Dörfler and Francesco Bullo. On the critical coupling for kuramoto oscillators. *SIAM Journal on Applied Dynamical Systems*, 10(3):1070–1099, 2011.

[41] Bruno Eckhardt, Edward Ott, Steven H Strogatz, Daniel M Abrams, and Allan McRobie. Modeling walker synchronization on the millennium bridge. *Physical Review E*, 75(2):021110, 2007.

[42] Bard Ermentrout. An adaptive model for synchrony in the firefly pteroptyx malaccae. *Journal of Mathematical Biology*, 29(6):571–585, 1991.

[43] Leon Glass and Michael C Mackey. *From clocks to chaos: The rhythms of life*. Princeton University Press, 1988.

[44] Olga Golovneva, Russell Jeter, Igor Belykh, and Maurizio Porfiri. Windows of opportunity for synchronization in stochastically coupled maps. *Physica D: Nonlinear Phenomena*, 340:1–13, 2017.

[45] Martin Golubitsky and Ian Stewart. Nonlinear dynamics of networks: the groupoid formalism. *Bulletin of the american mathematical society*, 43(3):305–364, 2006.

[46] Martin Golubitsky, Ian Stewart, and Andrei Török. Patterns of synchrony in coupled cell networks with multiple arrows. *SIAM Journal on Applied Dynamical Systems*, 4(1):78–100, 2005.

[47] John Guckenheimer and Philip Holmes. *Nonlinear oscillations, dynamical systems, and bifurcations of vector fields*, volume 42. Springer Science & Business Media, 2013.

[48] Michael R Guevara, Alvin Shrier, and Leon Glass. Phase-locked rhythms in periodically stimulated heart cell aggregates. *American Journal of Physiology-Heart and Circulatory Physiology*, 254(1):H1–H10, 1988.

[49] Seung-Yeal Ha, Yongduck Kim, and Zhuchun Li. Large-time dynamics of kuramoto oscillators under the effects of inertia and frustration. *SIAM Journal on Applied Dynamical Systems*, 13(1):466–492, 2014.

[50] Constance Hammond, Hagai Bergman, and Peter Brown. Pathological synchronization in parkinson's disease: networks, models and treatments. *Trends in Neurosciences*, 30(7):357–364, 2007.

[51] Martin Hasler, Vladimir Belykh, and Igor Belykh. Dynamics of stochastically blinking systems. part ii: Asymptotic properties. *SIAM Journal on Applied Dynamical Systems*, 12(2):1031–1084, 2013.

[52] Johanne Hizanidis, Nikos E Kouvaris, Gorka Zamora-López, Albert Díaz-Guilera, and Chris G Antonopoulos. Chimera-like states in modular neural networks. *Scientific reports*, 6:19845, 2016.

[53] Hyunsuk Hong, Hugues Chaté, Hyunggyu Park, and Lei-Han Tang. Entrainment transition in populations of random frequency oscillators. *Physical Review Letters*, 99(18):184101, 2007.

[54] Patrycja Jaros, Serhiy Brezetsky, Roman Levchenko, Dawid Dudkowski, Tomasz Kapitaniak, and Yuri Maistrenko. Solitary states for coupled oscillators with inertia. *Chaos: An Interdisciplinary Journal of Nonlinear Science*, 28(1):011103, 2018.

[55] Russell Jeter and Igor Belykh. Synchronization in on-off stochastic networks: win-

dows of opportunity. *IEEE Transactions on Circuits and Systems I: Regular Papers*, 62(5):1260–1269, 2015.

[56] Peng Ji, Thomas KDM Peron, Francisco A Rodrigues, and Jürgen Kurths. Low-dimensional behavior of kuramoto model with inertia in complex networks. *Scientific Reports*, 4, 2014.

[57] Hiroko Kamei and Peter JA Cock. Computation of balanced equivalence relations and their lattice for a coupled cell network. *SIAM Journal on Applied Dynamical Systems*, 12(1):352–382, 2013.

[58] Maxim Komarov, Shamik Gupta, and Arkady Pikovsky. Synchronization transitions in globally coupled rotors in the presence of noise and inertia: Exact results. *EPL (Europhysics Letters)*, 106(4):40003, 2014.

[59] Yoshiki Kuramoto. International symposium on mathematical problems in theoretical physics. *Lecture notes in Physics*, 30:420, 1975.

[60] Yoshiki Kuramoto. Self-entrainment of a population of coupled non-linear oscillators. In *International Symposium on Mathematical Problems in Theoretical Physics*, pages 420–422. Springer, 1975.

[61] Yoshiki Kuramoto and Dorjsuren Battogtokh. Coexistence of coherence and incoherence in nonlocally coupled phase oscillators. *Nonlinear Phenomena in Complex Systems*, 5(4):380–385, 2002.

[62] Carlo R Laing. Dynamics and stability of chimera states in two coupled populations of oscillators. *Physical Review E*, 100(4):042211, 2019.

[63] Yu Maistrenko, O Popovych, O Burylko, and PA Tass. Mechanism of desynchronization in the finite-dimensional kuramoto model. *Physical review letters*, 93(8):084102, 2004.

[64] Yuri Maistrenko, Serhiy Brezetsky, Patrycja Jaros, Roman Levchenko, and Tomasz Kapitaniak. Smallest chimera states. *Physical Review E*, 95(1):010203, 2017.

[65] Erik Andreas Martens, E Barreto, SH Strogatz, E Ott, P So, and TM Antonsen. Exact results for the kuramoto model with a bimodal frequency distribution. *Physical Review E*, 79(2):026204, 2009.

[66] Erik Andreas Martens, Shashi Thutupalli, Antoine Fourrière, and Oscar Hallatschek. Chimera states in mechanical oscillator networks. *Proceedings of the National Academy of Sciences USA*, 110(26):10563–10567, 2013.

[67] Kenji Mizuseki and György Buzsaki. Theta oscillations decrease spike synchrony in the hippocampus and entorhinal cortex. *Philosophical Transactions of the Royal Society B: Biological Sciences*, 369(1635):20120530, 2014.

[68] Adilson E Motter, Seth A Myers, Marian Anghel, and Takashi Nishikawa. Spontaneous synchrony in power-grid networks. *Nature Physics*, 9(3):191–197, 2013.

[69] VO Munyaev, LA Smirnov, VA Kostin, GV Osipov, and A Pikovsky. Analytical approach to synchronous states of globally coupled noisy rotators. *New Journal of Physics*, 22(2):023036, 2020.

[70] Theoden I Netoff and Steven J Schiff. Decreased neuronal synchronization during experimental seizures. *Journal of Neuroscience*, 22(16):7297–7307, 2002.

[71] Mark EJ Newman. The structure and function of complex networks. *SIAM Review*, 45(2):167–256, 2003.

[72] Takashi Nishikawa and Adilson E Motter. Network synchronization landscape reveals compensatory structures, quantization, and the positive effect of negative interactions. *Proceedings of the National Academy of Sciences*, 107(23):10342–10347, 2010.

[73] Simona Olmi. Chimera states in coupled kuramoto oscillators with inertia. *Chaos: An Interdisciplinary Journal of Nonlinear Science*, 25(12):123125, 2015.

[74] Simona Olmi, Adrian Navas, Stefano Boccaletti, and Alessandro Torcini. Hysteretic transitions in the kuramoto model with inertia. *Physical Review E*, 90(4):042905, 2014.

[75] Oleh E Omelchenko. Coherence–incoherence patterns in a ring of non-locally coupled phase oscillators. *Nonlinearity*, 26(9):2469, 2013.

[76] Edward Ott and Thomas M Antonsen. Low dimensional behavior of large systems of globally coupled oscillators. *Chaos: An Interdisciplinary Journal of Nonlinear Science*, 18(3):037113, 2008.

[77] Mark J Panaggio and Daniel M Abrams. Chimera states: coexistence of coherence and incoherence in networks of coupled oscillators. *Nonlinearity*, 28(3):R67, 2015.

[78] Mark J Panaggio, Daniel M Abrams, Peter Ashwin, and Carlo R Laing. Chimera states in networks of phase oscillators: the case of two small populations. *Physical Review E*, 93(1):012218, 2016.

[79] Louis M Pecora and Thomas L Carroll. Master stability functions for synchronized coupled systems. *Physical review letters*, 80(10):2109, 1998.

[80] Louis M Pecora, Francesco Sorrentino, Aaron M Hagerstrom, Thomas E Murphy, and Rajarshi Roy. Cluster synchronization and isolated desynchronization in complex networks with symmetries. *Nature communications*, 5(1):1–8, 2014.

[81] Arkady Pikovsky and Michael Rosenblum. Partially integrable dynamics of hierarchical populations of coupled oscillators. *Physical Review Letters*, 101(26):264103, 2008.

[82] Arkady Pikovsky, Michael Rosenblum, and Jürgen Kurths. *Synchronization: a Universal Concept in Nonlinear Sciences*, volume 12. Cambridge University Press, 2003.

[83] Alexander Pogromsky and Henk Nijmeijer. Cooperative oscillatory behavior of mutually coupled dynamical systems. *IEEE Transactions on Circuits and Systems I: Fundamental Theory and Applications*, 48(2):152–162, 2001.

[84] Alexander Pogromsky, Giovanni Santoboni, and Henk Nijmeijer. Partial synchronization: from symmetry towards stability. *Physica D: Nonlinear Phenomena*, 172(1-4):65–87, 2002.

[85] Oleksandr V Popovych, Yuri L Maistrenko, and Peter A Tass. Phase chaos in coupled oscillators. *Physical Review E*, 71(6):065201, 2005.

[86] M Prevedelli, T Freegarde, and TW Hänsch. Phase locking of grating-tuned diode lasers. *Applied Physics B Lasers and Optics*, 60(2):3, 1995.

[87] Rajarshi Roy and K Scott Thornburg Jr. Experimental synchronization of chaotic lasers. *Physical Review Letters*, 72(13):2009, 1994.

[88] Hidetsugu Sakaguchi. Instability of synchronized motion in nonlocally coupled neural oscillators. *Physical Review E*, 73(3):031907, 2006.

[89] Kaspar Schindler, Christian E Elger, and Klaus Lehnertz. Increasing synchronization may promote seizure termination: evidence from status epilepticus. *Clinical Neurophysiology*, 118(9):1955–1968, 2007.

[90] L. P. Shilnikov, A. L. Shilnikov, D. V. Turaev, and L. Chua. *Qualitative Theory in Nonlinear Dynamics. Part II.* World Scientific, 2001.

[91] Leonid Pavlovich Shilnikov. A case of the existence of a denumerable set of periodic motions. *Doklady Akademii Nauk*, 160(3):558–561, 1965.

[92] Per Sebastian Skardal, Juan G Restrepo, and Edward Ott. Frequency assortativity can induce chaos in oscillator networks. *Physical Review E*, 91(6):060902, 2015.

[93] Per Sebastian Skardal, Dane Taylor, and Juan G Restrepo. Complex macroscopic behavior in systems of phase oscillators with adaptive coupling. *Physica D: Nonlinear Phenomena*, 267:27–35, 2014.

[94] Paul So and Ernest Barreto. Generating macroscopic chaos in a network of globally coupled phase oscillators. *Chaos: An Interdisciplinary Journal of Nonlinear Science*, 21(3):033127, 2011.

[95] Francesco Sorrentino, Louis M Pecora, Aaron M Hagerstrom, Thomas E Murphy, and Rajarshi Roy. Complete characterization of the stability of cluster synchronization in complex dynamical networks. *Science Advances*, 2(4):e1501737, 2016.

[96] SH Strogatz. Nonlinear dynamics and chaos: with applications to physics, biology and chemistry, and engineering 2nd edn (boulder, co. *CO: Westview Press.[Google Scholar]*, 2015.

[97] Steven H Strogatz. From kuramoto to crawford: exploring the onset of synchronization in populations of coupled oscillators. *Physica D: Nonlinear Phenomena*, 143(1):1–20, 2000.

[98] Steven H Strogatz. Exploring complex networks. *Nature*, 410(6825):268, 2001.

[99] Steven H Strogatz, Daniel M Abrams, Allan McRobie, Bruno Eckhardt, and Edward Ott. Theoretical mechanics: Crowd synchrony on the Millennium Bridge. *Nature*, 438(7064):43–44, 2005.

[100] Hisa-Aki Tanaka, Allan J Lichtenberg, and Shin'ichi Oishi. First order phase transition resulting from finite inertia in coupled oscillator systems. *Physical Review Letters*, 78(11):2104, 1997.

[101] Hisa-Aki Tanaka, Allan J Lichtenberg, and Shin'ichi Oishi. Self-synchronization of coupled oscillators with hysteretic responses. *Physica D: Nonlinear Phenomena*, 100(3-4):279–300, 1997.

[102] Vincent Torre. A theory of synchronization of heart pace-maker cells. *Journal of theoretical biology*, 61(1):55–71, 1976.

[103] F Tricomi. Sur un'equation differentielle de l'electrotechnique, c.-r. acad. sci. paris, 198 (1931), 635; integrazione di un'equation differenziale presentatasi in elettrotecnica. *Ann. Sc. Norm. Sup. Pisa*, 2:1–20, 1933.

[104] Francesco Tricomi. Integrazione di un'equazione differenziale presentatasi in elettrotecnica. *Annali della Scuola Normale Superiore di Pisa-Classe di Scienze*, 2(1):1–20, 1933.

[105] Liudmila Tumash, Simona Olmi, and Eckehard Schöll. Stability and control of power grids with diluted network topology. *Chaos*, 29:123105, 2019.

[106] Yunjiao Wang and Martin Golubitsky. Two-colour patterns of synchrony in lattice dynamical systems. *Nonlinearity*, 18(2):631, 2004.

[107] John A Wolf and Paul F Koch. Disruption of network synchrony and cognitive dysfunction after traumatic brain injury. *Frontiers in Systems Neuroscience*, 10:43, 2016.

[108] Matthias Wolfrum and E Omelchenko. Chimera states are chaotic transients. *Physical Review E*, 84(1):015201, 2011.

[109] Matthias Wolfrum, Oleh E Omelchenko, Serhiy Yanchuk, and Yuri L Maistrenko. Spectral properties of chimera states. *Chaos: An Interdisciplinary Journal of Nonlinear Science*, 21(1):013112, 2011.

[110] Gang Yan, Petra E Vértes, Emma K Towlson, Yee Lian Chew, Denise S Walker, William R Schafer, and Albert-László Barabási. Network control principles predict neuron function in the caenorhabditis elegans connectome. *Nature*, 550(7677):519–523, 2017.

CHAPTER 4

APPENDIX FOR CHAPTER 3

In this appendix, we provide the two of the Python scripts used to analyze and simulate the three-population network of 2D oscillators. The first is `Equations.py`, which provides the complete pallate of parameters and several of the key equations given in Chapter 3. The second code, `manifoldRuns_alpha_betaFromArgv.py`, calculates winding numbers associated with a phase shift cluster solution in the three-population network. These numbers, plotted in Fig. 3.5 as functions of the phase lag α and inertia β, characterize existing regular and chaotic phase shift dynamics in the three-population Kuramoto model. This Python code can be easily adapted for further exploring new types of dynamical effects and cooperative structures in multipopulation networks of phase oscillators.

More precisely, `manifoldRuns_alpha_betaFromArgv.py` simulates the dynamics of the 4D pendulum system (3.7) on the manifold $C_{\Theta\Phi\Psi}$. After skipping a transient time, this script calculates the period of $x(t)$ around the cylinder $[-\pi, \pi)$ according to the following cases. Without loss of generality, the procedure is described for x; it is also valid for z.

Case I: $\langle|\dot{x}|\rangle < \epsilon$ for some $0 < \epsilon \ll 1$. Then $x(t)$ is assumed to be a fixed point with winding number 0.

Case II: $|\langle\dot{x}\rangle| < \epsilon$. In practice, this requires averaging over many more time points and having a larger ϵ than in Case I. Then $x(t)$ is assumed to be an oscillatory (small) limit cycle. Consider the ordered pair $A(t) = (x(t), \dot{x}(t))$. As $t \to \infty$, $\exists\tau > 0$ independent of t such that $A(t) = A(t + \tau)$ if the system is not chaotic. In this case, there will exist countably many points $A_k(t_k) = (x, 0)$ such that $\ddot{x} > 0$. However, a numerical simulation produces discrete points that may not overlap in a limit cycle. To overcome this, we project nearby points along a secant line of the trajectory to the line $\dot{x} = 0$ as follows: Find a set of numerical timesteps $\left\{t_k^+\right\}$ whose previous numerical timesteps are $\left\{t_k^-\right\}$ such that points

$B_k(t_k^+) = (x(t_k^+), \dot{x}(t_k^+))$ have $\dot{x}(t_k^+) \geq 0$, $\ddot{x}(t_k^+) > 0$ and the points $C_k(t_k^-) = (x(t_k^-), \dot{x}(t_k^-))$ have $\dot{x}(t_k^-) < 0$, $\ddot{x}(t_k^-) > 0$. Since $\ddot{x}$ remains positive and continuous over this interval, we use the intermediate value theorem to conclude the existence of $A_k(t_k)$ for all k, $t_k^- < t_k < t_k^+$. We take $A_k^*(t_k) = (x^*, 0) \stackrel{\Delta}{=} (a_k, 0)$ as the intersection between $\overline{B_k C_k}$ and the line $\dot{x} = 0$ as an approximation for A_k. If the timestep is sufficiently small, we are guaranteed that $|x(t_+) - x(t_-)| \ll \dot{x}(t_+) - \dot{x}(t_-)$, so A_k^* is a highly accurate approximation for A_k.

Finally, we take the standard deviation s of $\{a_1, a_2, a_3, \dots\}$. If s is very small, the winding number is taken as 1. Otherwise, we follow the following procedure: Set $\Delta = 1$. Find the standard deviation s_Δ of $D = \{(a_{\Delta+1} - a_1, a_{\Delta+2} - a_2, a_{\Delta+3} - a_3, \dots\}$. If s_Δ is very small, assume that it takes Δ cycles for the system to return to the neighborhood of $(a_k, 0)$ after starting there. Otherwise, increase s_Δ by one. Repeat this procedure unless Δ is at least as high as an arbitrary threshold, here set at 30, in which case assume that Δ is infinitely large (chaos).

Case III: Project $x(t)$ onto $(x(t) - \pi) \bmod (2\pi) - \pi$. Then x is assumed to be a rotatory (large) limit cycle around the cylinder $[-\pi, \pi)$. Thus there will exist countably many points $A_k(t_k) = (-\pi, \dot{x}_k)$. Following similar reasoning to Case II, find all points $B_k(t_k^+) = (x(t_k^+), \dot{x}(t_k^+))$ such that for the previous numerical timestep t_k^- forming $C_k(t_k^-) = (x(t_k^-), \dot{x}(t_k^-))$, $x(t_k^+) < x(t_k^-)$ when $\dot{x}(t_k^+) > 0$ or $x(t_k^+) > x(t_k^-)$ when $\dot{x}(t_k^+) < 0$; this represents x crossing the $\pm\pi$ threshold on the cylinder. Note that this requires $\dot{x}$ to remain positive or remain negative for all time over this limit cycle, but with the parameters used this was always the case for rotatory limit cycles. Over a sufficiently small timestep, we may take $\ddot{x}$ as roughly constant. Then similarly to Case II, we find the intersection between the secant line $\overline{B_k C_k}$ and $x = -\pi$. The procedure for finding the winding number is also similar to the one in Case II, except it is done over $\dot{a}_k$ and the differences between those rates.

If a "loop" emerges on a rotatory limit cycle, where x switches signs a positive even number of times on its transversal around the cylinder, then a hybrid calculation may have to be used for period. However, with our parameters we never observed this phenomenon

for stable manifolds.

Equations.py

```
"""
Equations from the 3D Kuramoto system with inertia and fixed points of
    interest.

Equation numbers matching Brister, et al. (2020) are given where applicable.
"""

import numpy as np
import warnings

alphaArray799 = np.linspace(0, np.pi/2, 801)[1:-1]
betaArray800 = np.linspace(0, 250, 801)[1:]

'''First row is alpha; second is beta. Columns are points A, B, C, D, E, the
spots in the ENE area of the graph, and the old Fig. 13. A's alpha needs to be
alphaArray[787] when plotted for visualization.'''
examplePointIDs = np.array([[793, 436, 53, 783, 53, 619, 339],
                            [31, 249, 196, 379, 20, 786, 799]])
examplePoints = np.c_[alphaArray799[examplePointIDs[0]],
                      betaArray800[examplePointIDs[1]]].T

'''Quartic characteristic equation (12). Is zero at the four fixed points.'''
charac = lambda a, h, delta, s, x, z: (s**2 + h*s + np.cos(x))*\
    (s**2 + h*s + np.cos(z)) - a**2 * np.cos(x-delta) * np.cos(z-delta)
```

```
'''System of equations (8) for the fixed points. Returns [0,0] there.'''
fixedPoint = lambda x, z, a, delta, omega:\
    np.array([np.sin(x) + a*np.sin(z-delta) - omega,
              np.sin(z) + a*np.sin(x-delta) - omega])

'''Equation (9) for the x=z fixed point. Returns 0 there.'''
fixedPointInner = lambda x, a1, delta1, omega: a1*np.sin(x-delta1) - omega

'''The Kuramoto order parameter. X is assumed to be an angle.'''
def KuramotoOrder(X):
    if not hasattr(X, '__len__'): #A single point
        return 1.
    if not isinstance(X, np.ndarray):
        X = np.array(X)
    if len(X.shape) == 1:
        return np.abs(np.average(np.exp(1j*X)))
    return np.average(np.abs(np.average(np.exp(1j*X), axis=1)))

'''Complement of the Heaviside function: lightside(x) = 1-H(x).
Deprecated with np.atan2.'''
def lightside(X):
    warnings.warn('Use numpy.arctan2 instead of the lightside function',
                  DeprecationWarning)
    if np.any(X==0):
        warnings.warn('Heaviside(0) is ambiguous', RuntimeWarning)
    return X<=0.
```

```
'''Maps the angle to the coterminal angle on [-pi, pi).'''
modNegToPosPi = lambda x: np.mod(x - np.pi, 2*np.pi) - np.pi

'''Repeats a 1D array with the same size as the alphaArray over the betas.'''
repeatOverBetas = lambda x, m_beta:\
    np.repeat(x, m_beta).reshape([x.size, m_beta])

'''Approximation (18) for the Tricomi function (Belykh, et al.)'''
Tricomi = lambda h: 4*h/np.pi - 0.305*h**3

'''Class for the 3-cluster Kuramoto system with inertia. Various parameters
are derived from the base variables alpha, beta, gamma, N, and M. Alpha and
beta can be vectors. Only h's and the Trichomi curve depend on beta. R_1 and
delta_2 used to be R_0/R_hat and delta_R0/delta_hat, respectively.

alpha, beta, gamma, N, M: Required system parameters.

reshapeArrays: Whether to reshape alpha or beta such that these two arrays
    form a grid. Likely to be deprecated in the future.

fullSys: Whether to use the full system described in system (2) (if False:
    uses the manifold system (7)

calcFixedPoints: Whether to calculate the fixed points of the system and
    their stability.
```

```
    oppositeGammas: Whether gamma_Theta_Phi = -gamma_Psi_Phi. Universally set to
        False for Brister, et al. (2020)'''
class Kuramoto3DSys:
    def __init__(self, alpha, beta, gamma, N, M, reshapeArrays=True,
                 fullSys=False, calcFixedPoints=False, oppositeGammas=False):
        self.alpha = alpha; self.beta = beta
        self.N = N; self.M = M; self.gamma = gamma
        self.fullSys = fullSys
        self.P = 2*N+M

        self.Omega = (M-N)*np.sin(alpha)
        self.R = gamma*np.sqrt(N**2 + M**2 + 2*M*N*np.cos(2*alpha))
        self.R_1 = gamma*np.sqrt(4*N**2 + M**2 + 4*M*N*np.cos(2*alpha))
        self.delta_0 = np.arctan((M-N)/(M+N) * np.tan(alpha)) #For R, not R_1
        self.delta_2 = np.arctan((M-2*N)/(M+2*N) * np.tan(alpha))
        self.delta = alpha + self.delta_0
        self.a = gamma*N/self.R
        self.a1 = np.sqrt(1 + self.a**2 + 2*self.a*np.cos(self.delta))
        self.delta_1 = np.arctan2(self.a*np.sin(self.delta),
                                  1+self.a*np.cos(self.delta))
        self.omega = self.Omega/self.R

        ratio = self.Omega/self.R_1
        if hasattr(alpha, '__len__'): #i.e., alpha is not a scalar
            self.x_e = np.zeros_like(alpha)
            self.x_e[np.abs(ratio) <= 1] = np.arcsin(ratio) - self.delta_2
            self.x_e[np.abs(ratio) > 1] = np.nan
```

```
        else:
            with warnings.catch_warnings(): #possibility of undefined arcsin
                warnings.simplefilter("ignore")
                self.x_e = np.arcsin(ratio) - self.delta_2
        self.x_s = self.x_e + self.delta_0
        self.x_sd = np.pi - self.x_e - 2*self.delta_2
        self.x_u = np.pi - 2*self.x_s + 2*self.delta_1


        R = self.R #we only want local R reshaped for h's calculation
        R_1 = self.R_1
        if reshapeArrays:
            try:
                R = R.reshape([alpha.size, 1])
                R_1 = R_1.reshape([alpha.size, 1])
            except AttributeError:
                pass #nothing to do if R is just a single number
        try:
            beta = beta.reshape([1, beta.size])
        except AttributeError:
            pass
        self.h = 1/np.sqrt(np.dot(R, beta)) #R or beta could be a scalar
        self.h_1 = 1/np.sqrt(np.dot(R_1, beta))
        self.Tricomi = Tricomi(self.h)
        self.Tricomi_1 = Tricomi(self.h_1)


        if fullSys: #assumes 1st and 3rd clusters are of size N and
            unconnected
```

```
        onesN = np.ones(N); onesM = np.ones(M)
        self.e_N = np.concatenate([onesN, self.gamma*onesM, np.zeros(N)])
        self.e_M = np.concatenate([self.gamma*onesN, onesM,
                                   (1-2*oppositeGammas)*self.gamma*onesN])
        self.e_L = np.concatenate([np.zeros(N), (1-2*oppositeGammas)*\
                                   self.gamma*onesM, onesN])

    elif calcFixedPoints: # The four fixed points
        g = np.arctan2(1 - self.a*np.cos(self.delta),
                       self.a*np.sin(self.delta)) #kappa/2
        self.kappa = 2*g

        x_0 = np.arccos(self.omega*np.sqrt(1 + self.a**2\
            -2*self.a*np.cos(self.delta))/(1-self.a**2))
        self.x_1 = np.arcsin(self.omega/self.a1) + self.delta_1
        self.x_2 = np.pi - np.arcsin(self.omega/self.a1) + self.delta_1
        self.x_3 = g+x_0; self.x_4 = g-x_0

        b_lambda = (np.cos(self.x_3) + np.cos(self.x_4))/-2
        disc_lambda = np.sqrt(
            0j + (np.cos(self.x_3) - np.cos(self.x_4))**2 + 4*self.a**2
            * np.cos(self.x_3 - self.delta)
            * np.cos(self.x_4 - self.delta))/2
        lambda_1 = b_lambda + disc_lambda
        lambda_2 = b_lambda - disc_lambda
        self.lambda_1 = lambda_1; self.lambda_2 = lambda_2 #for debugging
```

```
        if reshapeArrays:
            try:
                lambda_1 = lambda_1.reshape([alpha.size, 1])
                lambda_2 = lambda_2.reshape([alpha.size, 1])
            except AttributeError:
                pass #nothing to do if beta is just a single number
        disc_s1 = np.sqrt(self.h**2/4 + lambda_1)
        disc_s2 = 1j*np.sqrt(np.abs(self.h**2/4 + lambda_2))
        self.s = -self.h/2 + np.array([disc_s1, -disc_s1, disc_s2, -
            disc_s2])

    '''Full system differential equation (2).
    First P cells = theta; the rest = thetaDot.'''
    def f_full(self, Y, t):
        assert self.fullSys, 'f_full requires the full system'
        theta = Y[:self.P]; thetaDot = Y[self.P:]
        sinTheta = np.sin(theta.reshape([-1,1]) - theta - self.alpha)
        ThetaN = np.multiply(self.e_N, sinTheta[:self.N])
        ThetaM = np.multiply(self.e_M, sinTheta[self.N : self.N+self.M])
        ThetaL = np.multiply(self.e_L, sinTheta[self.N+self.M : self.P])
        return np.r_[
            thetaDot, (-thetaDot + np.sum(np.r_[ThetaN, ThetaM, ThetaL],
                                          axis=0))/self.beta]

    '''Differential equation (7) on the manifold.'''
    def f_manifold(self, Y, t):
        assert not self.fullSys, 'f_manifold requires the manifold system'
```

```
        x = Y[0]; z = Y[1]; xDot = Y[2]; zDot = Y[3]
        return np.array(
            [xDot, zDot,
             (self.Omega - xDot - self.R*np.sin(x+self.delta_0)
              - self.gamma*self.N*np.sin(z-self.alpha))/self.beta,
             (self.Omega - zDot - self.R*np.sin(z+self.delta_0)
              - self.gamma*self.N*np.sin(x-self.alpha))/self.beta])


    '''Differential equation (9) on the inner Theta_Phi_Theta manifold.'''
    def f_inner_manifold(self, X, t):
        MESSAGE =\
            'f_inner_manifold requires the Theta_Phi_Theta manifold system'
        assert not self.fullSys, MESSAGE
        assert len(X)==2, MESSAGE + ', not just Theta_Phi_Psi.\n'\
            + 'Input vector should be (x, xDot) only.'
        x = X[0]; xDot = X[1]
        return np.array([xDot, self.omega - self.h*xDot - self.a1
                         *np.sin(x-self.delta_1)])
```

manifoldRuns_alpha_betaFromArgv.py

```
"""
Simulation of the system on the C_Theta_Phi_Psi manifold. alpha and beta can
be arrays. A single value of beta will be selected, which can be from a
command-line argument.
"""


'''Simulation parameters'''
```

```
runFromArgv = True#; runFromArgv = False
runFromLastSoln = True; runFromLastSoln = False #will also load params
DEBUG = True; DEBUG = False
oppositeGammas = False


import numpy as np
from scipy.integrate import odeint
import math
import sys
sys.path.append(['d:/Research_Kuramoto_system/3D_Simulations/Lib',
                 '/home/users/bbrister1/Kuramoto/Lib']
                [int(runFromArgv*(not DEBUG))])
import Equations
import TimeTracker
from scipy import stats


'''Mathematical constants'''
mu = 1.
N, M, nu = 24, 25, 0.4
n_alpha, m_beta = 801, 801
eps = 0.001
timer = TimeTracker.TimeTracker()


#Step 0: Get the data.
alphaArray = np.linspace(0, np.pi/2, n_alpha)[1:-1]
betaArray = np.linspace(0., 250., m_beta)[1:]
n_alpha = alphaArray.size; m_beta = betaArray.size;
```

```
gamma = nu/mu
if DEBUG:
    alphaIndex = [53]; betaID = 196 #Key West
#    alphaIndex = [70]; betaID = 150
elif runFromArgv:
    try:
        betaID = int(sys.argv[1])
    except ValueError:
        raise ValueError('No index value provided for beta. ' +\
                         'Current input:\n' + str(sys.argv))
    except IndexError:
        raise IndexError('Integer between 0 and ' + str(m_beta-1) +\
              ' required. Current input:\n' + str(sys.argv[1]))
else:
    betaID = 1 #set to the desired index
if not DEBUG:
    alphaIndex = range(n_alpha)
beta = betaArray[betaID]
n_alpha = alphaArray.size
n_windingArray = np.zeros([n_alpha, 2]).astype(np.int32)
initConds1 = np.array([0, 2, -1, -2])
lastSoln = np.zeros([n_alpha, 4])


'''Simulation constants. Times:
t0: Starting time of the entire simulation
t_step: odeint timestep
t_max: Length of time per rep (m_reps)
```

```
t_start: Time at the beginning of the analysis/graphing portion per rep
t_final: Time at the end of all runs
'''
t_step = 0.005
t_max = 5000
m_reps = 40
if DEBUG:
    t_max = 5000; m_reps = 3
n_max = int(t_max/t_step) + 1
t_start = 500.
n_start = min(int(t_start/t_step) + 1, n_max)
t0 = 0.
if runFromLastSoln:
    t0 = np.load('params.npy')[6]
t_final = t0 + t_max*m_reps


'''Simulator starts here.'''
#pctComplete = 0.
for i in alphaIndex:
    if runFromLastSoln:
        initConds = np.load('lastSoln' + str(betaID) + '.npy')[i,:]
        [mu, nu, M, N, n_start, t_step] = np.load('params.npy')[:-1]
        [M, N] = np.array([M, N]).astype(int)
        P = 2*N+M
    else:
        t0 = 0
        initConds = np.copy(initConds1)
```

```
    alpha = alphaArray[i]
    system = Equations.Kuramoto3DSys(alpha, beta, gamma, N, M, fullSys=False,\
          calcFixedPoints=False, oppositeGammas=oppositeGammas)

    #Step 1: Run for a bit.
    for j in range(m_reps):
        t1 = np.linspace(t0+t_max*j, t0+t_max*(j+1), n_max)
        soln = odeint(system.f_manifold, initConds, t1)[-n_start:,:]
        initConds = soln[-1,:]
#         pctComplete = 100*(i+(j+1.)/m_reps)/n_alpha
        lastSoln[i,:] = soln[-1,:]

        for k in [0,1]: #whether we are looking at x or z
            if np.average(np.abs(soln[:,k+2])) < 1e-6: #likely fixed point
                n_windingArray[i,k] = 0; m=0
                indecesListed = False
            elif np.abs(np.average(soln[:,k+2])) < 0.05:
                #likely small limit cycle
                indecesListed = True
                #Step 2: Get the indeces where xDot crosses from - to +.
                indeces = np.all([soln[:-1,k+2]<0, soln[1:,k+2]>0], axis=0)
                indeces = np.nonzero(indeces)[0][1:]
                #Check that the last index != last item in array.
                if np.any(indeces >= soln.shape[0]-1):
                    indeces = np.delete(indeces, -1)
                #Step 3: Get the RECIPROCAL of the extrapolation line slopes.
                flatness =\
```

```
            np.array(np.divide(soln[indeces+1, k]-soln[indeces, k],
            soln[indeces+1, k+2]-soln[indeces, k+2]))
        #Step 4: Linear interpolation from (x0, xDot0) to (x1, 0).
        #Increases accuracy.
        X = flatness*soln[indeces, k+2] + soln[indeces, k]
        #Step 5: Compute the standard deviations.
        if np.std(X, ddof=1) < eps: #value of eps is a judgment call
            m = 1
            n_windingArray[i,k] = 1
        else:
            m = int(min(30, X.size/2-1))
            for ell in range(1,m):
                if np.std(X[ell:]-X[:-ell], ddof=1) < eps:
                    n_windingArray[i,k] = ell
                    break
                else:
                    n_windingArray[i,k] = m #likely chaos
    else: #likely large limit cycle
        indecesListed = True
        #Step 2: Get the indeces of x where mod(x-pi, 2*pi) is a min.
        X = Equations.modNegToPosPi(soln[:,k])
        indeces =\
            np.r_[True, X[1:] < X[:-1]] & np.r_[X[:-1] < X[1:], True]
        indeces = np.nonzero(indeces)[0][1:]
        #Check that the last index != last item in array.
        if np.any(indeces >= X.size-1):
            indeces = np.delete(indeces, -1)
```

```
            #Step 3: Get the extrapolation line slopes.
            slope =\
                np.array(np.divide(soln[indeces+1, k+2]-soln[indeces, k
                    +2],
                X[indeces+1]-X[indeces]))
            #Step 4: Linear extrapolation from (x1, xDot1) to (-pi, xDot0)
                .
            #Increases accuracy.
            velocities = soln[indeces, k+2] - slope*(np.pi + X[indeces])
            #Step 5: Compute the standard deviations.
            if np.std(velocities, ddof=1) < eps: #judgment call
                m = 1
                n_windingArray[i,k] = 1
            else:
                m = min(30, velocities.size/2-1)
                for ell in range(1, int(m)):
                    if np.std(velocities[ell:]-velocities[:-ell],
                              ddof=1) < eps:
                        n_windingArray[i,k] = ell
                        break
                    else:
                        n_windingArray[i,k] = m #likely chaos
'''If the winding number is 1, we have a limit cycle, and if it is 0,
we have a fixed point. The conditions needed to get these results are
strict, and chaos is highly unlikely to emerge if this happens. Thus
there is no need to continue this run.'''
if max(n_windingArray[i]) <= 1: #likely limit cycle or F.P.
```

```
            if DEBUG:
                print('Breakout when j=' + str(j))
            break

    #Step 6: Get the period (in array, not time, units).
    if m < 1:
        n_winding = 0
    else:
        n_winding = min(m, np.prod(n_windingArray[i,:])/\
            math.gcd(n_windingArray[i,0], n_windingArray[i,1]))
        if DEBUG:
            print('GCD:', math.gcd(n_windingArray[i,0], n_windingArray[i,1]))

    if indecesListed:
        T = stats.mode(indeces[n_winding:]-indeces[:-n_winding])[0][0]
#     pctComplete = 100*(i+1.)/n_alpha

if not DEBUG:
    np.save('n_winding' + str(betaID), np.array([n_windingArray]))
    np.save('lastSoln' + str(betaID), lastSoln)
    if betaID == 1: #The following only need saving once.
        np.save('alphaArray', alphaArray)
        np.save('betaArray', betaArray)
        np.save('params', np.array([mu, nu, M, N, n_start, t_step, t_final,
                                    oppositeGammas]))
if DEBUG:
    import matplotlib.pyplot as plt
```

```
    for i in range(2):
        plt.figure()
        strTitle = ['x', 'z'][i]
        strTitle += '. $N = ' + str(N) + '$; $M = ' + str(M) + '$; ' +\
            r'$\alpha/\pi = ' + str(alpha/np.pi) + r'$; $\beta = ' + str(beta)
                \
            + '$; $t=' + str(t_final) + '$\n$\mu = ' + str(mu) + r'$; $\nu = '
                \
            + str(nu) + r'$'
        plt.title(strTitle)
        plt.plot(Equations.modNegToPosPi(soln[-n_start:,i]),
                 soln[-n_start:,i+2], c=['r','b'][i])
    plt.show()
    print('Last soln: ', soln[-1,:])
    print('Winding numbers:', n_windingArray[alphaIndex[0],:])


print(timer.getElapsedTime())
```